

FERMILAB-MASTERS-2021-06

**Cherenkov and Transition Radiation as Low-Energy
Background Sources in SuperCDMS Detectors**

by

Ashley Li

B.A., The University of Chicago, 2018

A THESIS SUBMITTED IN PARTIAL FULFILLMENT
OF THE REQUIREMENTS FOR THE DEGREE OF

Master of Science

in

THE FACULTY OF GRADUATE AND POSTDOCTORAL
STUDIES

(Physics)

The University of British Columbia

(Vancouver)

August 2021

© Ashley Li, 2021

The following individuals certify that they have read, and recommend to the Faculty of Graduate and Postdoctoral Studies for acceptance, the thesis entitled:

Cherenkov and Transition Radiation as Low-Energy Background Sources in SuperCDMS Detectors

submitted by **Ashley Li** in partial fulfillment of the requirements for the degree of **Master of Science in Physics**.

Examining Committee:

Scott Oser, Physics and Astronomy, UBC
Supervisor

Alison Lister, Physics and Astronomy, UBC
Additional Examiner

Abstract

The Weakly Interacting Massive Particle (WIMP) has historically been a prime candidate for dark matter due to its elegant compatibility with the Minimally Supersymmetric Standard Model (MSSM). Recent dark matter experiments have ruled out much of the $\text{GeV} \sim \text{TeV}$ mass range predicted by the MSSM, however, and the newest generation of direct detection experiments, such as SuperCDMS SNOLAB, have begun to explore sub-GeV dark matter.

As experiments push towards lower masses, sensitivity to eV-scale electron recoil events has become increasingly important. A variety of unexplained excesses at energy deposits of $1 \sim 100$ eV have been found in many such low-mass experiments, across different detection techniques and at different excess rates. These low-energy events are not thought to be dark matter, and they must be understood and effectively removed to further improve detector energy resolution.

This thesis will outline the simulation of one possible source of low-energy excess at SuperCDMS: optical photons produced from charges in uniform motion, specifically from Cherenkov radiation (CR), transition radiation (TR), and the intermediate hybrid transition-Cherenkov radiation (HR). In the latter case, the standard formulae for HR contain divergences at certain angles in transparent media, which are an artifact of their derivation and become problematic to simulate. To resolve this, we present a novel approach to normalize the divergent HR peaks, which allows HR to transition smoothly between TR and CR in a numerical simulation.

We also add TR and CR as a physics process to the SuperCDMS Monte Carlo simulation package SuperSim, based on the Geant4 simulation toolkit. To verify the physics of our addition, we show some test simulations in comparison to theoretical predictions of optical radiation intensity. We also use the simulation to make

some preliminary predictions on the contribution of TR and CR to the low energy background, with the expectation that more thorough analyses will be conducted in the future.

Lay Summary

The universe has been shown to contain large amounts of invisible or “dark” matter that does not interact with light, and is consequently difficult to detect – thus far, no experiment has yet made a convincing discovery of a dark matter particle. The current generation of the SuperCDMS experiment aims to expand the search of dark matter to masses lighter than a proton, which requires increased sensitivities to lower energy phenomena, and introduces new and unexplained backgrounds.

In this thesis, we study low energy light emitted in SuperCDMS detectors as one possible source of unexplained backgrounds. To this end, we provide a mathematical overview of the physics involved, and discuss the implementation of the physics in our simulation software. This is intended both as a preliminary study of these backgrounds, and as the groundwork for more detailed studies in the future.

Preface

All work throughout this thesis were done in close consultation with my advisor, Scott Oser. The text in this thesis is written in my own words, except for plots that are reproduced with permission and are cited accordingly.

In Chapters 1 to 3 of this thesis, I present an overview of dark matter, the SuperCDMS experiment, and observations of unexplained low energy backgrounds, drawing entirely on the work of others to motivate my own investigation. In particular, much of Chapter 3 references the compilation of low energy excesses done by Kurinsky et al. in Ref [1].

Chapter 4 contains a theoretical description of Cherenkov and transition radiation, drawing heavily from the many papers on the subject by Zrelov, Ruzicka, Pafomov, Tamm, and others. In it, I present several original plots, to support a novel method of correcting the hybrid radiation divergences. This was directly inspired by the interpretation of hybrid radiation given by Zrelov et al. in Ref [2].

Chapter 5 contains original calculations in estimating the contribution of transition and Cherenkov radiation to low energy backgrounds, most of which are based on the internal SuperCDMS work of Alan Robinson [3] and the work of Du et al. in Ref [4].

The first two sections of Chapter 6 describe the Geant4 and SuperSim simulation packages, summarized respectively from the Geant4 user manuals [5–7], and various SuperCDMS internal documentation [8] and theses [9]. The last section of Chapter 6 contains a description of the implementation of optical properties done largely by Birgit Zatschler, in addition to my original implementation of transition and Cherenkov radiation processes in SuperSim. Much of the original work described in this chapter was done in consultation with Birgit Zatschler and Mike

Kelsey of the SuperCDMS collaboration.

Finally, Chapter 7 presents results from running the SuperSim software package with the original additions described in Chapter 6. Visualizations in this chapter were made using the HepRApp software [10].

Table of Contents

Abstract	iii
Lay Summary	v
Preface	vi
Table of Contents	viii
List of Tables	xii
List of Figures	xiv
Acknowledgments	xx
1 An Overview of Dark Matter	1
1.1 Astronomical Evidence	1
1.1.1 Galaxy rotation curves	2
1.1.2 MACHOs as dark matter	4
1.1.3 Galaxy cluster collisions	5
1.2 Dark Matter Cosmology	6
1.2.1 Curved Spacetime	7
1.2.2 The Λ CDM Model	8
1.2.3 Dark matter freeze-out	10
1.3 The WIMP in Particle Physics	13
1.3.1 The Hierarchy Problem	13
1.3.2 Supersymmetry	14

1.4	Dark Matter Detection	15
1.4.1	Indirect Detection	16
1.4.2	Accelerator Searches	16
1.4.3	Direct Detection	17
1.5	Low-Mass Dark Matter Hypotheses	19
2	The SuperCDMS Experiment	21
2.1	Theory of Operation	21
2.2	Detector Types	25
2.2.1	iZIP and HV	25
2.2.2	HVeV	27
2.2.3	CPD/LAPD	28
2.3	Detector Backgrounds	28
2.3.1	The SNOLAB test facilities	29
2.3.2	External Radiation	30
2.3.3	Internal Bulk Radiation	31
2.3.4	Internal Surface Radiation	33
2.3.5	Cosmic Muons	34
3	Low-Energy Backgrounds in Dark Matter Experiments	35
3.1	Low-Energy Backgrounds in Low-Threshold Detectors	36
3.1.1	A Qualitative Description of Low-Threshold Detectors	36
3.2	Low-Energy Backgrounds in SuperCDMS LAPD and HVeV-0VeV	41
4	Radiation from Charges under Uniform Motion	43
4.1	Cherenkov Radiation	44
4.1.1	Complex Index of Refraction	44
4.1.2	Cherenkov Radiation over an Infinite Path	44
4.2	Transition Radiation	46
4.2.1	TR at Normal Incidence	46
4.2.2	TR at Oblique Incidence	48
4.3	Hybrid Cherenkov-Transition Radiation	49
4.3.1	Divergence at the Cherenkov Angle	51
4.3.2	The HR Formation Length	53

4.3.3	HR and Finite Path CR	56
4.3.4	Suppression of HR from Scattering	58
5	Estimates of Cherenkov and Transition Radiation in SuperCDMS	
	Detectors	59
5.1	Transition Radiation in SuperCDMS SNOLAB	59
5.1.1	TR from Radon Decay Background	60
5.1.2	TR from Beta Decays in Cirlex	61
5.1.3	TR from Muon Background	63
5.1.4	Other TR Sources	64
5.2	Cherenkov Radiation in SuperCDMS SNOLAB	64
5.3	Cherenkov and Transition Radiation in SuperCDMS HVeV Above-ground	67
6	SuperCDMS Simulation Software	69
6.1	Geant4 Basics	69
6.1.1	Runs and Events	69
6.1.2	Particles	70
6.1.3	Tracking and Stepping	71
6.1.4	Physics processes	72
6.1.5	Geometry and Materials	74
6.2	The SuperSim Package	75
6.2.1	SuperSim Structure	76
6.3	Implementation of Transition and Cherenkov Radiation in SuperSim	77
6.3.1	The Electromagnetic-Optical schism	77
6.3.2	Existing implementations	78
6.3.3	Optical properties of materials	80
6.3.4	Hybrid radiation physics process	80
6.3.5	Future efficiency improvements	84
7	Transition and Cherenkov Radiation Simulation	86
7.1	Electron Beam on Copper	87
7.1.1	Primary Rejection	89
7.1.2	Position Dependence	90

7.2	Bi-210 Decays in Copper	91
7.3	Hybrid Radiation in Cirlex	92
7.3.1	Pa-234 and K-40	92
7.4	CR and TR energy ranges	94
8	Conclusions	97
	Bibliography	99

List of Tables

Table 1.1	Measured values for various density parameters, produced by the <i>Planck</i> Collaboration [11] and compiled in Ref [12]	9
Table 2.1	Activity rates (mBq/kg) of various isotopes in various important non-detector materials used at SuperCDMS SNOLAB, using recent assays compiled internally. Here, Cirlex is a proprietary polyimide film derived from Kapton; μ -metal refers to a nickle-iron alloy used for magnetic shielding. The total radiation and overall effect on the detector must take into account the relative masses of each material and their placement within the apparatus relative to the detector (e.g. Cirlex has a direct line of sight to the crystal, whereas Kapton does not). A full per-component list of radiocontamination can be found internally at Ref [13].	33
Table 3.1	Low-energy excesses observed at various experiments with single-electron resolutions. Upper and lower bounds are integrated over $n \geq 1$ and $n \geq 2$ electron event rates, respectively; where single-electron rates are unavailable, a lower limit of event rate above threshold is given. Top section corresponds to charge-sensitive calorimeters and CCDs, middle section to interaction-independent calorimeters, and bottom section to noble fluid detectors. Table originally compiled by Kurinsky et al. in Ref [1].	37

Table 5.1	Estimated number of CR photons absorbed in Si per electron in Cirlex, summed from 1 to 6 eV and over the respective mean path lengths [14]. In rows 1 & 3, the betas are assumed to begin at the full energy and slow to rest with constant energy loss, with an average energy of half the full energy; in rows 2 & 4, the betas do not lose energy at all. These values are very rough estimates and likely greatly overestimated, and should only be used as upper limits compared to simulation results.	66
Table 6.1	Some information contained in the respective particle classes in Geant4. Only the fields most relevant to us are listed. The * symbol indicates a pointer.	71
Table 6.2	Some information contained in the <code>G4Step</code> and <code>G4StepPoint</code> classes in Geant4. Only the fields most relevant to us are listed.	72
Table 6.3	Some information contained in the respective volume classes in Geant4. Only the fields most relevant to us are listed. The * symbol indicates a pointer.	75
Table 7.1	TR simulation results from a 389keV electron beam fired at each of the test points in Fig 7.4. “Post-PR” refers to the hit rate after primary rejection. The standard error of the mean is given for uncertainties.	91
Table 7.2	Hit rates of 1~6 eV TR photons produced from Bi-210 decays, distributed evenly over the inner surface of the detector housing to various depths. “Post-PR” refers to the hit rate after primary rejection.	93
Table 7.3	Hit rates of 1~6 eV HR+CR photons from Cirlex in a single detector, for 10,000 events simulated per isotope. “Post-PR” refers to the hit rate after primary rejection.	93

List of Figures

Figure 1.1	Rotation curves measured of many galaxies, each nearing asymptotic values at large distances. Plot taken from Ref [15]. . . .	3
Figure 1.2	Optical image of the Bullet cluster (left) and the Chandra X-ray image of the cluster (right). Green contours represent the mass distribution, reconstructed using weak gravitational lensing. Figure taken from Ref [16].	5
Figure 1.3	Comoving particle number N_X or Y and relic density Ω_X (y-axis) versus temperature T and time t (x-axis). The solid line is a numerical solution to Eq 1.13 that matches the observed DM relic abundance, whereas the dotted line projects DM depletion without freeze-out. Colored regions indicate solutions for cross-sections that differ by 10, 10^2 , and 10^3 respectively. Plot taken from Ref [17].	12
Figure 1.4	Exclusion limits published by various direct detection experiments, accurate up to 2020. Plot taken from [12]	18
Figure 2.1	Projected sensitivity of the SuperCDMS detectors at SNOLAB, in terms of the DM direct detection parameter space. Figure taken from Ref [18].	22
Figure 2.2	Simple schematic describing the function of a QET: phonons entering from the crystal produce quasiparticles (QP) in the aluminum fin, which are trapped and deposit heat into the tungsten TES. Figure taken from Ref [19].	24

Figure 2.3	Phonon channel layout of the iZIP detector (left) and the HV detector (right). In addition, iZIPs have two charge channels; the outer charge channel overlaps with the outer phonon channel, and the inner charge channel with the remaining phonon channels. HV detectors have no charge channels. Figure taken from Ref [20].	25
Figure 2.4	Illustration of the CUTE layout. During operation, the crane payload will be lowered into the drywell. Figure taken from Ref [21].	30
Figure 2.5	Schematic of the main SuperCDMS SNOLAB experiment, including the SNOBOX copper cans at the center. Figure taken from Ref [18].	31
Figure 3.1	Excess rates (Table 3.1) found in various experiments with shown target materials versus rock overburden. Shaded bands indicate regions approximately consistent with excess rates for Ge (red), Si (blue), and Xe (green). Muon flux is shown in dashed black for reference of a depth-dependent effect. Figure taken from Kurinsky et al. in Ref [1].	38
Figure 4.1	TR θ distributions (Eq 4.6) of 2 eV photons emitted from an electron traveling from vacuum to copper, at $\beta = 0.5$ (left) and 0.9 (right). Radial axis is in \log_{10} scale, with units $[\text{eV}^{-1}]$. Backward radiation into vacuum is shown in red, and forward radiation into copper is shown in blue. Choice of ϕ is arbitrary as the distribution is symmetric at normal incidence.	47
Figure 4.2	TR θ distributions (Eq 4.6) of 2 eV photons from an electron traveling from copper to vacuum, at $\beta = 0.5$ (left) and 0.9 (right). Radial axis is in \log_{10} scale, with units $[\text{eV}^{-1}]$. Backward radiation into copper is shown in red, and forward radiation into vacuum is shown in blue. Choice of ϕ is arbitrary as the distribution is symmetric at normal incidence.	48

Figure 4.3	TR frequency spectra of an electron traversing a copper-vacuum boundary, emitting forwards into vacuum (solid) and backwards into vacuum (dashed) for several β	49
Figure 4.4	TR θ distributions (Eq 4.7) for an electron traveling from vacuum to copper (left) and copper to vacuum (right), at angle of incidence $\psi = \pi/4$, $\beta = 0.9$, and $\omega = 4$ eV. Radial axis is in \log_{10} scale, with units [eV ⁻¹]. At 4 eV in Copper, $\beta_{CR} > 1$ and Cherenkov radiation is prohibited for all velocities.	50
Figure 4.5	HR distributions (Eq 4.7) for an electron of $\beta = 0.1$ (left) or $\beta = 0.99$ (right) and listed photon frequencies ω , emitted forward from vacuum into silicon (top) or copper (bottom at normal incidence. At higher velocities, HR into silicon shows a strong CR-like peak, whereas HR into copper shows a strong TR-like peak.	52
Figure 4.6	(Left) The Cherenkov threshold (Eq 4.3) in silicon. (Right) The complex refractive index r of silicon over ω	53
Figure 4.7	(Left) Formation lengths l_f (Eq 4.8) for an electron of $\beta = 0.99$ and listed photon frequencies ω , emitted forward from vacuum into silicon at normal incidence. (Right) The left plot zoomed in, with dotted lines that mark the Cherenkov angle θ_{CR} at each ω	54
Figure 4.8	Comparison of HR intensity (Eq 4.9) and CR intensity at various β , emitted forward from vacuum into silicon at normal incidence. Here, CR intensity is multiplied by 2 to show similarities between CR and HR.	55
Figure 4.9	Finite path length CR calculated with the Tamm formula (Eq 4.10 for silicon, $\beta = 0.99$, $\omega = 1$ eV, and a variety of path lengths ℓ	57

Figure 5.1	TR spectra for average Bi-210 decay (389 keV or $\beta = 0.823$) electrons entering copper from vacuum at normal incidence. The three lines are the emission spectrum in black, the absorption spectrum from Si-first reflection (Eq 5.2) in blue, and the absorption spectrum from Cu-first reflection in dashed blue.	61
Figure 5.2	TR spectra for peak cosmic-ray muons (200 GeV) crossing a copper/vacuum interface at normal incidence. The emission spectra are shown in solid lines, and the absorption spectra are shown dashed (Eq 5.2).	63
Figure 5.3	Estimated CR spectra for electrons of various energies traveling in Cirlex. Shown in solid is the flat CR emission spectrum for a constant index of refraction in Cirlex. Dashed lines show the absorption spectra after reflection. These values are likely greatly overestimated, and should only be used as upper limits compared to simulation results.	65
Figure 6.1	Data flow in the SuperCDMS simulation software, including the basic structure of the SuperSim package [8].	76
Figure 7.1	Visualization of the electron beam aimed at the center of an internal copper face, which produces the events shown in Fig 7.2a. The detector crystal (Zip) is shown in magenta, the copper housing in orange, the electron in red and the TR photon in green. The deepest level of zoom (cyan) shows the electron scattering in copper, which has a chance of escaping copper. The visualizations were produced using the HepRApp software [10].	87

Figure 7.2	Energy spectra of backward TR produced from a beam of 389 keV electrons normally incident on a copper surface. In (a) electrons are allowed to freely exit and reenter the copper housing, whereas in (b) electrons are not allowed to exit copper. The measured spectra from our Monte Carlo simulation (Ch 6) is shown in blue; the expected spectra (integrated from the “absorption” distribution in Fig 5.1) is shown in black outline.	88
Figure 7.3	Energy spectra of backward TR produced from a beam of 389 keV electrons normally incident on a copper surface. Fig (a) is identical to Fig 7.2a, reproduced here for comparison to (b), where primary rejection has been applied that removes all TR photons coincident with a charged particle hit. The overall effect is that the hit rates are reduced to below our initial estimate (black outline).	89
Figure 7.4	Test points for checking position dependence of electron sources to TR absorption. A 389 keV beam of electrons, as in Fig 7.1, is fired at each point normally to the inner surface of the copper housing. Results are given in Table 7.1.	90
Figure 7.5	Energy spectra of TR produced from Bi-210 decays, distributed evenly over the inner surface of the detector housing at a skin depth of up to ~ 10 nm. Raw hit rates are shown in (a), whereas the hit rates after primary rejection are shown in (b). The expected spectrum from a monoenergetic 389 keV electron beam is shown in black outline, which we now see was likely an overestimate of the Bi-210 decay TR hit rate.	92
Figure 7.6	Visualization of the SuperCDMS SNOLAB detector with instrumentation. The detector crystal (Zip) is shown in red wire-frame, copper housing in orange, Cirlex DIB connectors in magenta, and empty slots in teal. The visualizations were produced using the HepRApp software [10].	94

Figure 7.7 Simulated energy spectra of HR+CR between 1 and 6 eV after primary rejection, produced from (a) Pa-234 decays and (b) K-40 decays, each distributed evenly over the bulk of Cirlex components (Fig 7.6). 10,000 events were generated for each isotope. 95

Acknowledgments

I am grateful for the patient support of my advisor, Scott Oser, throughout my time as his student and over the course of so many projects. The same goes for the current and former people of the Oser and Rau groups, in particular Belina von Krosigk, Emanuele Michielin, and Ben Smith, who helped me along on various projects, and my fellow grad students, who gave me friendship and sometimes help with homework. I also thank the kind people of the SuperCDMS Simulations Working Group, most of all Miriam Diamond, Mike Kelsey, Birgit Zatschler, and Stefan Zatschler, who have been gracious in teaching me how to build and run my own simulations.

I owe so much to my family, who not only provided the requisite unconditional love but also helped me pay rent, and my friends, who apparently would risk their lives to see me.

I do not thank the COVID-19 pandemic.

Chapter 1

An Overview of Dark Matter

What is dark matter? No one knows for sure.

In this chapter, we will provide an overview of dark matter, its historical discovery, its relationship to cosmology and particle physics, and the current state of dark matter detection. Together, these topics will introduce the concepts that motivate the SuperCDMS experiment and the search for low-mass dark matter.

Many of the discussions in this chapter, especially in the first three sections, follow arguments commonly available in cosmology textbooks. Refs [22, 23] were particularly instrumental in writing this chapter, and citations will be neglected for general information about dark matter and cosmology unless specific experimental figures are presented.

1.1 Astronomical Evidence

First, we will summarize the astronomical observations, primarily of galaxies and galaxy clusters, that suggest the existence of large amounts of invisible matter throughout the universe. We will also use these observations to motivate some of the basic properties of dark matter, most notably its non-baryonic and weakly self-interacting nature, that will lead into the more detailed predictions of cosmology and particle physics in later sections.

1.1.1 Galaxy rotation curves

The traditional starting point for discussions of dark matter is the observation that parts of galaxies seem to be spinning faster than they should.

A classical prediction of galactic rotational velocities can be made using the galactic mass distribution – a galaxy’s mass must provide sufficient gravitational attraction to maintain circular motion. In turn, the mass distribution can be estimated using the observed luminosity of galaxies and a known mass-to-light ratio $\langle M/L \rangle$. The simplest such estimate can be made by assuming that all stars are like our Sun, where $\langle M/L \rangle = M_{\odot}/L_{\odot}$.

Not all stars are like our Sun, however; even in main sequence stars, the mass-to-light ratio can range from 10^{-3} to 10^3 times that of our Sun. A better estimate is to take the average mass-to-light ratio of our solar neighborhood, or stars within 1 kpc of the Sun [22]:

$$\langle M/L_B \rangle \approx 4 \times \frac{M_{\odot}}{L_{\odot,B}} \approx 170,000 \text{ kg W}^{-1} \quad (1.1)$$

where L_B is the luminosity in 400 nm \sim 500 nm or “B-band” light. The mass-to-light ratios of different galaxies tend to be quite close to each other, and our solar neighborhood is a fairly representative sample, although even better estimates can be made by adjusting for the star-formation history of each galaxy. What’s important, though, is that the average mass-to-light ratio can be stated as a constant factor.

Next, the observed surface brightness of a spiral galaxy tends to diminish exponentially with radius R from the galactic center:

$$I(R) = I(0) \exp(-R/R_s) \quad (1.2)$$

where R_s is a scale length that characterizes the radial distribution of stars in a galaxy; in the Milky Way, this is roughly 4 kpc. Using the constant mass-to-light ratio, this can then be converted to a mass distribution $\rho(R) \propto \exp(-R/R_s)$.

The exponentially decaying nature of the mass distribution suggests that the vast majority of the mass is concentrated at the center of the galaxy; hence, the mass contained within the radius R , or $M(R) = \int_R \rho(r) dr$, becomes roughly constant

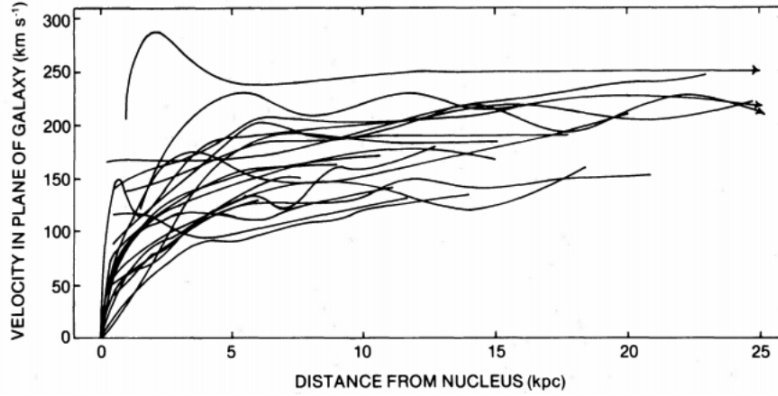


Figure 1.1: Rotation curves measured of many galaxies, each nearing asymptotic values at large distances. Plot taken from Ref [15].

with R at the fringes of the galaxy.

It is fairly straightforward to see how this should affect the galactic rotational velocity. Using basic kinematics, the average velocity at a given radius R should be:

$$v = \sqrt{\frac{GM(R)}{R}} \quad (1.3)$$

where, again, $M(R)$ is the galactic mass enclosed by a sphere of radius R . At large radii, where the enclosed mass is roughly constant, the velocity should simply decrease as $1/\sqrt{R}$.

However, empirical measurements of galactic rotational velocities tell us that this is not the case in reality. Starting in the 1970s, an increasing number of measurements have shown that the rotational velocity tends to stay constant at large radii, or even slightly increase [15, 22]. Some of these velocity-radius plots, or “rotation curves,” are shown in Fig 1.1.

Per Eq 1.3, to produce a uniform velocity the enclosed mass needs to rise *linearly* with R instead. In turn, the mass density needs to fall as $1/R^2$ for a spherically symmetric distribution, or $1/R$ for a flat disk. Either way, this falls much slower than the exponential prediction from luminosity (Eq 1.2). This discrepancy suggests that there exists large amounts of non-luminous matter at the outer edges of

the galaxy, where the true mass-to-light ratio is spatially dependent.

With a uniform velocity, the updated enclosed mass can be estimated with $M(R) = v^2 R/G$. The total mass-to-light ratio of the Milky Way is [22]:

$$\langle M/L_B \rangle \approx 50 \times \frac{M_\odot}{L_{\odot,B}} \times \frac{R_{\text{halo}}}{100 \text{ kpc}} \quad (1.4)$$

where R_{halo} refers to the radius of the invisible halo of matter. This halo radius is not well-measured, but a lower bound of ~ 75 kpc can be set using the orbital velocities of global clusters and satellite galaxies. At this limit, the total mass-to-light ratio is at least $\sim 40 \times M_\odot/L_{\odot,B}$, which is an order of magnitude larger than the stellar-only estimate (Eq 1.1)!

Similar discrepancies have also been found on an intergalactic level, where galaxies within clusters show a dispersion in radial velocity that far exceeds the gravitational attraction provided by luminous mass. Much like galaxies, the clusters' peculiar behavior suggests that most of the cluster mass resides outside of the luminous stars. We will not describe all such measurements here, but a detailed account can be found in Ref [22].

1.1.2 MACHOs as dark matter

The stellar mass-to-light ratio (Eq 1.1) is complicated by the presence of low-luminosity baryonic matter, in the form of dim stellar remnants, brown dwarfs, gas, and dust. The former two are known as Massive Compact Halo Objects, or MACHOs, and have received much attention as potential dark matter candidates.

One well-known consequence of general relativity is that gravitational fields can bend light. Especially massive objects, such as MACHOs, can act as *gravitational lens* when they pass in front of stars, focusing and amplifying light enough for the effect to be detectable on Earth. The abundance of MACHOs can then be measured, despite their low luminosity, by measuring the frequency at which gravitational lensing events occur.

In the 1990s and 2000s, gravitational lensing studies generally ruled out the possibility that the bulk of dark matter is made up of MACHOs. At the high end, the MACHO Collaboration found that MACHOs could account for up to 20% of the dark halo mass of the Milky Way only [24]. Subsequent experiments could not

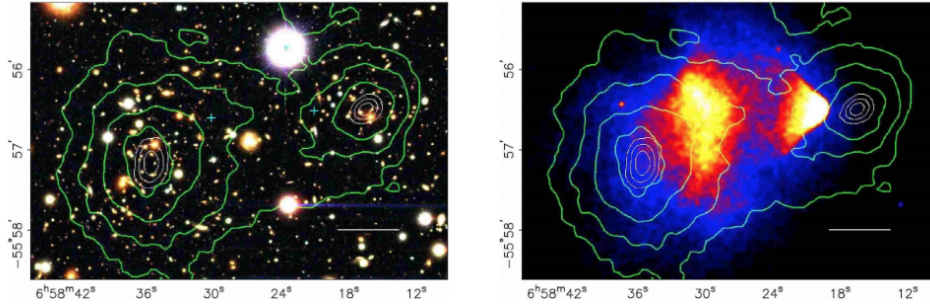


Figure 1.2: Optical image of the Bullet cluster (left) and the Chandra X-ray image of the cluster (right). Green contours represent the mass distribution, reconstructed using weak gravitational lensing. Figure taken from Ref [16].

detect enough lensing events to confirm even that figure, however [25, 26].

The hypothesis that dark matter is baryonic can also be addressed with cosmology, which provides us tools for estimating the composition of the universe; as we will discuss in Section 1.2.2, measurements of the baryonic abundance show that it accounts for only a small fraction of the required total mass content.

1.1.3 Galaxy cluster collisions

Some of the most useful evidence for dark matter has been derived from the Bullet Cluster collision. Separate imaging from the Hubble Space Telescope and the Chandra X-Ray Observatory allows us to view three components of the collision individually; shown in Fig 1.2, these are the optical light emitted by stars, the X-rays emitted by interstellar gas, and the total mass distribution shown by gravitational lensing [16].

In a typical cluster collision, one expects that the sparsely distributed stars would move past each other without much interaction, whereas the intracluster gases would collide directly and slow down relative to the stars. As shown in Fig 1.2, this expectation is correct for the stars and gases, but the mass distributions *also* passes through each other, following the movement of the stars and leaving the gases behind. Since the stellar content of a galaxy cluster cannot make up the bulk of its mass (Section 1.1.1), the movement of the mass distribution sug-

gests that the bulk of the mass is actually made up of a separate, non-stellar and non-gaseous component. And, since we know that the invisible interstellar mass is not made up of MACHOs, but is instead distributed smoothly like intracluster gas, for the mass distributions to pass through each other they must also be very weakly self-interacting. This combination of properties is strongly suggestive of non-baryonic matter.

An important consequence of the Bullet Cluster observation is to challenge non-DM explanations of galactic rotation curves. Of these, the most prominent are a broad class of theories known as *modified gravity*, which attempt to amend general relativity e.g. at very low accelerations [27]. The Bullet Cluster observation directly contradicts predictions made by simpler versions of modified gravity, and also diminishes the necessity of non-DM theories by Occam’s Razor. More recent observations such as gravity wave measurements from LIGO have further challenged modified gravity theories [28].

Increasingly complicated modified gravity theories are still being developed to fit any combination of astrophysical observations [29], and as dark matter eludes detection they may become relevant to experimentalists in the future. That possibility is beyond the scope of the SuperCDMS experiment, however.

1.2 Dark Matter Cosmology

Now that we have a motivation to search for dark matter, we need to predict the basic properties of a potential dark matter particle. One of the most common candidates, and most directly relevant to SuperCDMS, is the Weakly Interacting Massive Particle (WIMP). The WIMP, as its name suggests, is broadly construed as a non-baryonic particle with a nonzero rest mass that interacts on the weak energy scale or less – in the previous section, we saw empirical evidence for these properties in the Bullet Cluster collision. More specifically, however, it refers to the hypothetical lightest particle predicted by supersymmetry, which coincides well with cosmological predictions.

Our discussion of the basic WIMP will be split into separate cosmology and particle physics sections. In this section, we will provide a very brief overview of the cosmology concepts required to understand the role and abundance of dark

matter in the evolution of the universe. The results shown here will be joined with supersymmetry in the next section to give a complete picture of the “WIMP miracle.” This served as a motivation for TeV-scale DM searches in the past and is the historical origin of many direct detection experiments, although recent null results have put heavy constraints on the TeV-scale WIMP.

1.2.1 Curved Spacetime

Per Einstein’s theory of general relativity, spacetime is not Euclidean, but curves depending on the energy distribution within it. If the universe is assumed to be homogeneous and isotropic, its curvature is smooth and can be characterized by two quantities:

- The *curvature constant* $\kappa \in (-1, 0, +1)$, which corresponds to if the universe is respectively open, flat, or closed.
- The *radius of curvature* R , which is uniform across all space.

If we’re dealing with gravitational effects and not just empty space, spatial distances may also expand or contract with time. Again, in a homogeneous and isotropic universe, we account for this using a *scale factor* $a(t)$, for a total of three quantities that characterize the universe completely. Of course, locally the universe is not actually homogeneous and isotropic, but when considering large scales (i.e. the universe as a whole) this approximation is generally valid.

The three quantities κ , R , and $a(t)$ can be related to the homogeneous energy density $\varepsilon(t)$ using the Friedmann equation:

$$H(t)^2 = \left(\frac{\dot{a}}{a}\right)^2 = \frac{8\pi G}{3c^2}\varepsilon(t) - \frac{\kappa c^2}{R^2} \frac{1}{a(t)^2} \quad (1.5)$$

where $H(t) = \dot{a}/a$ is the Hubble parameter, and its present-day value $H_0 = H(t_0)$ is the Hubble constant.

For a flat universe ($\kappa = 0$), only the first term on the RHS of the Friedmann equation is nonzero. This gives an expression for the energy density required for a

flat universe, or the *critical density*:

$$\begin{aligned}\varepsilon_c(t) &= \frac{3c^2}{8\pi G}H(t)^2, \text{ or,} \\ \rho_c(t) &= \frac{3}{8\pi G}H(t)^2\end{aligned}\tag{1.6}$$

where the latter is the equivalent mass density $\rho = \varepsilon/c^2$.

When discussing the composition of the universe, it is convenient to use instead the relative density, or the dimensionless *density parameter*:

$$\Omega_X(t) = \frac{\varepsilon_X(t)}{\varepsilon_c(t)} = \frac{\rho_X(t)}{\rho_c(t)}\tag{1.7}$$

which compares the density of any mix of particle species X with the critical density. Our best measurements today show that the universe is very nearly flat ($\Omega_0 \sim 1$) [11].

1.2.2 The Λ CDM Model

As the universe expands, its energy density tends to decrease. Naively, we might expect that the homogeneous energy density falls as $\varepsilon(t) \propto a(t)^{-3}$, where particles simply drift farther apart in three-dimensional space. This is valid for non-relativistic matter, but is not true for other types of energy: radiation experiences redshift in addition to spatial spreading, and falls as $\varepsilon_{\text{rad}}(t) \propto a(t)^{-4}$.

Using the present-day Hubble constant H_0 , density parameter Ω_0 , and critical density $\varepsilon_{c,0}$ shown in the previous section, the Friedmann equation (Eq 1.5) can be rewritten in a more evocative way:

$$\left(\frac{H(t)}{H_0}\right)^2 = \frac{\varepsilon(t)}{\varepsilon_{c,0}(t)} + \frac{1 - \Omega_0}{a(t)^2}\tag{1.8}$$

where the present-day scale factor a_0 is normalized to 1. In this formula, the first term describes the energy density evolution and the second term describes the curvature; together, they provide a complete picture of the shape and content of a homogeneous isotropic universe.

With these tools, we can introduce the Λ CDM (Λ -cold dark matter) model,

Type	Symbol	Value
Baryonic	Ω_b	0.0493(6)
Cold Dark Matter	Ω_c	0.265(7)
All Matter	Ω_m	0.315(7)
Photons	Ω_γ	$5.38(15) \times 10^{-5}$
Neutrinos	Ω_ν	< 0.003
Dark Energy	Ω_Λ	0.685(7)

Table 1.1: Measured values for various density parameters, produced by the *Planck* Collaboration [11] and compiled in Ref [12]

which parameterizes the overall present-day density parameter Ω_0 into four distinct components. Written as a Friedmann equation (Eq 1.8), this is:

$$\left(\frac{H(t)}{H_0}\right)^2 = \frac{\Omega_b + \Omega_c}{a(t)^3} + \frac{\Omega_{\text{rad}}}{a(t)^4} + \frac{\Omega_\Lambda}{a(t)^0} + \frac{1 - \Omega_0}{a(t)^2} \quad (1.9)$$

where the subscript b is for non-relativistic baryonic matter, c for cold dark matter, rad for radiation (including relativistic matter), and Λ for the cosmological constant (or dark energy). The “cold” dark matter distinction here is important, as it refers to non-relativistic matter; on the other hand, ultrarelativistic matter, such as neutrinos, is radiation-like, and is more properly included in Ω_{rad} . The curvature term is frequently dropped, as measurements have shown that $\Omega_0 \sim 1$ and the universe today is nearly flat [12]; however, a nonzero curvature is not in itself prohibited by Λ CDM.

Currently, these density parameters are best constrained using measurements of temperature fluctuations in the Cosmic Microwave Background (CMB) – photon radiation emitted in the very early universe that permeates the universe today. The CMB is fairly even, with small fluctuations that reflect inhomogeneities in the plasma from which the CMB photons were released. Then, the size of these energy fluctuations can be numerically fit to a matter distribution, which yields the relative densities of matter and radiation at the time of CMB emission. A more detailed description of this process can be found in Ref [11].

Measurements made using the method outlined above are provided by the *Planck* Collaboration, shown in Table 1.1. These values independently confirm the

astronomical observations discussed in the previous sections of this thesis. First, the ratio of dark matter to baryonic matter is ~ 5 , consistent with the estimate made in Section 1.1.1 that stellar mass makes up $\sim 10^{-1}$ of the total galactic mass (recall that, in addition to stellar mass, there are large amounts of non-luminous baryonic matter in the form of gas, dust, and MACHOs). The very small neutrino density also rules out the possibility that neutrinos make up the bulk of dark matter.

It is important to remember that these values are not fixed in time, as they depend on $a(t)$ in different ways. The very early universe was dominated by radiation, which quickly fell in favor of matter, and today the universe is dominated by dark energy.

1.2.3 Dark matter freeze-out

We will now discuss how the abundance of a specific dark matter candidate (an unknown particle X) might evolve in time to reproduce the dark matter density we see today. The derivation of various formulae in this section generally follow the discussion in Refs [30, 31].

In the very early universe, temperatures were much higher than the DM rest mass m_X . Dark matter annihilation into lighter Standard Model (SM) particles ($X\bar{X} \rightarrow L\bar{L}$) would have occurred at about the same rate as the reverse process ($L\bar{L} \rightarrow X\bar{X}$), putting DM particles in chemical equilibrium with all SM particle species. According to basic thermodynamics, the relationship between DM number density and temperature would have been:

$$n_X(T \gg m_X) \propto T^3 \tag{1.10}$$

As temperatures dropped below the DM rest mass, the $L\bar{L} \rightarrow X\bar{X}$ process became exponentially suppressed and the chemical equilibrium was broken. The DM number density can then be expressed as a Boltzmann distribution, where DM particles are modeled as a higher-energy thermal state of the lighter SM particles:

$$n_X(T < m_X) \propto T^3 \exp(-m_X/T) \tag{1.11}$$

Note that although chemical equilibrium is broken here, thermal equilibrium per-

sists between the DM and SM particles. Over time, if the universe remains in thermal equilibrium, the DM number density should trend towards zero.

If the expansion of the universe accelerates to the point where the expansion rate exceeds the DM annihilation rate, the DM particles fall out of thermal equilibrium and annihilation slows or ceases. That is, the average distance between DM particles and antiparticles grew far enough apart that annihilation reactions must have become very rare. This phenomenon is known suggestively as “freeze-out,” which preserves the large DM abundance or “relic density” Ω_X we see today.

To determine the relic density, we must solve the Boltzmann transport equation for a system not in equilibrium:

$$\frac{dn_X}{dt} = -\langle\sigma v\rangle [n_X^2 - (n_X^{\text{eq}})^2] \quad (1.12)$$

where $\langle\sigma v\rangle$ is the average DM annihilation cross section and n_X^{eq} is the DM number density assuming thermal equilibrium.

As the universe expands, its temperature cools monotonically and can be used as a surrogate for time and the scale factor. Using T instead of t is particularly useful here, as point at which DM and SM particles fall out of chemical equilibrium is defined by $T = m_X$. It is therefore customary to rewrite Eq 1.12 as a derivative over $x = m_X/T$.

Furthermore, the number density of any particle species naturally decreases as the universe expands. To isolate annihilation, we want to define a *comoving* number density $N_X = n_X/s$ normalized to the average entropy density, such that the post-freeze out comoving number density reaches a constant N_X^∞ . The average entropy density decreases monotonically with expansion and is suited for this task. Then, the modified Boltzmann transport equation reads:

$$\frac{dN_X}{dx} = \frac{-\lambda}{x^2} [N_X^2 - (N_X^{\text{eq}})^2], \quad (1.13)$$

$$\text{where } \lambda = \frac{2\pi^2 g_{*S} m_X^3 \langle\sigma v\rangle}{45 H(T = m_X)}$$

where g_{*S} is the effective number of relativistic degrees of freedom, a linear combination of the number of degrees of freedom of each particle species. In reality, g_{*S}

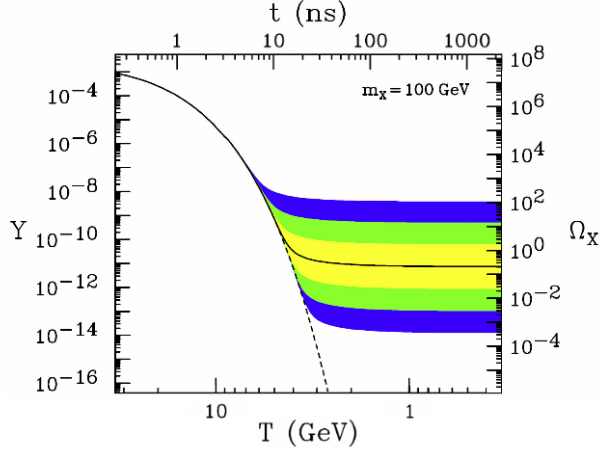


Figure 1.3: Comoving particle number N_X or Y and relic density Ω_X (y-axis) versus temperature T and time t (x-axis). The solid line is a numerical solution to Eq 1.13 that matches the observed DM relic abundance, whereas the dotted line projects DM depletion without freeze-out. Colored regions indicate solutions for cross-sections that differ by 10 , 10^2 , and 10^3 respectively. Plot taken from Ref [17].

varies with T , but we will assume that it is roughly constant in the epochs relevant to this discussion.

For a given λ , Eq 1.13 can be solved numerically to yield the comoving number density at any point in time. Since $\rho_{X,0} = m_X \times n_X^\infty$, we can also calculate the relic density parameter Ω_X . Fig 1.3 shows the comoving number density and relic density solved for different cross sections. As we might intuitively expect, a larger annihilation cross section should produce a higher λ and, in turn, a smaller DM relic abundance, since annihilation should remain relevant as a process of DM particle depletion for a longer period of time.

Since we have good empirical measurements of the overall DM density Ω_c , we can work backwards to determine the DM particle cross section. For our known Ω_c from Table 1.1, the DM annihilation cross section is [30]:

$$\langle\sigma v\rangle\sim 10^{-8}\text{ GeV}^{-2}\sim 10^{-3}G_F\quad(1.14)$$

where G_F is the Fermi coupling constant for weak interactions. In other words, the DM cross section is on the weak scale, confirming the independent observation made from the Bullet cluster that dark matter should be weakly self-interacting.

1.3 The WIMP in Particle Physics

In the previous section, we predicted the annihilation cross section of a dark matter particle and the weakly-interacting character of the WIMP using cosmology alone. Here, we will present an overview of supersymmetry and its fortuitous convergence with dark matter cosmology in predicting the mass scale of a hypothetical particle.

Again, it should be noted that the “WIMP miracle” *as such* has been ruled out by consistent null results from direct detection experiments (with some notable yet heavily disputed exceptions that will be discussed in Section 1.4). Nevertheless it served as the historical motivator of the earlier CDMS experiments, and as a starting point for expansions of the WIMP model in vogue today. SuperCDMS itself searches for DM signals generically across all models of \sim GeV mass range, as an initial expansion from the TeV mass range of the basic WIMP. Other experiments, which might probe e.g. \lesssim eV masses, are historically related to other theories.

1.3.1 The Hierarchy Problem

The Standard Model of particle physics predicts the existence of the Higgs boson and a corresponding complex scalar Higgs field. The potential of the Higgs field is:

$$V = m_H^2 |H|^2 + \lambda |H|^4 \quad (1.15)$$

which is unique as it forms a “Mexican hat” shape with no single minimum, allowing the Higgs field to spontaneously break symmetry and giving the Higgs field its interesting properties, most of which are beyond the scope of this thesis.

The parameters in Eq 1.15 have been experimentally determined with the discovery of the Higgs boson in 2012 [32]. Theoretically, however, the m_H^2 factor is also extremely sensitive to any quantum corrections from couplings to the Higgs field. The one-loop corrections to m_H^2 are slightly different for couplings to

fermions versus bosons:

$$\Delta m_H^2 = \frac{-|\lambda_f|^2}{8\pi^2} \Lambda_{UV}^2 + \dots \text{ (for fermions)} \quad (1.16)$$

$$\Delta m_H^2 = \frac{|\lambda_S|^2}{16\pi^2} [\Lambda_{UV}^2 - 2m_S^2 \ln \Lambda_{UV}/m_S \dots] \text{ (for bosons)} \quad (1.17)$$

where both are quadratically dependent on “ultraviolet cutoff” Λ_{UV} , or the highest energy at which the SM is expected to be valid (and hence the energy scale at which new, higher energy physics become necessary). For a large (e.g. Planck scale) Λ_{UV} , the correction Δm_H^2 becomes untenably larger than the experimentally verified m_H^2 itself! This known as the “hierarchy problem,” where the observed physical quantity can only be reproduced when large corrections are canceled out with incredibly fortunate fine-tuning. If our universe is assumed to be typical, then this presents a real problem.

1.3.2 Supersymmetry

A potential solution to the hierarchy problem lies in the very suggestive opposing signs between the quadratic terms of Eqs 1.16 and 1.17. If a new theory can combine the two terms by relating fermions and bosons, these problematic terms might cancel out, giving us a relatively small overall Δm_H^2 without the need for fine-tuning.

Theories of supersymmetry (SUSY) attempt to do exactly this. SUSY postulates that, for each fermion or boson in the SM, there must exist a “superpartner” boson or fermion that transforms into SM particles under the new symmetry. For SUSY to be realistic, though, a few extra concepts have to be introduced:

1. Soft SUSY breaking: The fact that no superpartner has been identified so far suggests that SUSY is broken, such that the superpartners have very different (i.e. larger) masses compared to the known SM particles. However, for the leading Δm_H^2 terms to still roughly cancel, the symmetry breaking must be “soft,” which requires an extra m_{soft} parameter to suppress all symmetry-breaking terms at high enough energies.
2. R-Parity: SUSY opens the possibility for baryons to decay into leptons, and

vice versa, by exchange of superparticles. However, the conservation of baryon and lepton numbers have been verified very stringently, and any such conversions between the two must be very rare or nonexistent. R-Parity is an extra symmetry added to SUSY to suppress such couplings, which has the benefit of preventing SM particles from decaying into superparticles. There must then be at least one superparticle that is stable, referred to as the Lightest Supersymmetric Partner (LSP). [33]

Together with base SUSY, soft SUSY breaking and R-Parity form the basis of the Minimally Supersymmetric Standard Model (MSSM), an extension of the SM with the least number of changes that is still consistent with experimental evidence.

The LSP, being non-SM, uncoupled from baryons, and stable, can exist in high abundances throughout the universe and is a natural dark matter candidate. Remarkably, the LSP also has an energy scale close to that predicted by cosmological observations. The soft symmetry-breaking parameter m_{soft} provides a mass scale for SUSY particles to be around 1000 GeV or less [34]: the neutralino is traditionally the most common LSP candidate and has a predicted mass range of around 50 to 1000 GeV.

Using 1.13 and requiring that the annihilation cross section $\langle\sigma v\rangle$ be on the weak scale (i.e., $\sim G_F$), the DM mass must be ~ 1000 GeV to match the observed DM relic abundance [31], which is the same as the mass scale of the LSP. That is, DM freeze-out and the MSSM may be predicting the same particle! This is a remarkable coincidence – so remarkable that it has been called the *WIMP miracle*. It also figures as a natural starting point for searches of dark matter, as two independent models appear to lend credence to each other, and a successful detection of the LSP WIMP would confirm both.

1.4 Dark Matter Detection

Recent detection experiments have more or less ruled out the standard LSP WIMP as a DM candidate. The parameter space between LSP energy range $10 \sim 1000$ GeV has been increasingly thoroughly investigated, yet no definitive evidence of a WIMP has been found. In this section, we will discuss the types of DM detection experiments available, with a special focus on direct detection as employed at

SuperCDMS. We will also provide an overview of dark matter findings thus far.

1.4.1 Indirect Detection

Also known as astrophysical searches, indirect searches look for cosmic rays originating from predicted DM-dense regions of space, with properties that cannot be conventionally explained. Specifically, these include gamma rays, neutrinos, and antimatter particles that may be produced by DM annihilation and decay. Lighter DM particles may also be produced in stars, and in turn interfere with typical stellar processes with possibly measurable effects.

Some indirect search experiments have claimed excesses in expected signal regions. For example, data from the Fermi Gamma Ray Space Telescope have reported gamma ray excesses from the inner galaxy indicating WIMPs of $\sim 10\text{GeV}$ [35]. Several other experiments have also reported excesses in high-energy positrons consistent with more complicated DM models [36]. These findings are controversial, as they are not reproduced in other detection channels, nor are they unique or strongly indicative of dark matter: in both cases, many plausible non-DM hypotheses have been pitched as alternative explanations [12].

1.4.2 Accelerator Searches

Dark matter experiments at accelerators, principally the LHC, attempt to identify dark matter in the aftermath of particle collisions [37]. Usually, it is assumed that any DM particles produced in the collider will not interact with detectors, and will instead present as imbalances in detectable SM particles. For instance, when known particles show missing transverse energy or momentum, it may be assumed by conservation laws that one or more unknown particles have escaped unnoticed; in this case, further investigation and comparison with other types of DM detection are necessary to confirm that the missing particle is, in fact, dark matter [12].

Another possibility is that a DM mediator is produced and subsequently decays into an SM particle-antiparticle pair (or a “dijet” event) – if a DM particle can be created in a collision of SM particles, then it should be able to decay into SM particles as well. Instead of a missing particle, this registers as a bump in the detected dijet mass or angular distributions [37]. These types of DM candidates

go beyond the basic LSP hypothesis and are predicted by a range of dark sector theories (Section 1.5).

Currently, the main experiments performing accelerator DM searches are CMS and ATLAS. Neither have detected either type of DM signal thus far, though they are placing increasingly stringent limits that can be used in conjunction with direct detection experiments [38].

1.4.3 Direct Detection

As the name suggests, direct detection experiments look for scattering from DM particles with the detector material directly. Generally, for the predicted velocity and mass ranges of WIMPs, these are expected to be elastic scattering off of atomic nuclei. Inelastic or electron scattering, where WIMPs either excite or ionize orbital electrons, may also be significant, particularly for certain low-mass DM models.

For a known density and velocity distribution, there are two main unknown parameters that characterize WIMP candidates and their projected event rates: WIMP mass m_X and the WIMP-nucleon scattering cross section σ_0 . Direct detection experiments investigate different ranges of m_X and σ_0 , and have thus far established “exclusion limits” in m_X and σ_0 where WIMPs have not been found. The exclusion limits established by various experiments can be directly compared and are plotted nicely on Fig 1.4.

The direct detection exclusion curves tend to rise rapidly in cross section at low mass. This is a limit imposed by the nuclear recoil energy, which is dependent on the WIMP mass [39]:

$$E_r = 2v^2 \frac{\mu^2}{m_A} \cos^2 \theta_r \quad (1.18)$$

where m_A is the target nuclear mass, $\mu = m_X m_A / (m_X + m_A)$ is the reduced WIMP-nucleus mass, v is the WIMP velocity in the lab frame, and θ_r is the scattering angle. As the WIMP mass decreases, so too does the nuclear recoil energy until it falls to the level of the detector noise. The inability of detectors to resolve low-energy nuclear recoils from noise is the main limiting factor in exploring the low-mass region, and overcoming this limit requires either reducing noise dramatically or amplifying the recoil signal.

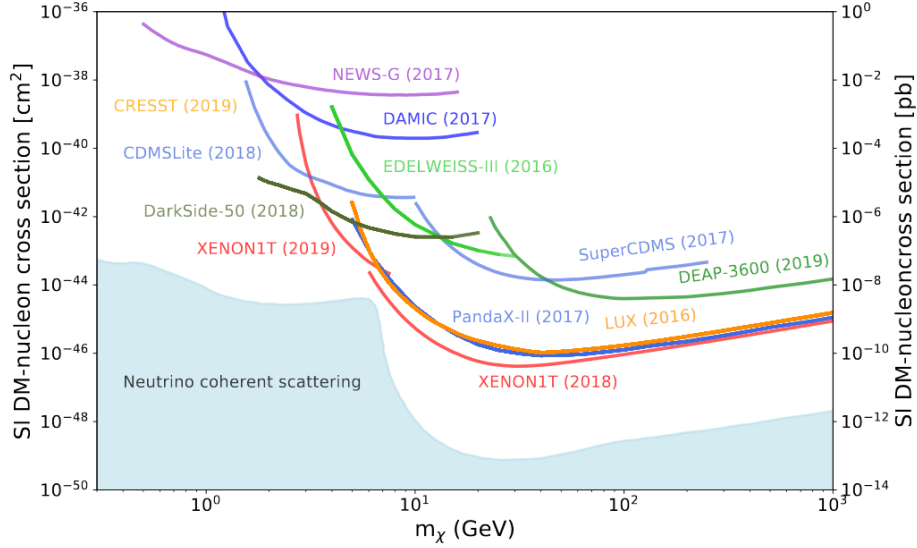


Figure 1.4: Exclusion limits published by various direct detection experiments, accurate up to 2020. Plot taken from [12]

It is also important to note that σ_0 is different for spin-dependent (SD) versus spin-independent (SI) scattering. In the former, WIMPs are coupled to the nucleon spin, with cross sections dependent on the total nuclear angular momentum J ; in the latter, WIMP scattering is dependent on the nuclear mass instead, where all nucleons add coherently to the cross section [40]:

$$\sigma_{0,SD} = \frac{32\mu^2}{\pi} G_F^2 (J+1) [a_p \langle S_p \rangle + a_n \langle S_n \rangle] \quad (\text{Spin-dependent}) \quad (1.19)$$

$$\sigma_{0,SI} = \frac{4\mu^2}{\pi} [Zf_p + (A-Z)f_n]^2 \quad (\text{Spin-independent}) \quad (1.20)$$

where the subscripts p and n refer to proton and neutrons respectively, G_F is Fermi's coupling constant, μ^2 is the reduced nuclear mass, $\langle S \rangle$ is the spin expectation value, Z is the number of protons, and A is the number of protons in the target nucleus. The parameters a and f characterize WIMP coupling to nucleons.

Since in Eq 1.20 the cross section is quadratically related to nucleon number, it may be useful when probing spin-independent scattering to select a heavier element

as the detector medium (this is not the only factor in material selection, however). On the other hand, targets with high nuclear spin are limited, so overall, spin-dependent scattering is much harder to investigate. As such, the σ_0 quoted in direct detection experiments is by convention the *spin-independent* cross section.

Increasingly sensitive direct detection techniques have pushed deeper and deeper into the WIMP and, increasingly, nonstandard WIMP or non-WIMP parameter space (Fig 1.4), with no conclusive signal yet found. The latest generation of detectors have very nearly begun to detect coherent neutrino-nucleus scattering, a background of neutrino events that both resemble WIMP signals and cannot be shielded [41]. In this region, any WIMP discovery will need to show an excess much greater than the statistical fluctuations of the neutrino background, which will pose a significant challenge and requires new particle discrimination techniques.

One interesting exception to the reports of null results is the DAMA/LIBRA experiment, which has over the past decades reported increasingly stringent measurements of an annual modulation consistent with the periodic movement of Earth through DM-filled space [42]. These findings are very controversial, however, as it is difficult to show conclusively that annual modulations are not caused by any number of seasonal effects, and the DAMA/LIBRA results have yet to be reproduced independently, using the same methods or otherwise [12, 43].

1.5 Low-Mass Dark Matter Hypotheses

Despite the great promise and fortuitousness of the WIMP miracle, its characteristic parameter range has been more or less ruled out. It has therefore become increasingly necessary for dark matter experiments to consider a larger parameter range motivated by non-MSSM, non-SUSY, or altogether non-WIMP theories.

Of particular relevance to SuperCDMS and this thesis are low-mass DM candidates. Many of these fall under the “Hidden Sector” umbrella, which postulates that DM does not interact with SM under SM forces, but under new forces with new mediator particles. Hidden sector models also allow for a range of DM production and destruction scenarios, which with the experimentally observed DM relic abundance predicts mass ranges that overlap with the MSSM WIMP on the high end (\sim GeV) and extends down to the keV range on the low end. Aside from

typical thermal freeze-out, some interesting ones are [44]:

- Secluded Freeze-out: The DM particle couples to SM via a mediator particle lighter than itself ($m_{\text{med}} < m_X$). The DM annihilation cross-section is dependent on the DM-mediator coupling, which is distinct from the mediator-SM coupling – freeze-out of the former may occur while the latter continues with SM interactions. [45]
- Asymmetric DM: The DM particle and antiparticle have a primordial asymmetry similar to the baryonic asymmetry. In this case, the DM relic abundance is set not by suppression of annihilation in freeze-out, but by the excess of DM particles over antiparticles [46].
- Freeze-in: DM particles coupled very weakly to SM may never have entered thermal equilibrium. Such DM particles rarely annihilate and, instead of depleting and freezing-out, are continuously accumulated by decays from SM particles [47].

These are only a sample of the types of hidden sector models available. More complete summaries can be found in Ref [44] and in the PDG overview of dark matter [12]. Suffice to say, though, that after the conventional WIMP is ruled out, there is no shortage of models and parameter space to explore.

Chapter 2

The SuperCDMS Experiment

SuperCDMS (Super Cryogenic Dark Matter Search) is a direct detection experiment aimed at expanding the search for WIMPs to lower (\lesssim GeV) mass ranges [18]. It is the current generation of the CDMS experiments, which previously probed the standard GeV \sim TeV mass range of WIMPs and [48, 49], alongside the wide array of other direct detection experiments, have ruled out much of that parameter space for dark matter [12].

The main upcoming SuperCDMS experiment is currently under construction \sim 2 km underground at SNOLAB, near Sudbury, Ontario. The rock overburden provided by SNOLAB is expected to eliminate most cosmic radiation backgrounds and, in addition to improvements in the shielding and the detectors themselves, will allow new limits to be set on the DM parameter space. The projected range of the upcoming SuperCDMS experiment, along with the sensitivity ranges of previous experiments, are shown in Fig 2.1.

2.1 Theory of Operation

The detectors used at SuperCDMS are solid-state phonon and charge calorimeters that measure the energy deposit and/or ionization produced from incident particles. Generally, these are cylinders of high-purity semiconductor crystals (Si or Ge), though newer test devices can vary significantly in size and shape. The crystals are instrumented on both circular faces with sensors in different patterns and channel

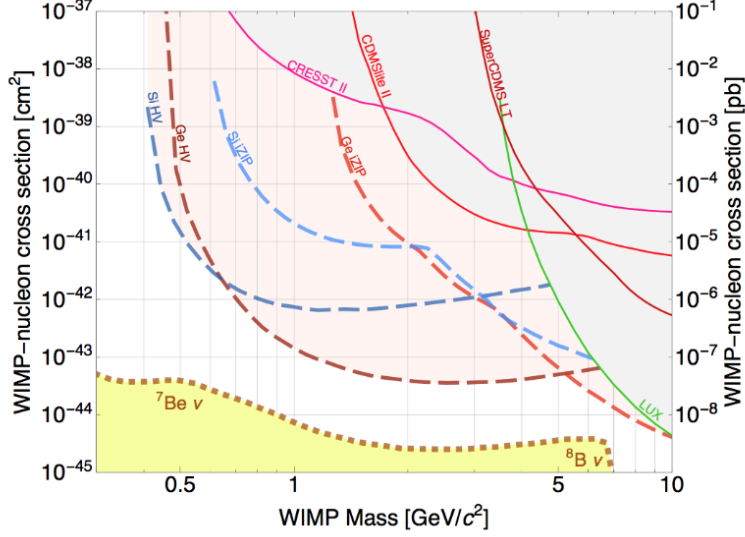


Figure 2.1: Projected sensitivity of the SuperCDMS detectors at SNOLAB, in terms of the DM direct detection parameter space. Figure taken from Ref [18].

configurations, depending on the detector type.

As an incident particle travels through the detector crystal, it may transfer energy to either atomic nuclei or electrons. These interactions are classified respectively as nuclear recoils (NR) or electron recoils (ER). In both cases, some amount of energy is deposited as vibrations in the crystal lattice called *phonons*, that then propagate to the detector sensors.

If the recoil energy is greater than the bandgap energy $\varepsilon_{gap} \approx 1.1$ (0.67) eV in Si (Ge) [50], the interaction may also produce electron-hole pairs. By applying a voltage between the detector faces, the electron-hole pairs can be split and drifted towards opposite faces. Since the quasiparticle holes behave as free positive charges they, together with the negative electrons, are also known as *charge carriers*.

The detector voltage may also activate the Neganov-Trofimov-Luke (NTL) effect, where drifted charge carriers produce additional “NTL” phonons. The total phonon energy E_{ph} is thus also split between “prompt” phonons produced by the

recoil itself and NTL phonons [19]:

$$\begin{aligned} E_{NTL} &= n_{eh} \cdot e \cdot V, \\ E_{ph} &= E_r + E_{NTL} \end{aligned} \quad (2.1)$$

where E_{NTL} is the total NTL phonon energy, E_r is the recoil energy, n_{eh} is the number of electron-hole pairs produced, V is the bias voltage, and e is the elementary charge. The number of electron-hole pairs can itself be written in terms of a *charge yield* $y(E_r)$:

$$\begin{aligned} n_{eh} &= y(E_r) \frac{E_r}{\varepsilon_{eh}}, \\ E_{ph} &= E_r \left(1 + e \cdot V \cdot \frac{y(E_r)}{\varepsilon_{eh}} \right) \end{aligned} \quad (2.2)$$

where ε_{eh} is the average energy required to produce an electron-hole pair, at $\varepsilon_{eh} \approx 3.8$ (3.0) eV in Si (Ge) [51]. For electron recoils, $y(E_r) \equiv 1$; for nuclear recoils, $y(E_r)$ is nontrivial but generally ranges from 0 ~ 30% [19].

The form of Eq 2.2 suggests two distinct modes of operation: low-voltage (LV) and high-voltage (HV). In LV operation, phonon production from the initial recoil event dominates; charge carriers do not contribute significantly to the phonon energy, and the measured phonon and charge energies can be compared to determine the ionization yield $y(E_r)$ and discriminate between NR and ER events.

In HV operation, NTL phonon production from charge carriers is significant, and there is much overlap between detected phonon and charge energies as the former becomes proportional to the latter [19]. As a result, HV operation lacks ER/NR discrimination but has the benefit of amplification – low-energy events that produce a small number of charge carrier pairs and an imperceptible primary phonon signal may instead be detected by their NTL phonons. This alleviates in part the noise problem described in Section 1.4.3 that limits DM detection at low masses.

Once phonons and charge carriers are propagated to the detector surfaces, the signals be read out separately with different sensors. Phonons are primarily measured with QETs, or Quasiparticle trap-assisted Electrothermal-feedback

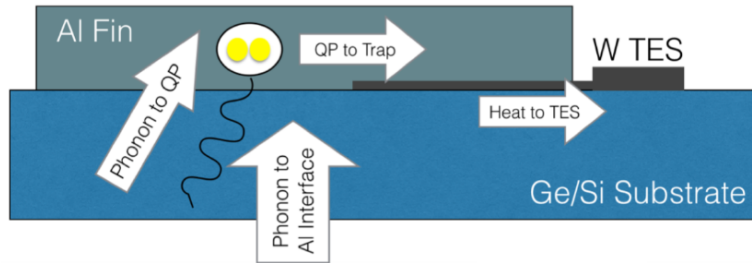


Figure 2.2: Simple schematic describing the function of a QET: phonons entering from the crystal produce quasiparticles (QP) in the aluminum fin, which are trapped and deposit heat into the tungsten TES. Figure taken from Ref [19].

Transition-edge sensors. These are a special type of transition-edge sensor (TES), which are kept just below their superconducting transition temperatures, such that even a small phonon signal can heat the TES enough to cause a large change in resistance. In this case, each QET is composed of a tungsten film attached to aluminum fins (Fig 2.2), which are kept as close to the tungsten superconducting temperature as possible.

Generally, TES sensitivity depends on its susceptibility to temperature changes – a larger TES has a larger total heat capacity, and takes more energy to produce a unit change in energy. QETs are unique to other TESs by their inclusion of aluminum fins, in which phonons produce quasiparticles that are then propagated to and trapped in tungsten. The surface area of the sensor is increased as the aluminum fins “funnel” phonons to the TES, whereas the TES mass and heat capacity are maintained. More about QET physics and design can be found in Ref [19, 20].

Charge carriers are instead absorbed by electrodes held at the bias voltage, then fed into FET (Field Effect Transistor) amplifiers where the charge signal can be read out. Together with QETs, these electrodes are distributed over the entire detector face in a dense pattern. These sensors can be divided into several distinct channels (Fig 2.3) to provide some position sensitivity based on the relative shapes, amplitudes, and timing of pulses generated in each channel.

Finally, signals from the QETs and FETs are sent to the room-temperature instrumentation, where they are digitized by a Detector Control and Readout Card

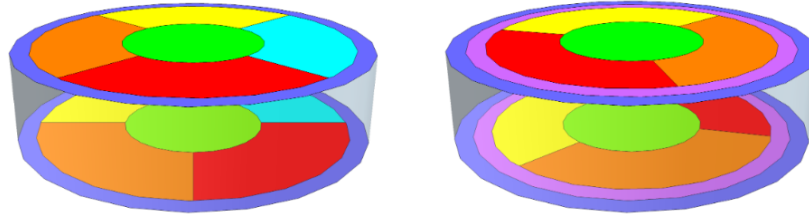


Figure 2.3: Phonon channel layout of the iZIP detector (left) and the HV detector (right). In addition, iZIPs have two charge channels; the outer charge channel overlaps with the outer phonon channel, and the inner charge channel with the remaining phonon channels. HV detectors have no charge channels. Figure taken from Ref [20].

(DCRC) and stored in a buffer [52]. The DCRC then applies triggers to the buffered data: to save processing power and storage space, events that do not pass the trigger condition are discarded, whereas triggered events are saved for further offline cuts and analysis. The stringency of the trigger condition imposed determines the trigger efficiency, rate, and energy threshold, the latter of which will be minimized as much as possible when searching for low-mass DM.

2.2 Detector Types

SuperCDMS currently operates two flagship detector types at SNOLAB, along with a slew of test devices at SNOLAB, Fermilab, SLAC, and various aboveground laboratories. All SuperCDMS detectors are solid-state charge- and/or phonon-readout calorimeters, and function by the physical processes and sensors described in the previous section. The detector crystals are alternately made of silicon or germanium; these materials complement each other as silicon has a lower recoil kinematic cutoff and is sensitive to lower masses, whereas germanium has fewer radioactive backgrounds [20].

2.2.1 iZIP and HV

The two flagship SuperCDMS detector types, iZIP and HV, use semiconductor crystals in cylinders 100 mm in diameter and 33.3 mm thick [18]. Each type can be made of either silicon or germanium, to facilitate comparisons between the two

materials. Generally, these detectors are arranged in stacks (“towers”) including the copper housing, clamps, wiring, and various instrumentation needed for signal readout and some shielding. The tower layout allows events coincident in multiple detectors to be vetoed, as a single DM particle is very unlikely to interact more than once in its trajectory.

The iZIP and HV devices differ by their phonon and charge sensor patterns and operating bias voltage. Their specific design and purpose are as follows:

- iZIPs, or interleaved Z-dependent Ionization and Phonon detectors, feature six phonon and two charge channels per face, where phonon and charge sensors occupy the same space and are hence “interleaved” (Fig 2.3). These are operated at lower bias voltages (typically ± 4 V), which, per Eq 2.2, allows for ER/NR discrimination by measuring the relative charge yield.

Events near the surface tend to exhibit reduced charge signals due to charge carrier trapping at the crystal surface. As such, ER surface events, which should have a charge yield of $y(E_r) = 1$, may be misidentified as lower charge yield NR events. To identify and potentially reject these surface events, a special charge biasing scheme is introduced, where the charge sensor electrodes on each surface are interleaved with grounded electrodes (i.e. the QET phonon sensors). Close to the surface, this pattern produces a local electric field oriented parallel to the surface, whereas in the crystal bulk the electric field is very nearly axial. Surface event charge carriers are therefore made to drift towards interleaved electrodes on the same detector face, whereas bulk charge carriers are split and drifted towards different faces as usual. A more detailed discussion of surface event handling can be found in Ref [53].

ER/NR discrimination has been especially useful in the past, when it was assumed that WIMPs would scatter off of atomic nuclei, and ER events could be straightforwardly rejected. With the expansion of searches to lower masses, however, it becomes increasingly necessary to consider lower energy events. The iZIP energy resolution becomes severely limited for events below ~ 10 keV, and a different type of detector able to handle lower energies must be used in conjunction.

- The HV or High Voltage detectors, as their name suggests, are kept at higher voltages (~ 100 V) to exploit the NTL effect (Section 2.1) for phonon signal amplification; per Eq 2.2, for an average electron-hole pair energy of $\epsilon_{eh} \sim 3$ eV, the signal is increased by a factor of ~ 30 relative to the initial recoil energy. Because of this, much lower energy thresholds can be used in comparison to iZIP detectors, and lower energy events (including ER events) can be properly studied.

All else held constant, the bias voltage can simply be increased to explore lower and lower energy events. In reality, however, this is limited by voltage-dependent noise sources that may come to dominate, and currently ~ 100 V gives the best tradeoff between signal amplification and new noise sources [20].

Since the phonon signal is dominated by NTL phonons, the phonon and charge signals in an HV detector are degenerate, and ER/NR discrimination becomes difficult or impossible. In fact, the HV detector lacks charge sensors altogether, as well as surface event identification, which necessitates running iZIP and HV detectors side-by-side for a complete picture of backgrounds and any potential DM particles.

2.2.2 HVeV

The HVeV (High Voltage, eV-scale) detectors are made of silicon crystal in small, square chips ~ 1 g in mass and $10 \times 10 \times 4$ mm³ in volume (or about 1/2600 the size of iZIP and HV detectors!) [20]. The top face of each chip is lined with QETs and no charge sensors, whereas the bottom has an aluminum grid for voltage biasing. As with the HV detectors, HVeVs are operated at high voltages for NTL amplification, with no built-in ER/NR discrimination.

A major and unexplained source of noise in all high-voltage detectors is the *leakage current* or *charge leakage*. Generally, the leakage current consists of Poisson-distributed single charge carriers, thought to “leak in” from as-yet unknown sources that then produce a background NTL phonon noise. Possible origins include effects at the electrode-crystal interface or induced e-h pair production in the crystal bulk; either way, the leakage current density depends on the size of

the detector, and the small size of the HVeV detector is able to greatly reduce its effects [20, 54].

The HVeV detector was designed as a test device to study advances in QET energy efficiency. Thus far, it has only been operated aboveground, with relatively lax background elimination; even then, it has achieved a sub-eV energy resolution and a threshold below the silicon bandgap energy, which lets it differentiate between single- and multiple-electron ionization events in detail. This, in turn, will be very useful in analyzing noise sources and low-energy backgrounds (Chapter 3), and has allowed HVeV to set new limits on the DM parameter space [54, 55]. Future deployment of HVeV underground will provide further insight, with the aim of improving noise reduction in the much larger HV detectors.

2.2.3 CPD/LAPD

Known internally as PD2, the CPD (Cryogenic PhotoDetector) or LAPD (Large Area PhotoDetector) is a large, thin, circular silicon wafer of 38.1 mm in radius and 1 mm in thickness, weighing a hefty 10.6 g. It is instrumented on one side, with phonon sensors only, distributed sparsely and connected to a single readout channel [56]. Currently, CPD is tested for DM detection underground at CUTE, with aboveground results in preparation for publication.

CPD has achieved a relatively low baseline energy resolution of ~ 4 eV and a recoil energy threshold of 16.3 eV, without a bias voltage for NTL amplification or stringent background elimination [56, 57]. Instead, it improves its resolution and threshold with high efficiency and a low QET critical temperature. Notably, CPD uses a preexisting detector design from the CPD Collaboration for non-DM rare event searches, and its namesake large surface area is not itself ideal for DM detection – the energy resolution and threshold can be even further improved with a decrease in instrumented area and an increase in volume [57].

2.3 Detector Backgrounds

In previous sections, we briefly discussed the detector signal-noise ratio as the key factor in limiting energy resolution and low-mass parameter reach (as opposed to, for instance, the crystal bandgap energy or quantum mechanical uncertainty). The

source of this noise is the detector background, which, broadly defined, can be anything that might mimic or obscure a genuine dark matter event.

In this section, we will primarily discuss the well-studied radiogenic backgrounds at SuperCDMS SNOLAB, which will be useful when investigating unexplained low-energy backgrounds later on in this thesis. Generally, these are emitted from radioactive decay, which we will divide into external and internal radiation, depending on where the decay occurred relative to the detector shielding.

The internal radiation can be further divided into *bulk* and *surface* radiation. In the former, the radioisotopes are distributed throughout apparatus materials, and in non-detector materials their radiation must escape the material itself, where they may be absorbed first or produce secondary particles. In the latter, radioisotopes are distributed on the surfaces of materials, usually with a small skin depth.

All decay data in this section were found using Ref [58], and will not be cited individually.

2.3.1 The SNOLAB test facilities

The iZIP and HV detectors are currently operated at CUTE (Cryogenic Underground TEst facility), located 2km underground at SNOLAB. Cooling at CUTE is provided by a dilution refrigerator specially designed to minimize vibration transmission to the detectors. The dilution refrigerator and detector stacks are contained in a thermally-shielded cryostat, surrounded by copper, lead, polyethylene, and a 3.7 m diameter water tank that provides extensive shielding against gamma and neutron radiation (Fig 2.4). Along with efforts to minimize internal radiation, this pushes the expected background rate down to a few events/keV/kg/day [21].

Both detectors will also be deployed at the main SuperCDMS SNOLAB experiment, currently under construction and projected to start dedicated data taking by 2023 [20]. Here, the detectors are arranged in four towers of six detectors each, contained in a further series of nested copper housings known as the “SNOBOX” (Fig 2.5). Surrounding the SNOBOX are several layers of shielding, chiefly made of lead, aluminum, polyethylene, and water, which work to shield external radiation as well as secondary particles produced in each layer [59].

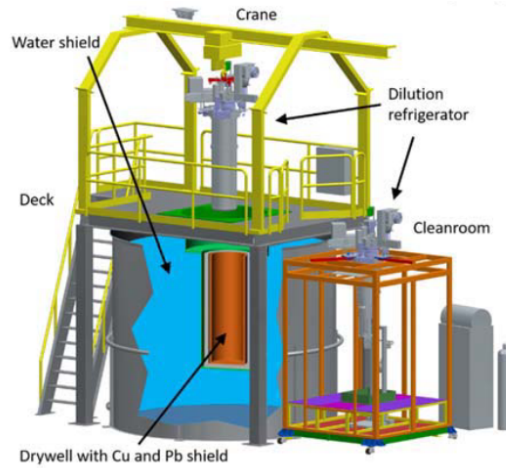


Figure 2.4: Illustration of the CUTE layout. During operation, the crane payload will be lowered into the drywell. Figure taken from Ref [21].

2.3.2 External Radiation

Radioisotopes are distributed throughout the test facilities, embedded in the cavern walls and in dust, which despite best efforts in maintaining a clean environment cannot be entirely removed. These are chiefly Th-232, U-238, K-40, which over the course of their respective decay chains produce a mix of alpha, beta, and gamma particles; a detailed treatment of these decays can be found in Refs [18, 59, 60]. These decays can produce significant NR (via alphas) and ER (via betas and gammas) event backgrounds in the detectors. Then, their decay products may in turn produce secondary particles: high-energy gammas can Compton scatter electrons that go on to produce a Compton ER background, and betas can undergo brehmsstrahlung, Cherenkov, and other types of processes to emit a further photon background.

In addition, the Th-232 and U-238 decay chains produce a neutron background via two processes. First is spontaneous fission (SF), where nuclei split into smaller nuclei and several free neutrons; this is a relatively rare process, with branching fractions of $\sim 10^{-7}$ for U-238 and $\sim 10^{-11}$ for Th-232, but nonetheless occurs enough to be a significant background. Second is the (α, n) process, where alpha particles created in the U-238 and Th-232 decay chains liberate neutrons in the

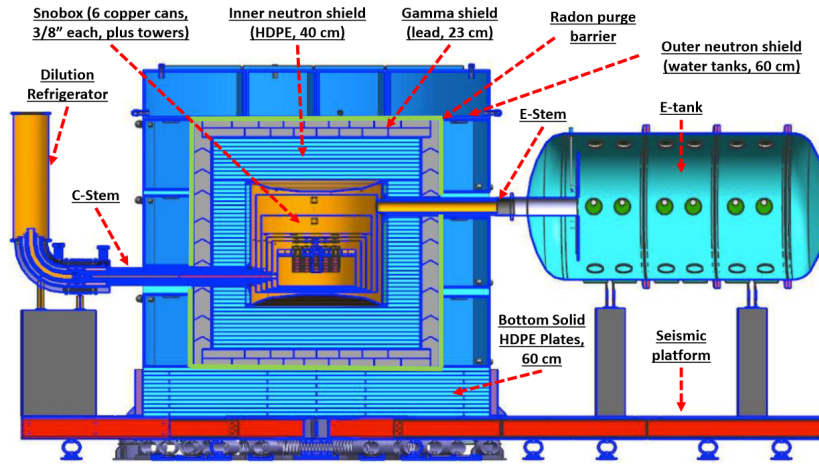


Figure 2.5: Schematic of the main SuperCDMS SNOLAB experiment, including the SNOBOX copper cans at the center. Figure taken from Ref [18].

material bulk. Simulations have shown that this can be a significant neutron source in common materials such as copper and polyethelene [18].

The shielding provided by CUTE and SNOBOX are highly effective at eliminating external sources of radiocontamination. Monte Carlo simulations of CUTE showed that external radiation can leak in from gaps in the lead shielding, which constitutes $\sim 40\%$ of the total radiogenic background [21]. Certain high-energy gammas and neutrons are also able to penetrate the shield layers directly, though simulations have shown that these backgrounds are likely subdominant [18].

2.3.3 Internal Bulk Radiation

Bulk radiation comes from two main sources: *cosmogenic* isotopes, which are activated by cosmic radiation and have relatively short half-lives (days \sim 100 years), and *primordial* isotopes, which were likely present since the formation of the Earth with very long half-lives (\sim Gyr). Additionally, there is *anthropogenic* radiation, or man-made sources, the most important of which is the Cs-137 produced from U-235 fission in nuclear reactors and weapons. Anthropogenic Cs-137 is expected to be subdominant at SuperCDMS SNOLAB, however [18].

A prominent source of bulk radiation comes from cosmogenic sources in the detector itself. These include [18, 60]:

- Tritium (H-3): Produced from interactions of cosmic-ray secondaries with Si or Ge nuclei, tritium is a beta-emitter with a relatively long half-life (for a cosmogenic source) of 12.3 years. This allows tritium to accumulate as the detector is prepared and stored aboveground. To mitigate contamination, proper aboveground storage is required, and a 365-day underground “cooldown” period is used in part to deplete the tritium before science data-taking.
- Germanium activation isotopes: Cosmic-ray secondaries also produce several other isotopes in germanium crystals with long enough half-lives to accumulate aboveground. As observed in the CoGeNT experiment [61], these are: Ge-68, Ga-58, Zn-65, As-73, Co-57, Fe-55, Mn-54, and V-49. All listed isotopes decay via electron capture, with very well-defined spectral peaks that can be vetoed efficiently given the detectors’ energy resolutions [59].
- Si-32: Interactions between cosmic-ray secondaries and atmospheric argon produce Si-32, which contaminates the terrestrial Si supply with a half life of 153 years. Since this is not produced in the crystal directly, the origin and purity of silicon must be considered before the crystal is grown. Assuming a similar contamination rate to that measured by the DAMIC Collaboration [62], this is expected to be the dominant source in Si detectors by $1 \sim 2$ orders of magnitude [18].

Next are sources found in the materials surrounding the detector; an accounting of the abundances in various materials is given in Table 2.1. These include the aforementioned U-238, Th-232, and K-40 that are also found throughout the lab environment, which emits a mixture of alphas, betas, gammas, neutrons, and secondary Compton, bremsstrahlung, and X-ray backgrounds. In addition, there are two other major sources:

- Co-60: Cosmic rays produce many radioisotopes in copper, with Co-60 as the dominant source by ~ 1 order of magnitude compared to Mn-45 in second place. It emits beta particles, which have a small chance of escaping

Material	U-238	Th-232	K-40
Copper	< 0.00018	0.00015	0.00031
Cirlex	14	4.5	< 5.3
Kapton	2.8	13	420
Kevlar	6	2	590
μ -metal	< 0.67	< 0.45	4
Polypropylene	0.098	0.095	0.8
Lead	0.66	0.5	7

Table 2.1: Activity rates (mBq/kg) of various isotopes in various important non-detector materials used at SuperCDMS SNOLAB, using recent assays compiled internally. Here, Cirlex is a proprietary polyimide film derived from Kapton; μ -metal refers to a nickle-iron alloy used for magnetic shielding. The total radiation and overall effect on the detector must take into account the relative masses of each material and their placement within the apparatus relative to the detector (e.g. Cirlex has a direct line of sight to the crystal, whereas Kapton does not). A full per-component list of radiocontamination can be found internally at Ref [13].

copper, and may additionally emit two high-energy gammas. Since Co-60 has a fairly short half-life of 5.3 days, it can be mitigated by minimizing aboveground storage and allowing a cooldown period underground before data collection [60].

- Bulk Pb-210: Deposited by Rn-222 decay naturally into lead, Pb-210 decays eventually into Pb-206 via a series of beta, gamma, and a single alpha emission. At CUTE, Pb-210 contributes $\sim 40\%$ to the total detector background rate, a similar level to external radiation. This can be improved by selecting for more depleted “ancient” lead and adding shielding between major lead layers and the detector.

2.3.4 Internal Surface Radiation

The main (and, practically, only [18]) source of surface radiation is the Rn-222 decay chain. Produced in the U-238 decay chain, Rn-222 has a half-life of 3.82 days, which allows it to diffuse into the atmosphere and onto surfaces, primarily those of copper. Further decay of Rn-222 deposits Pb-210 into the various surfaces

with a Gaussian depth distribution of order $\sim 10\text{nm}$ [60]; with a half-life of 22.2 years, Pb-210 can accumulate on surfaces in significant amounts.

The Pb-210 surface contamination can be more problematic than bulk Pb-210 as radon deposition occurs on surfaces very close to the detector (e.g. the inside surface of the copper housing and on the detector substrate itself). On the other hand, when the surface does not have a clear line-of-sight to the detector, its background contribution is minimal as Pb-210 decay products generally do not penetrate materials well.

The Pb-210 decay chain primarily consists of four isotopes: Pb-210, Bi-210, Po-210, and the stable Pb-206. Beta and gamma decays from Pb-210 and Bi-210 produce a near-surface ER background, which can be vetoed by the surface discrimination of iZIPs but are more challenging to handle in HV detectors. The alpha particles produced in the Po-210 decay are very energetic and produce NRs that fall outside of the DM signal region; the Po-210 daughter Pb-206 can recoil with sufficient energy to register as a DM-like NR event, but it can be mostly rejected with a coincidence veto as its sister alpha particle is usually found in an adjacent detector [18]. Given the extensive work done at SuperCDMS in assessing and mitigating these sources, the radon deposition background is mostly accounted for, but as we will see in Section 5, secondary optical photon production by radon decay products may introduce a new background at low energies.

2.3.5 Cosmic Muons

Thus far, we have assumed that cosmogenic activation occurs aboveground, producing relatively long-lived isotopes that persist once components are brought underground. However, while the 2 km of rock overburden at SNOLAB eliminates the vast majority of cosmic rays, a small fraction of muons remain that can penetrate detector shielding. These muons can, in turn, produce secondary particles or induce recoil events in the detectors directly, though the latter is rare enough that the SNOLAB detectors do not have muon vetos. Detailed angular and energy distributions of these muons can be found for SNOLAB in Ref [63].

Chapter 3

Low-Energy Backgrounds in Dark Matter Experiments

Optical-scale Cherenkov and transition radiation have not historically been relevant backgrounds to dark matter experiments. Their energies and intensities are assumed to be very low, and generally only produce electron recoil events, whereas DM particles were assumed to cause neutron recoils.

However, recent experiments probing sub-GeV dark matter have detected unexplained excesses of events at low energies. Broadly, experiments sensitive to single-electron events have found such excesses at $\lesssim 100$ eV; these include, but are not limited to, XENON10/100/1T [64], LUX [65], Darkside-50 [66], CRESST-III [67], vCLEUS [68], EDELWEISS [69, 70], SuperCDMS HVeV [54] and CPD [71], DAMIC [72], and SENSEI [73].

The new backgrounds found in these experiments at times differ greatly and at other times show remarkable consistency. There does not appear to be a definitive consensus on what any of the backgrounds are, nor have they been shown to have a common origin. What they do share, however, is an energy range relevant to Cherenkov and transition radiation, which may contribute significantly to the excesses found in some of these experiments. In this section, we will give a brief summary of the low-energy backgrounds detected so far and some plausible hypotheses of their origin.

3.1 Low-Energy Backgrounds in Low-Threshold Detectors

Table 3.1 presents a quantitative summary of the low-energy backgrounds found in each mentioned experiment, grouped broadly by readout type. Where possible, upper and lower bounds are set on the excess rate based on charge carrier production: the lower bound counts the number of $n_e \geq 2$ electron events, whereas the upper bound includes all single-electron events as well. Where charge data is not available, a lower bound is given as the total number of events above threshold.

The variation in thresholds and resolutions suggests a range of different backgrounds covering $\lesssim 1$ eV to $\gtrsim 100$ eV. At the high end, EDELWEISS-Surf identified an excess rising sharply with decreasing energy below 500 eV [70]. Detectors with high thresholds may also miss lower-energy events completely, although the rates observed thus far do not appear to be well-correlated with the energy threshold.

Fig 3.1 plots the excess rates against operating depth, which shows no obvious correlation. Most strikingly, the measured excess rates of the charge-readout detectors are very similar, despite being operated at different depths and with different target materials. Also somewhat self-consistent are the excess rates of the noble fluid detectors, though they were measured at approximately the same depth.

Notably, the rates observed by different readout types do not tend to agree with each other: measurements from the noble fluid detectors are orders of magnitude lower than the charge-readout detector rates. Immediately, this suggests that the low-energy backgrounds are likely caused by detector-specific effects. The hypotheses put forward thus far have broadly followed the same assumption.

Much variation exists even within each detector category, however, and the numbers alone do not provide a full picture of the breadth of experiments in which these backgrounds are found. In the following section, we will provide an overview of the detector types that have observed the low-energy background, as well as detector-specific hypotheses put forward to account for these backgrounds.

3.1.1 A Qualitative Description of Low-Threshold Detectors

- **Noble fluid detectors** (e.g. XENON10/100/1T, DarkSide-50, LUX):

Type	Experiment	Target	Resolution	Threshold	Rate (Hz/kg)
Charge readout	EDELWEISS [69]	Ge	$1.6 e^-$	0.5 eVee ($\sim 1e^-$)	[20,100]
	SENSEI [73]	Si	$\sim 0.2e^-$	1.2 eVee ($< 1e^-$)	[6,400]
	CDMS HVeV [54]	Si	$0.1 e^-$	1.2 eVee ($< 1e^-$)	[10,2000]
	DAMIC [72]	Si	$1.6 e^-$	1.2 eVee ($\sim 1e^-$)	$[1 \times 10^{-3}, 7]$
Calorimeter	EDELWEISS [70]	Ge	18 eV	60 eV	> 2
	CRESST-III [67]	CaWO ₄	4.6 eV	30 eV	$> 3 \times 10^{-3}$
	ν CLEUS [68]	Al ₂ O ₃	3.8 eV	20 eV	> 30
Noble fluid	XENON10 [64]	Xe	6.7 PE	12.1 eVee (~ 14 PE)	$[0.5, 3] \times 10^{-4}$
	XENON100 [64]	Xe	6.2 PE	~ 70 eVee (~ 80 PE)	$> 2, 2 \times 10^{-5}$
	XENON1T [74]	Xe	< 10 PE	~ 140 eVee (~ 90 PE)	$> 1.7 \times 10^{-6}$
	Darkside50 [66]	Ar	~ 15 PE	50 eVee	$> 6 \times 10^{-4}$

Table 3.1: Low-energy excesses observed at various experiments with single-electron resolutions. Upper and lower bounds are integrated over $n \geq 1$ and $n \geq 2$ electron event rates, respectively; where single-electron rates are unavailable, a lower limit of event rate above threshold is given. Top section corresponds to charge-sensitive calorimeters and CCDs, middle section to interaction-independent calorimeters, and bottom section to noble fluid detectors. Table originally compiled by Kurinsky et al. in Ref [1].

In two-phase noble fluid detectors, incoming particles scatter off of either electrons or nuclei in the noble liquid, which first produces a prompt emission of light known as the primary scintillation (S1). Ionized electrons may then be accelerated by an electric field into the gaseous region, where they interact with the noble gas to produce a second “proportional” scintillation (S2) [75]. The S2 process amplifies energy deposition, and “S2-only” searches are able to decrease energy thresholds down to levels without an observable S1 signal. XENON10 in particular has a threshold below the average energy required to produce an electron in xenon, and is therefore sensitive to single-electron events [64].

Accordingly, excesses down to single-charge events have been detected over the past decade and are comparatively well-studied. Observed correlations with the impurity densities and the time/position distributions suggest that the excesses may arise from known effects, including the photoionization of impurities, electron trapping and delayed rerelease, and the photoelectric effect on metal surfaces [65, 76, 77]. These hypothesized processes are gen-

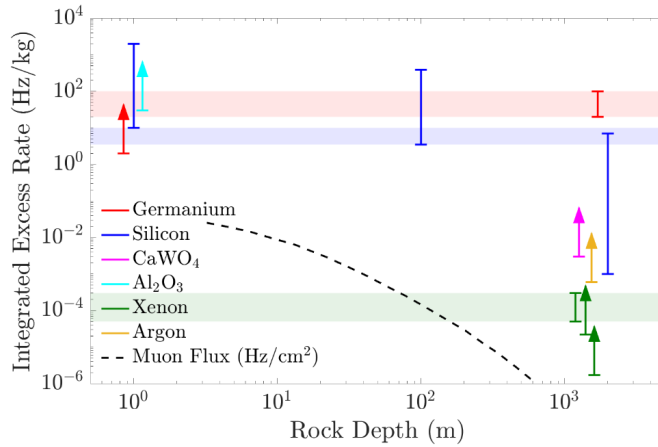


Figure 3.1: Excess rates (Table 3.1) found in various experiments with shown target materials versus rock overburden. Shaded bands indicate regions approximately consistent with excess rates for Ge (red), Si (blue), and Xe (green). Muon flux is shown in dashed black for reference of a depth-dependent effect. Figure taken from Kurinsky et al. in Ref [1].

erally responsible for single-electron events, though due to pileup they may obscure genuine multiple-electron events [65, 74].

While these hypotheses are well-motivated, they require more study to be properly understood and mitigated, and may in fact be consistent with a genuine dark matter signal [64].

- **Cryogenic calorimeter detectors** (e.g. CRESST-III, vCLEUS, EDELWEISS):

In cryogenic calorimeters, the target medium is a solid-state crystal brought to very low temperatures to reduce thermal noise and exploit superconductivity in transition-edge sensors (Section 2.1). Incoming particles deposit energy as phonons, which can be used to determine the energy deposition independent of the type of interaction; nuclear and electron recoils cannot be differentiated by phonons alone, though additional features such as light scintillation may be used for discrimination [67]. Due to the nature of cryogenic calorimeters, the single-electron event rate cannot be determined, so the rate of events above threshold is given instead as a lower limit [1].

The observed excess varies greatly between different experiments in this category, but usually presents as an event rate rising with decreasing energy, in contrast to known backgrounds that are approximately flat in the same energy range [1]. In CRESST-III, this background has been partly attributed to crystal cracking [78]. But, given the drastically different excess rates observed between CRESST-III and vCLEUS, crystal cracking alone is not an adequate explanation.

- **Cryogenic electron recoil searches** (e.g. SuperCDMS HVeV, EDELWEISS):

As an extension to cryogenic calorimeters, the Neganov-Trofimov-Luke (NTL) effect can be exploited by applying a strong bias voltage across the detector, which amplifies charge signals from electron recoils into larger phonon signals to achieve sub-eV resolutions (Section 2.1).

The background spectrum can be separated into n -electron bins, where the excess rate peaks with a large abundance of single-electron events and drops sharply with increasing n . In HVeV and EDELWEISS, many of the single-electron events can be attributed to the charge leakage found in high voltage detectors [54, 69]. A significant background remains even after these are removed, especially of multiple-electron events [4].

- **CCD electron recoil searches** (e.g. SENSEI, DAMIC):

In charge-coupled devices (CCDs), incoming particles produce electron-hole pairs in silicon, which are separated as the charge is drifted to a pixel array by an electric field applied along the depth of each pixel. There, charges are held until the entire device is read out, at which point the charges are transferred pixel by pixel to the CCD output [79].

Sensitivity in CCD detectors is primarily limited by readout noise, which is improved in Skipper-CCDs by performing many independent measurements of the pixel charges [80]. At SENSEI, Skipper-CCDs have lowered the energy threshold to sub-electron levels [73].

Both SENSEI and the standard CCD experiment DAMIC have detected low-energy backgrounds. The single-electron excess at SENSEI can be partly attributed to known spurious charge generation at readout in Skipper-CCDs, but a large single-electron rate remains after accounting for this effect [73].

Given the variety of well-motivated hypotheses specific to each detector, there are likely many distinct sources of low-energy backgrounds, where the dominant sources in each experiment is different at different energies. On the other hand, the similar excess rates found in the solid-state electron recoil searches, despite distinct technologies, suggests that at least some of the backgrounds are shared. In a recent

paper, Du et al. [4] proposed that the excesses in SENSEI, SuperCDMS HVeV, and EDELWEISS can be explained in part by Cherenkov radiation, transition radiation, and luminescence; the first two will be the primary focus of this thesis.

Finally, there is the possibility that the unexplained background is, in fact, dark matter. This possibility has been broadly ruled out as the observed excesses are inconsistent with elastic electron- and nuclear-recoil models. A recent paper by Kurinsky et al. [1] has attempted to reconcile low-energy observations with inelastic plasmon excitation from dark matter, though its conclusions are tentative and awaits further results from single-electron threshold experiments.

3.2 Low-Energy Backgrounds in SuperCDMS LAPD and HVeV-0VeV

In addition to the published HVeV Run 2 DM study, several other investigations of the low-energy backgrounds have been initiated at SuperCDMS. As of writing, the following unpublished results are preliminary and are meant to summarize observations of low-energy backgrounds broadly. More results are incoming in the near future, especially as CUTE operations resume after the COVID-19 pandemic.

- **LAPD/CPD** [71]: The LAPD or CPD (Section 2.2.3) was operated above-ground at SLAC, first at an energy resolution of ~ 3.8 eV (Run 44) and then at a decreased resolution of ~ 4.6 eV (Run 47) due to differences in calibration and environmental noise. It was operated again underground at CUTE, at energy resolutions of ~ 9.7 eV (Run 11) and ~ 5.3 eV (Run 14).

Low-energy backgrounds were observed in each. The SLAC R44 and CUTE R14 spectra share similarities below 100 eV, suggesting that the background is depth-independent. However, when performing likelihood fits to simple exponential backgrounds, the observed background spectra between runs do not appear to be consistent, even at the same test facility.

These discrepancies may be due to a poorly calibrated energy scale, as only a rough calibration was applied. CUTE Run 11 was also known to have infrared leaks, which inserted extra IR events and were fixed in CUTE Run 14. More data with better energy calibration in the future will allow us to

better compare these backgrounds between runs.

- **HVeV/0VeV** [81]: A preliminary analysis was performed with the HVeV detector, operated at three bias voltages of 100V, 60V, and 0V (AKA 0VeV) to compare the low-energy background measured under different conditions. A threshold of 9.1 eV and resolution of 2.5 eV were achieved in the 0V analysis, but due to the lack of NTL amplification its threshold could not be lowered to single-electron levels. Low-energy excesses proportional to the applied voltage are present at energies below 100 eV, where once adjusted for voltage, the 100V, 60V, and 0V backgrounds are mutually consistent.

Dominant in the low-energy region are burst events – groups of closely-packed pulses with non-Poissonian time distribution that precludes DM models. In HV data, burst events present as single-electron-scale secondary pulses following the main triggered pulse in the event trace. These may also be present in the 0V data as events with anomalously long decay times, though the exact relationship between the two phenomena is uncertain. Since burst events are incompatible with DM models, they were removed in the DM-search data (Table 3.1), but are included in this analysis.

The origin of burst events is as yet unknown, and even when burst events are removed, a significant portion of the excess remains as single-pulse events. One possible explanation is luminescence in SiO₂ layers, which can produce multiple photon peaks with a temperature-dependent time correlation. Much more study is required to verify this and other hypotheses.

Chapter 4

Radiation from Charges under Uniform Motion

Generally, we expect that radiation is emitted by charged particles undergoing acceleration. There exists, however, a class of radiative processes that occur while a charged particle is moving more or less uniformly: while a free particle emitting radiation will naturally slow down by conservation of energy, one can imagine a particle held in place in the lab frame by some combination of fields, as the medium around it is moved at a constant velocity. In this case, Cherenkov radiation may be emitted if the relative velocity of the charge exceeds the speed of light in the material, and transition radiation may be emitted if there is a change in the refractive index of the material, even though no net acceleration of the charge occurs!

Such processes have been explained as the coherent radiation originating from polarization caused by charges moving in media [82]. In particular, Cherenkov radiation is often analogized to a sonic boom, where successive wavefronts constructively interfere. This understanding of Cherenkov radiation is somewhat problematized over short path lengths, where a significant amount of Cherenkov light is emitted even by particles slower than the medium speed of light. In fact, Cherenkov and transition radiation can be understood as the same physical process in different regimes, with a transitional “hybrid radiation” between the two. Hybrid radiation becomes especially significant in transparent materials, such as the semiconductor crystals and plastic components found in dark matter detectors, with divergences

that make straightforward numerical integration impossible. In this chapter, we will discuss the basics of Cherenkov and transition radiation, then examine the transitional regime of hybrid radiation in detail, with the aim to develop a generic way of understanding and handling hybrid radiation.

4.1 Cherenkov Radiation

First, we will look at Cherenkov radiation (CR) alone, in the infinite path length limit in which it is usually considered.

4.1.1 Complex Index of Refraction

Cherenkov radiation is dependent on the dielectric properties of the material, characterized by the complex index of refraction \tilde{n} :

$$\tilde{n} = n + ik \quad (4.1)$$

Here, the real part n affects the phase velocity of light in the material as $v_{ph} = c/n$. The complex part k , also known as the extinction or absorption constant, describes the exponential attenuation of light in the material.

In dispersive media, the index of refraction is dependent on the photon frequency. The real and complex parts can vary greatly over the optical range; Fig 4.6 plots n , k for silicon as an example. We can also define the relative permittivity ϵ , or the dielectric function, as the square of the complex index:

$$\epsilon(\omega) = (\tilde{n})^2 = n^2 + 2ink - k^2 \quad (4.2)$$

From now on we will simply use n to refer to the complex index of refraction as a whole, as the real part alone will be of little relevance.

4.1.2 Cherenkov Radiation over an Infinite Path

For a charged source moving at a constant velocity in an infinite homogeneous medium, CR is emitted at a frequency ω when the particle velocity exceeds the

Cherenkov threshold [83]:

$$\beta_{\text{CR}} = \frac{1}{\sqrt{\text{Re}[\varepsilon(\omega)]}} \quad (4.3)$$

Note that $\text{Re}[\varepsilon(\omega)] = n^2 - k^2$ includes both the real and imaginary parts of the complex index of refraction. Since $\beta < 1$, CR is only physically possible when $n^2 - k^2 > 1$; as such, CR is prohibited in very absorptive media even if phase velocities are low.

Next, the angular distribution of Cherenkov radiation is strongly peaked in a cone defined by the *Cherenkov angle* $\theta_{\text{CR}}(\omega)$, where [84]:

$$\cos \theta_{\text{CR}}(\omega) = \frac{\sqrt{\text{Re}[\varepsilon(\omega)]}}{\beta|\varepsilon(\omega)|} \quad (4.4)$$

In the ideal case of uniform motion over an infinite path, CR is emitted at a single discrete angle θ_{CR} . This approximation is useful when the particle path length is long compared to the Cherenkov photon wavelength ($\ell \gg \lambda_{\text{CR}}$), which is broadly true whenever Cherenkov radiation is experimentally relevant. A slightly more nuanced view will be presented in Section 4.3.3.

Since $\varepsilon(\omega)$ is frequency-dependent, a particle in a dispersive medium will radiate over a range of frequencies and angles even in the ideal case. The frequency distribution of the number of photons emitted per unit path length is given by the Frank-Tamm formula [12]:

$$\frac{d^2 N_{\text{CR}}}{d\omega dl} = \frac{\alpha z^2}{\hbar c} \sin^2(\theta_{\text{CR}}) \quad (4.5)$$

where α is the fine structure constant and z is the particle charge number.

The Frank-Tamm formula is derived using classical electrodynamics only; quantum corrections may be important when photon frequencies are very low or when CR occurs over a very short length or time period (i.e. $\omega t < 1$) [85]. Generally, the relevant detector components are $\gtrsim 1$ mm in their shortest dimension, which takes $t \gtrsim 3 \times 10^{-12}$ s for a photon to traverse; for a 1 eV photon, we get $\omega t \gtrsim 1000$, so quantum corrections are likely very small. Other detector components (e.g. wires) may be thinner, but in turn have much smaller surface areas and therefore constitute

a very small proportion of the total Cherenkov emission.

4.2 Transition Radiation

Transition radiation (TR) is emitted when a charged source encounters inhomogeneities in the medium, either between different materials or within a material that has spatially-varying properties; in our case, only the former is relevant, and we will only consider discrete boundaries between materials with uniform indices of refraction.

4.2.1 TR at Normal Incidence

The simplest case is of a particle traversing two semi-infinite homogeneous media at normal incidence and constant velocity. TR is emitted both forwards (into the second medium) and backwards (into the first medium). The forward radiation has the differential emission rate [86]:

$$\begin{aligned} \frac{d^2 N_{\text{TR}}}{d\omega d\Omega} &= \frac{4z^2 \alpha \beta^2}{\pi \omega} \sqrt{|\epsilon_2|} \cos^2 \theta \sin^2 \theta |\epsilon_2 - \epsilon_1|^2 \\ &\times \left| \frac{1 - \beta^2 \epsilon_2 - \beta \sqrt{\epsilon_1 - \epsilon_2 \sin^2 \theta}}{(1 - \beta^2 \epsilon_2 \cos^2 \theta)(1 - \beta \sqrt{\epsilon_1 - \epsilon_2 \sin^2 \theta})(\epsilon_1 \cos \theta + \sqrt{\epsilon_1 \epsilon_2 - \epsilon_2^2 \sin^2 \theta})} \right|^2 \end{aligned} \quad (4.6)$$

where z is the charge number, α is the fine structure constant, and $\epsilon_{1,2} = n_{1,2}(\omega)^2$ are the relative complex permittivity of the media. For backward radiation, the signs on the β are flipped and ϵ_1 , ϵ_2 are exchanged. Note that this distribution is symmetric in ϕ . For normal incidence, transition radiation is always polarized parallel to the plane formed by the particle axis and the direction of radiation.

The TR angular distributions from a particle entering copper are plotted in Fig 4.1. At higher velocities the total intensity is greater both forwards and backwards, and the angular peak is shifted closer to the beam line.

The opposite scenario is shown in Fig 4.2, for an electron moving from copper to vacuum. This appears to be quite different from the $\text{Vac} \rightarrow \text{Cu}$ case, as the intensities are lower overall and the angular distributions are less strongly peaked.

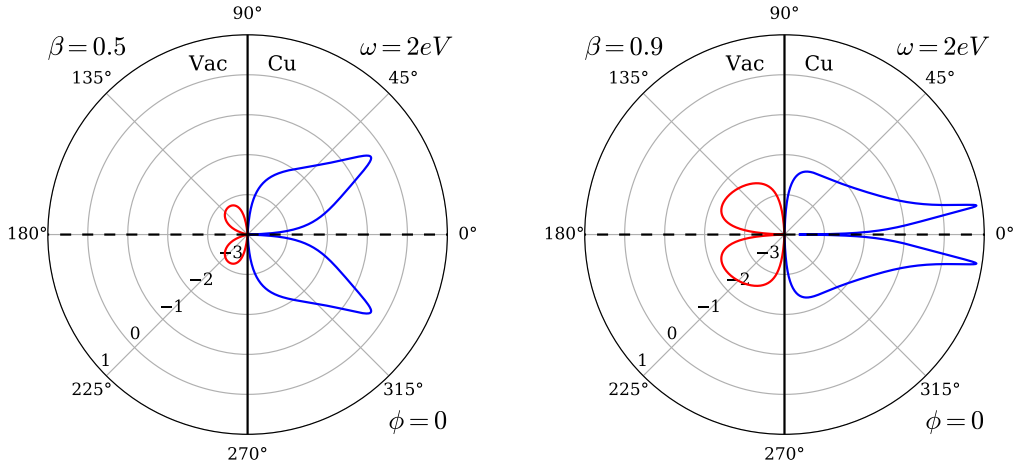


Figure 4.1: TR θ distributions (Eq 4.6) of 2 eV photons emitted from an electron traveling from vacuum to copper, at $\beta = 0.5$ (left) and 0.9 (right). Radial axis is in \log_{10} scale, with units $[\text{eV}^{-1}]$. Backward radiation into vacuum is shown in red, and forward radiation into copper is shown in blue. Choice of ϕ is arbitrary as the distribution is symmetric at normal incidence.

Most similar in magnitude and shape are the emissions into vacuum: compare the backward radiation in Fig 4.1 and forward in Fig 4.2. These will be particularly important as most detector components are opaque to optical photons, so photons emitted into vacuum are much more likely to hit the detector crystal than those emitted into materials.

The emission rates into vacuum are plotted in Fig 4.3. Forward radiation is often— but not always— more powerful than backward radiation, particularly at higher frequencies and particle velocities. On the other hand, the total TR rate is higher for both forward and backward radiation at low frequencies. This inherent imbalance in emission rates between forward and backward radiation will become especially relevant considering that the electron and muon backgrounds are not uniformly distributed or isotropic, and will produce forward and backward radiation at different rates.

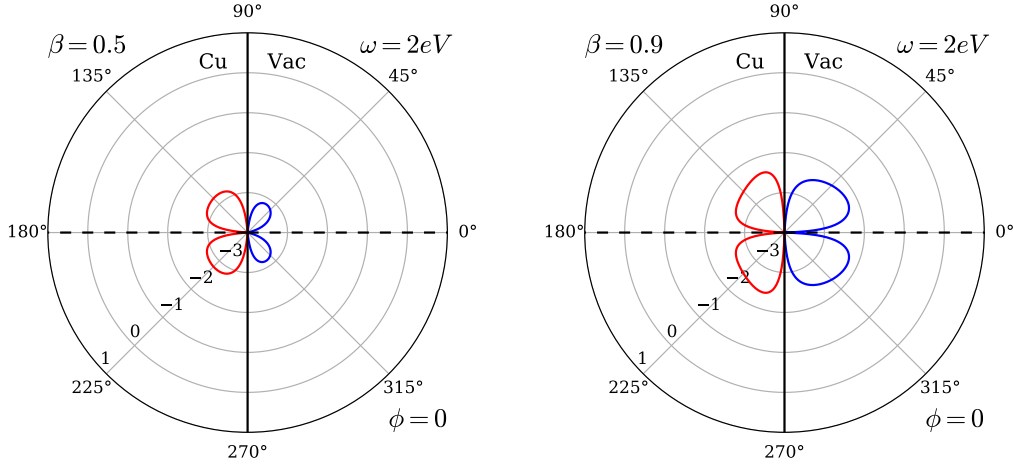


Figure 4.2: TR θ distributions (Eq 4.6) of 2 eV photons from an electron traveling from copper to vacuum, at $\beta = 0.5$ (left) and 0.9 (right). Radial axis is in \log_{10} scale, with units $[\text{eV}^{-1}]$. Backward radiation into copper is shown in red, and forward radiation into vacuum is shown in blue. Choice of ϕ is arbitrary as the distribution is symmetric at normal incidence.

4.2.2 TR at Oblique Incidence

The TR emission rate for arbitrary angles of incidence ψ is given in Eqs 4.7 of Section 4.3. The full implications and edge cases of this formula will be discussed in that section. Here, we will look at the simplest case of oblique TR below the Cherenkov threshold.

First, note that the emission rate at oblique incidence is split into two parts for two polarizations. Normal TR is polarized parallel to the incidence plane, but with increasing angles of incidence the perpendicular contribution increases as well [86]. In this thesis we will usually consider both polarizations together, as polarization is relatively unimportant for the materials used in dark matter detectors. Polarization will be accounted for in the simulation, however.

Fig 4.4 shows angular distributions for transition radiation at 45° incidence. Forward radiation into vacuum has a familiar form of two “lobes” around the beam axis (actually, a cross-sectional view of a 3D ring). The backward radiation into vacuum shows a similar distribution but reflected across the boundary normal.

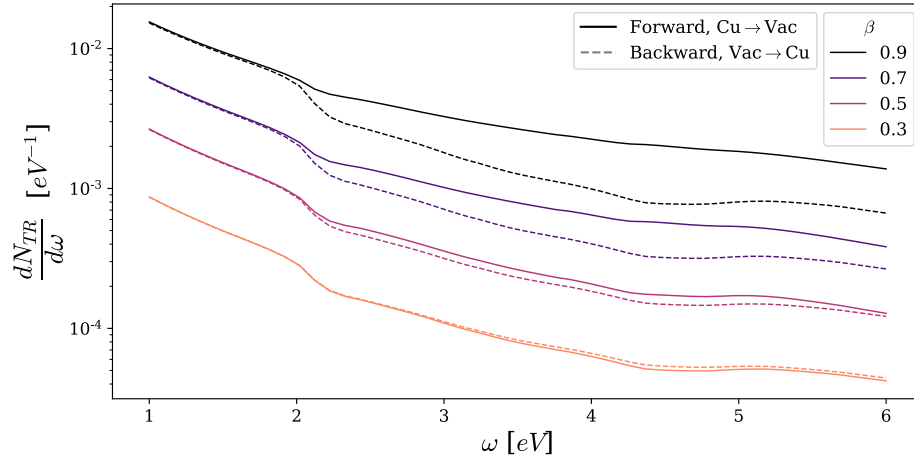


Figure 4.3: TR frequency spectra of an electron traversing a copper-vacuum boundary, emitting forwards into vacuum (solid) and backwards into vacuum (dashed) for several β .

4.3 Hybrid Cherenkov-Transition Radiation

For particle velocities near or above the Cherenkov thresholds of either media, the TR emission rate is modified significantly as it blends into Cherenkov radiation [87, 88]; in this regime the angular distribution shows strong peaks at the Cherenkov angles (Eq 4.4) in addition to the TR peaks near the beam axis.

This combination of TR, CR, and various interference effects between the two is known variably as *hybrid radiation* [88] or *Cherenkov-transition radiation* [89] by different authors. Here we will use the term hybrid radiation (HR) for brevity.

The HR emission rate is typically stated as separate formulas for parallel and

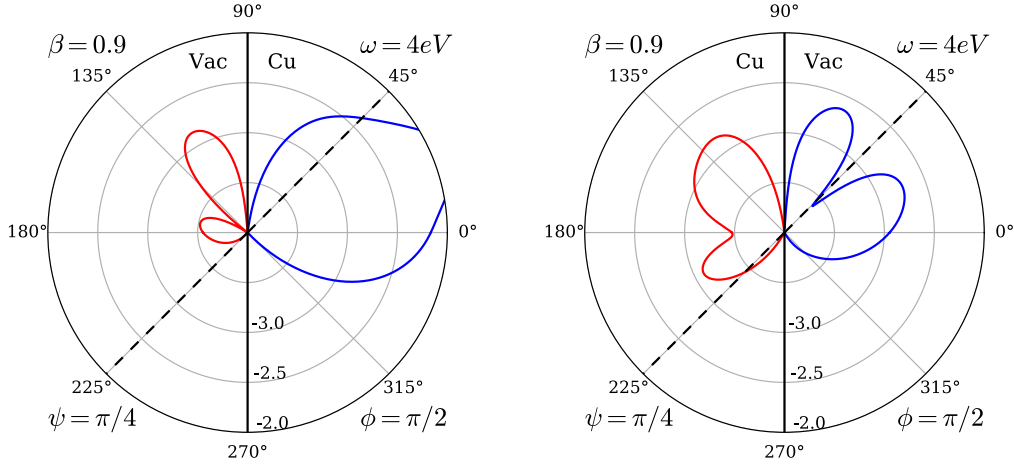


Figure 4.4: TR θ distributions (Eq 4.7) for an electron traveling from vacuum to copper (left) and copper to vacuum (right), at angle of incidence $\psi = \pi/4$, $\beta = 0.9$, and $\omega = 4 \text{ eV}$. Radial axis is in \log_{10} scale, with units $[\text{eV}^{-1}]$. At 4 eV in Copper, $\beta_{\text{CR}} > 1$ and Cherenkov radiation is prohibited for all velocities.

perpendicular polarization [86]:

$$\begin{aligned}
 \frac{d^2 N_{HR}^{\parallel}}{d\omega d\Omega} &= \frac{4\alpha\beta_z^2 \cos^2 \theta_z}{\pi\omega \sin^2 \theta_z} \times \left| \frac{(\epsilon_2 - \epsilon_1)(\epsilon_2)^{3/4}}{\epsilon_2 \sqrt{\epsilon_1 - \epsilon_2 \sin^2 \theta_z} + \epsilon_1 n_2 \cos \theta_z} \right|^2 \\
 &\times \left| \frac{\sin^2 \theta_z \left(1 - \beta_y n_2 \cos \theta_y - \beta_z^2 \epsilon_2 - \beta_z \sqrt{\epsilon_1 - \epsilon_2 \sin^2 \theta_z} \right) + \beta_z \left(\beta_y n_2 \cos \theta_y \right) \left(\sqrt{\epsilon_1 - \epsilon_2 \sin^2 \theta_z} \right)}{\left[(1 - \beta_y n_2 \cos \theta_y)^2 - \beta_z^2 \epsilon_2 \cos^2 \theta_z \right]} \right|^2, \\
 &\times \left| 1 - \beta_y n_2 \cos \theta_y - \beta_z \sqrt{\epsilon_1 - \epsilon_2 \sin^2 \theta_z} \right|
 \end{aligned}$$

$$\begin{aligned}
 \frac{d^2 N_{HR}^{\perp}}{d\omega d\Omega} &= \frac{4\alpha\beta_y^2 \beta_z^4 \cos^2 \theta_x \cos^2 \theta_z}{\pi\omega \sin^2 \theta_z} \times \left| \frac{(\epsilon_2 - \epsilon_1)(\epsilon_2)^{3/4}}{\sqrt{\epsilon_1 - \epsilon_2 \sin^2 \theta_z} + n_2 \cos \theta_z} \right|^2 \\
 &\times \frac{1}{\left| \left[(1 - \beta_y n_2 \cos \theta_y)^2 - \beta_z^2 \epsilon_2 \cos^2 \theta_z \right] \right|^2} \\
 &\times \left| 1 - \beta_y n_2 \cos \theta_y - \beta_z \sqrt{\epsilon_1 - \epsilon_2 \sin^2 \theta_z} \right|
 \end{aligned} \tag{4.7}$$

where $\cos \theta_x = -\sin \theta \cos \phi$, $\cos \theta_y = \sin \theta \sin \phi$, $\theta_z = \theta$;
 $\beta_y = \beta \sin \psi$, $\beta_z = \beta \cos \psi$ are the particle β components for incident angle ψ ;
and $\epsilon_{1,2} = n_{1,2}^2$ are the complex relative permittivities of either material.

As discussed in the previous section, Eq 4.7 is not unique to HR, but is in fact the generalized formula for TR at arbitrary angles of incidence (in fact, the Cherenkov peaks are present even in the normal incidence formula Eq 4.6). This suggests that transition and Cherenkov radiation are not distinct phenomenon, nor is hybrid radiation a simple interference between the two; rather, TR and CR can be viewed as the same phenomenon under different conditions, and HR is the transitional form.

It will be useful, however, to treat HR as being composed of separate TR and CR components. To minimize confusion, “TR” and “CR” will now refer to the TR-like and CR-like contributions to the overall HR emission rate. We will instead use “pure TR” to mean sub-threshold TR and “pure CR” to mean to bulk CR in homogeneous media.

4.3.1 Divergence at the Cherenkov Angle

Some angular distributions for forward HR into silicon are plotted in Fig 4.5; per Fig 4.6, the chosen β are below/above threshold for all plotted ω . At sub-threshold velocities, pure TR occurs with a characteristic peak at low angles. Near or above the threshold, a separate peak forms at the Cherenkov angle θ_{CR} (here, between 70° to 80°).

For a perfectly transparent material, the CR-like peak is in fact divergent, as the $[(1 - \beta_y n_2 \cos \theta_y)^2 - \beta_z^2 \epsilon_2 \cos^2 \theta_z]$ denominator term in Eq 4.7 crosses zero. This a consequence of assumptions made in the derivation of Eq 4.7, which integrates the HR field energy over the entire (*infinite!*) particle trajectory [90].

The HR derivation assumes that both media are semi-infinite, and follows the same steps as the pure CR derivation by considering the field equations of either media in isolation. Subsequently, the unique properties of TR are derived as the two sets of field equations are compared at the boundary, after which the field energy is integrated over the entire particle trajectory. Importantly, the Cherenkov character of the fields in either media remains, and is in fact necessary to the overall

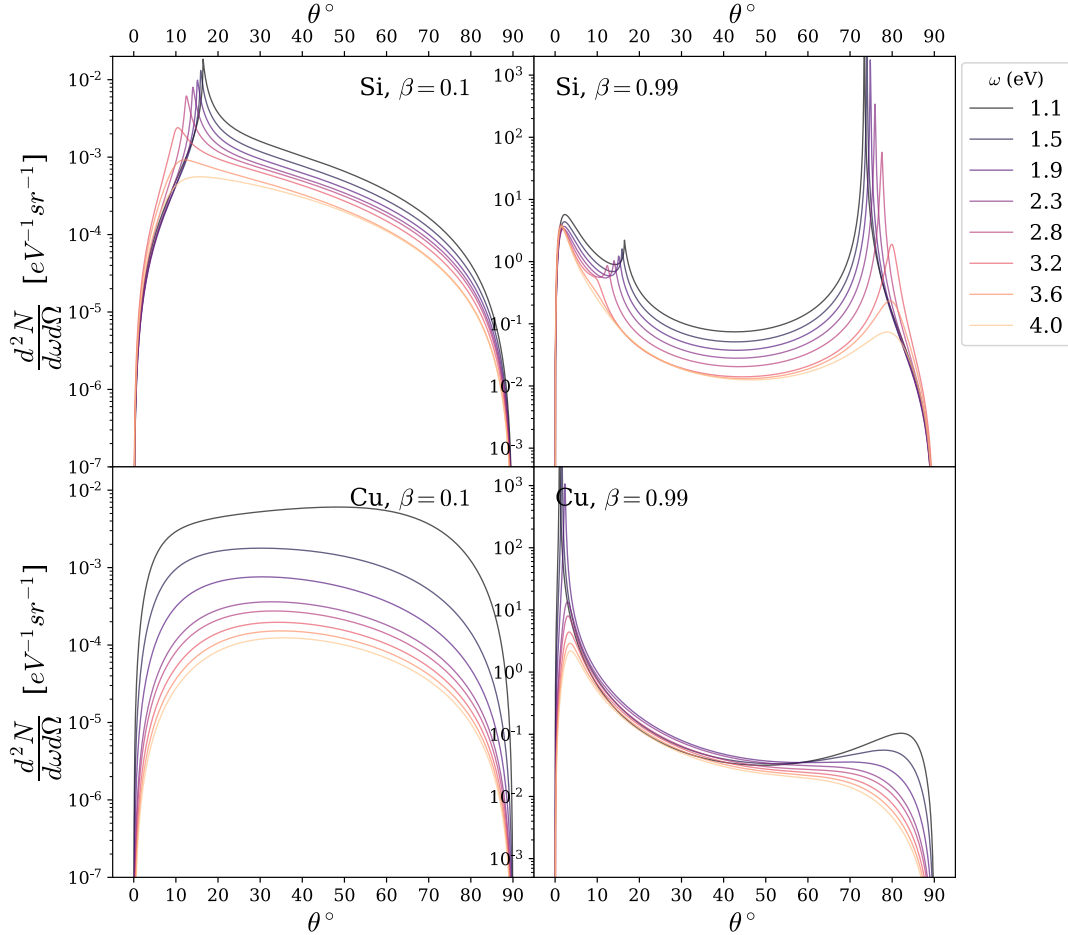


Figure 4.5: HR distributions (Eq 4.7) for an electron of $\beta = 0.1$ (left) or $\beta = 0.99$ (right) and listed photon frequencies ω , emitted forward from vacuum into silicon (top) or copper (bottom at normal incidence. At higher velocities, HR into silicon shows a strong CR-like peak, whereas HR into copper shows a strong TR-like peak.

derivation. For above-threshold velocities, this produces infinitely many CR-like photons over the infinitely long particle trajectory. A more detailed account of this derivation can be found in Ref [90].

In real materials, the CR peak is finite, as a nonzero absorption constant k (or the imaginary component of refractive index) prevents the $[(1 - \beta_y n_2 \cos \theta_y)^2 -$

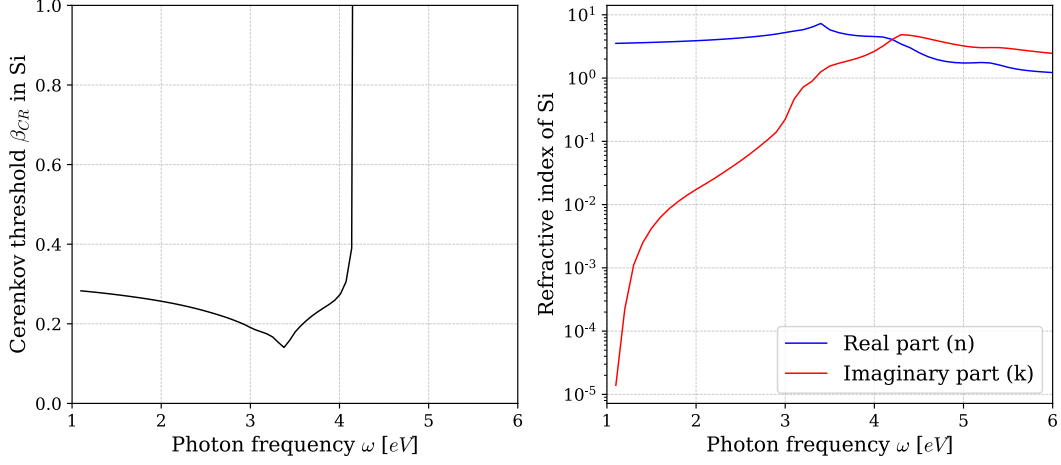


Figure 4.6: (Left) The Cherenkov threshold (Eq 4.3) in silicon. (Right) The complex refractive index r of silicon over ω .

$\beta_z^2 \epsilon_2 \cos^2 \theta_z]$ denominator term in Eq 4.7 from reaching zero. Fig 4.5 shows that the CR peak intensity becomes comparable to TR intensity at $\omega \approx 3$ eV, which suggests that an absorption factor of $k \gtrsim 0.1$ is sufficient to suppress the CR peak such that the TR peak is dominant.

4.3.2 The HR Formation Length

Although transition radiation is often considered as a discrete boundary effect, as discussed previously its derivation involves an integration of field energies over the entire particle trajectory. However, the majority of TR occurs within a finite distance known as the formation length l_f . At normal incidence, this is [88]:

$$l_f(\omega, \theta) = \frac{\beta \lambda n}{2|1 - \beta n \cos(\theta)|} = \frac{hc\beta}{2\omega|1 - \beta n \cos(\theta)|} \quad (4.8)$$

where $\lambda = hc/n\omega$ is the photon wavelength within a medium, and θ is the angle measured from the boundary normal.

The specific choice of formation length is somewhat arbitrary, as HR formation does not have a definite endpoint. In fact, the formation length is defined differently by different authors, though they tend to share the order of magnitude [88]. Here, it

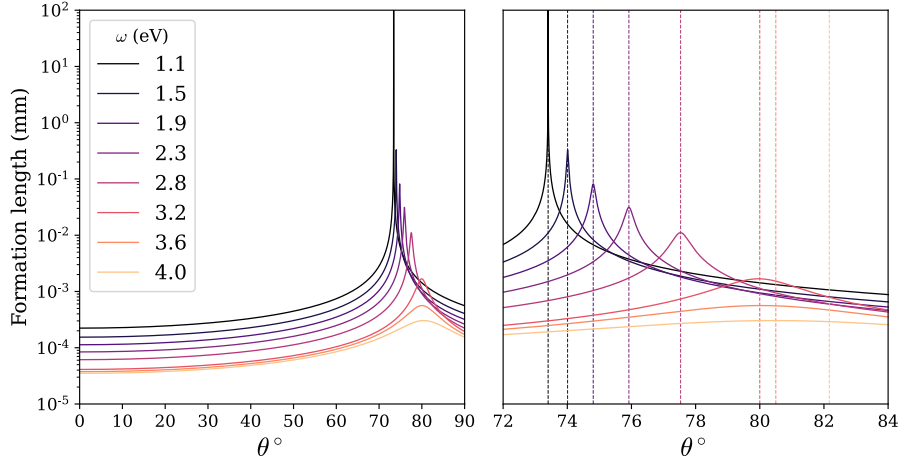


Figure 4.7: (Left) Formation lengths l_f (Eq 4.8) for an electron of $\beta = 0.99$ and listed photon frequencies ω , emitted forward from vacuum into silicon at normal incidence. (Right) The left plot zoomed in, with dotted lines that mark the Cherenkov angle θ_{CR} at each ω .

is defined as the length over which TR-like and CR-like components of HR move from constructive to destructive interference. Consequently, the formation length is angle-dependent; at the divergent peaks where $\theta = \theta_{CR}$, that is for parallel TR and CR, the formation length so defined is also infinite for a perfectly transparent medium.

Fig 4.7 plots l_f in silicon for $\beta = 0.99$ and a selection of ω . These are peaked towards the Cherenkov angles θ_{CR} particularly strongly at low energies, mirroring the behavior of the CR-like peaks in the HR distributions (Fig 4.5). This comparison suggests an interpretation of HR as *delocalized* TR, where the formation length grows long enough that CR becomes dominant.

This interpretation of HR also suggests that the CR-like peaks in Fig 4.5 are a consequence of divergences in formation length, and vice versa that the intensity can be constrained by the formation length. Dividing the HR emission by its maximum formation length yields an average *emission per unit length*, which we can

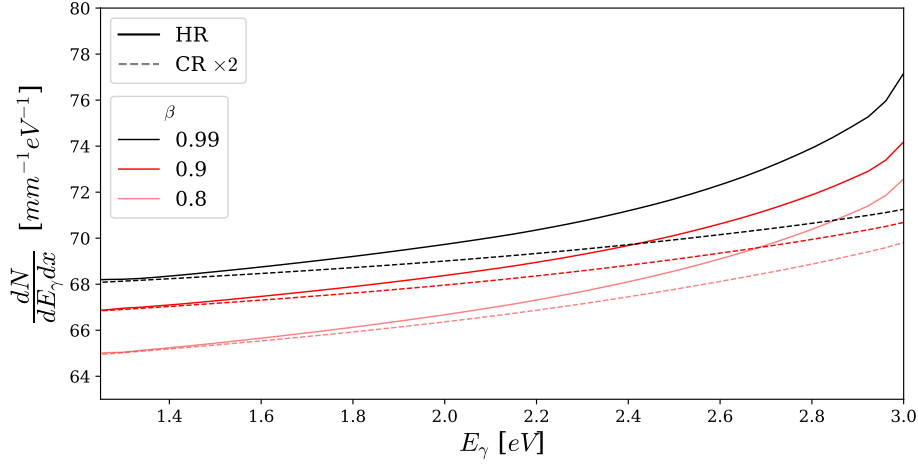


Figure 4.8: Comparison of HR intensity (Eq 4.9) and CR intensity at various β , emitted forward from vacuum into silicon at normal incidence. Here, CR intensity is multiplied by 2 to show similarities between CR and HR.

approximate as the length-differential emission rate:

$$\left\langle \frac{d^3 N_{HR}}{d\omega d\Omega dx}(\omega) \right\rangle = \frac{1}{l_f^*(\omega)} \frac{d^2 N_{HR}}{d\omega d\Omega}(\omega), \quad l_f^*(\omega) = l_f(\omega, \theta = \theta_{CR}),$$

$$\frac{d^3 N_{HR}}{d\omega d\Omega dx}(\omega) \approx \left\langle \frac{d^3 N_{HR}}{d\omega d\Omega dx}(\omega) \right\rangle \quad (4.9)$$

where l_f^* is the maximum formation length for a given frequency. By integrating over solid angle this rate can be directly compared to the bulk CR rate; Fig 4.8 shows that this is indeed finite and stable even at low energies. In fact, at low energies (i.e. where the absorption constant is especially low) the HR length-differential intensity appears to converge with $2 \times$ that of CR. Since the formation length is somewhat arbitrary, we can redefine the formation length to be $2 \times$ the definition given in Eq 4.8, so that CR and HR transition smoothly into each other.

4.3.3 HR and Finite Path CR

Cherenkov radiation is usually calculated with the Frank-Tamm formula (Eq 4.5), for a particle traveling at constant velocity through an infinite homogeneous medium. In this model, the particle emits a ring of radiation at a single $\theta_{\text{CR}}(n)$ for each $n(\omega) < 1/\beta$. This is an idealized picture, however, as particles in real settings will undergo acceleration, encounter inhomogeneous media, or traverse boundaries between media. Realistically, Cherenkov radiation occurs not at a discrete $\theta_{\text{CR}}(n)$ but as a peaked distribution over a range of angles; nor does Cherenkov radiation begin immediately at the threshold, but some degree of sub-threshold CR may occur [2].

When the CR wavelength λ is small compared to the path length ℓ of the particle, the CR distribution is strongly peaked and the infinite path length approximation is effectively correct. When $\lambda \sim \ell$, however, the *Tamm formula* (not to be confused with the standard *Frank-Tamm formula*) may be a useful approximation, which describes the radiation from a particle brought instantaneously from rest to a constant velocity, then brought back to rest instantaneously after traveling for a finite interval [2, 82]:

$$\frac{d^2 N_{\text{CR}}}{d\Omega d\lambda} = \frac{\alpha n(\lambda) \ell^2 \sin^2(\pi k)}{\lambda^3 (\pi k)^2} \sin^2 \theta, \quad k = \frac{n(\lambda) \ell}{2l_f(\theta)} \quad (4.10)$$

Where ℓ is the path length of the particle, λ is the CR wavelength, $n(\lambda)$ is the refractive index, and $l_f(\theta)$ is the HR formation length (Eq 4.8). This formula predicts a broad interference pattern (Fig 4.9); when k is an integer, it labels an interference maximum. For larger ℓ , the $\sin^2(\pi k)$ factor produces a denser pattern with a narrower and more prominent central peak, which recovers the familiar discrete Cherenkov peak as $\ell \rightarrow \infty$. The Tamm formula also predicts that the length-averaged CR intensity does not change with path length ℓ : since ℓ is included in k , the only dependence on ℓ is in the periodic factor $\sin^2(\pi k)$. Integrating this factor over ℓ should yield a linear dependence on ℓ for the total CR emission, which is in turn canceled out in the average CR emission per unit length.

The presence of l_f in Eq 4.10 suggests that HR and finite path CR are intimately related. Quantitative similarities between the two are discussed in Ref [2], which concludes that the Tamm formula predicts traits characteristic of transition radia-

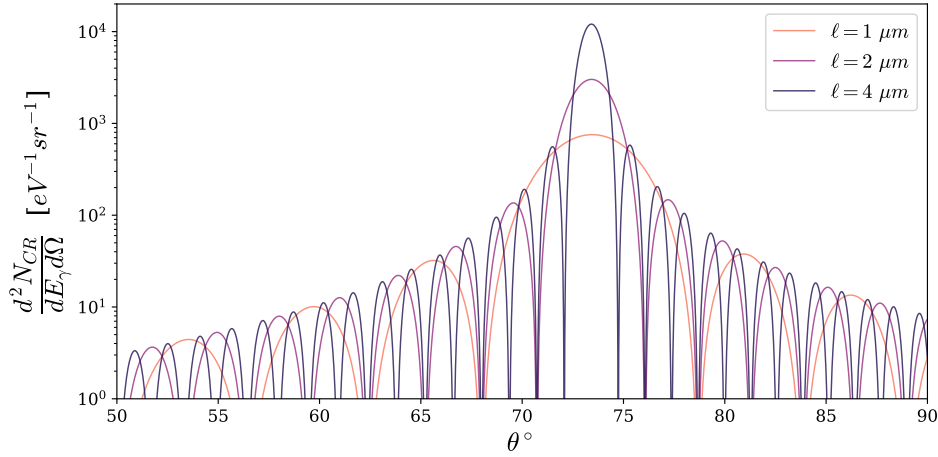


Figure 4.9: Finite path length CR calculated with the Tamm formula (Eq 4.10 for silicon, $\beta = 0.99$, $\omega = 1$ eV, and a variety of path lengths ℓ .

tion, even as it is derived for a homogeneous medium. Qualitatively, both HR and finite path CR can be modeled as a series of mutually interfering Bremsstrahlungs, which is discussed in Tamm’s original paper on finite path CR [82] and in further detail in Refs [91].

More importantly for us, the broad peak of the Tamm formula explains the broad CR-like peak of the HR distribution, which is not accounted for by the discrete emission angle of infinite path CR. At low energies, the absorption factor k is very small (Fig 4.6) and the maximum HR formation length is long – consequently, the CR-like peak is narrow, which then broadens with increasing energy and decreasing formation length.

Fig 4.8 shows that the length-averaged HR intensity is very nearly twice the infinite path CR intensity at low energies. The specific origin of this extra $2\times$ factor is unknown, but as previously stated (Section 4.3.2) the formation length is somewhat arbitrarily defined, and may well be off by a normalization factor. We will adjust for this using an ad hoc redefinition of the formation length:

$$l_f(\omega, \theta) = \frac{hc\beta}{\omega|1 - \beta n \cos(\theta)|} \quad (4.11)$$

which is simply $2\times$ the original expression given in Eq 4.8. Further investigations into the physicality of this definition may be necessary.

4.3.4 Suppression of HR from Scattering

Thus far, we have assumed that the incident particle travels the formation length in a straight line. For formation lengths shorter than the mean free path in the forward material ($l_f < \ell$) e.g. in metals, this is a valid approximation.

In silicon, however, l_f can range from $< 1 \mu\text{m}$ for pure TR to $\gtrsim 1\text{mm}$ at CR-like peaks (Fig 4.7). In the latter case, an electron will likely scatter before the entire formation length can be reached. If this happens, radiation at different points along the particle trajectory become incoherent, and the overall Cherenkov-like radiation would be abridged.

Assuming that $\lambda \ll \ell$, the Cherenkov-like radiation occurs over a finite but long enough path length that the standard Frank-Tamm formula (Eq 4.5) can be used, where CR occurs at an approximately constant emission rate per distance. This is likely untrue outside of the CR-like peaks, but formation lengths there are short enough that scattering would be very rare and we can assume that the TR-like part is always emitted in full.

Under this approximation, prior to scattering the particle emits Cherenkov-like HR at a constant emission rate per unit length $dN_{HR}/dl = N_{HR}/l_f$ prior to scattering. Per Fig 4.8, at relevant (i.e. low) energies the CR-like part of HR is very close to the pure CR when adjusted by a normalization factor present in the formation length. As such, after scattering we may simply switch from N_{HR}/l_f to the pure CR emission rate (Eq 4.5) with a minimal interruption in continuity.

Chapter 5

Estimates of Cherenkov and Transition Radiation in SuperCDMS Detectors

5.1 Transition Radiation in SuperCDMS SNOLAB

In this section we present analytical estimates of transition radiation from electron and muon backgrounds at SNOLAB. These estimates will consider TR photons emitted from the copper housing only, as it has by far the largest surface area out of all detector components. We will also simplify the geometry to two parallel copper and semiconductor plates, representing the housing and detector respectively.

Photons emitted from copper may reflect multiple times between the copper and detector, after which it may be absorbed and lost in copper. The effect of multiple reflections on the total detector hit rate can be estimated using the reflectance for either surface at normal incidence:

$$R(\omega) = \left| \frac{1 - \sqrt{\epsilon(\omega)}}{1 + \sqrt{\epsilon(\omega)}} \right|^2 \quad (5.1)$$

Whereas the transmission rate is $T(\omega) = 1 - R(\omega)$. For TR photons emitted from copper, the average fraction absorbed in silicon can be calculated with an infinite

series:

$$N_{\text{abs}} = T_{\text{Si}} \sum_{n=0}^{\infty} R_{\text{Si}}^n R_{\text{Cu}}^n N_{\text{TR}} = \frac{T_{\text{Si}}}{1 - R_{\text{Si}} R_{\text{Cu}}} N_{\text{TR}} \quad (5.2)$$

Note that this assumes that photons arrive at the detector crystal *first*, before bouncing back and forth between copper and silicon; we will label this scenario “Si-first.”

In reality, the copper housing surrounds the detector, and a photon emitted from copper is very likely to hit another copper surface before reaching the detector at all. This has a significant effect on the absorption rate in crystal as a large portion of photons may be absorbed in copper first. We can account for this scenario by applying an extra R_{Cu} factor to Eq 5.2, which we will label “Cu-first”. In fact, even more factors can be applied to account for consecutive reflections between copper, but we will omit them in this estimate as they merely compound the same effect.

5.1.1 TR from Radon Decay Background

The following section draws heavily from work done by Dr. Alan Robinson internally at the SuperCDMS Collaboration [3].

As discussed in Section 2.3, the Radon-222 decay chain deposits a number of radioactive isotopes into the surface of the copper housing. Of these, the most energetic beta emitter is Bi-210, with a mean energy of 389 keV ($\gamma \sim 1.761$). The TR spectrum (Eq 4.6) from these betas exiting copper is plotted in Fig 5.1, along with the absorbed spectrum after Si-first reflection (Eq 5.2). Also shown is the spectrum from Cu-first reflection, which suppresses detector hits at $\omega \gtrsim 2$ eV, skewing the TR spectrum even more towards lower energies; consecutive reflections from copper amplify this effect even more. At these energies we would expect, then, that TR primarily produces an excess of single electron-hole events.

An average of ~ 0.04 TR photons are produced per Bi-210 decay. After reflections this is reduced to ~ 0.03 photons absorbed in Si, and further reduced to $\lesssim 0.02$ when reflected from copper first. For a total Pb-210/Bi-210 contamination of 0.00957 mBq on the inner surface of the copper housing [13], this suggests an approximate absorption rate of ~ 10 photons/year for a single detector.

A beta particle exiting copper will likely hit the detector crystal, which produces a large ionization signal coincident with the TR photon that is easily iden-

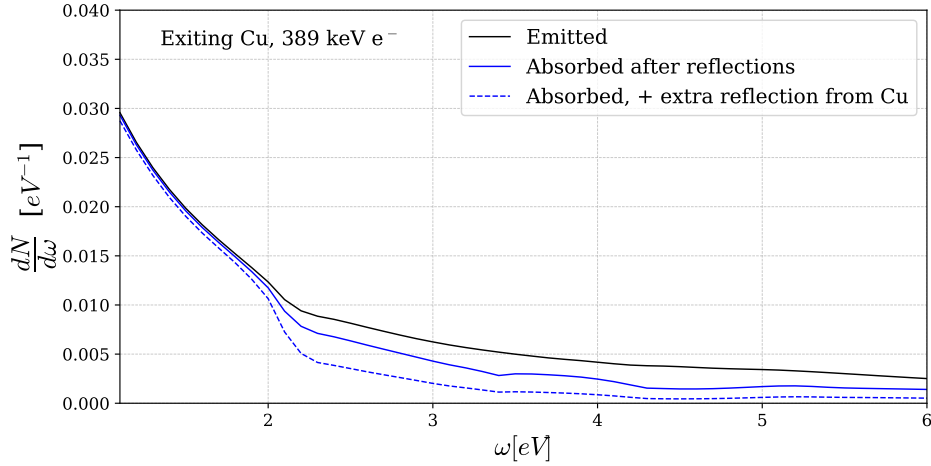


Figure 5.1: TR spectra for average Bi-210 decay (389 keV or $\beta = 0.823$) electrons entering copper from vacuum at normal incidence. The three lines are the emission spectrum in black, the absorption spectrum from Si-first reflection (Eq 5.2) in blue, and the absorption spectrum from Cu-first reflection in dashed blue.

tified and rejected. The detector housing also contains various other components and gaps, making it easier for a TR photon to miss the detector. As such, the actual absorption rate is likely to be much lower and will require a full simulation (Chapter 7) to calculate. As a rough estimate, gaps between the detector and housing are $\sim 10^{-1}$ times the detector diameter at the narrowest, so that a beta particle has on average $\sim 10\%$ chance of missing the detector. We therefore expect a TR contribution to the unexplained excess rate at ~ 1 photon/year.

5.1.2 TR from Beta Decays in Cirlex

As shown in Table 2.1, the two materials with the largest activity-mass density are Cirlex and Kevlar. Of these, Cirlex is located within the copper housing, with a straight line of sight to the detector crystal. Each detector is held in the copper housing by 12 Cirlex sensor clamps of 0.17 g each. The copper housing also contains 8 Cirlex detector interface boards (DIBs) of 0.21 g each. This gives a total of 3.72 g of Cirlex per detector, which is the main source of beta decays after the Rn-222 decay chain.

The dominant beta-emitting radioisotopes in Cirlex are U-238 at 14 mBq/kg and K-40 at < 5.3 mBq/kg. U-238 itself alpha decays into Th-234, which subsequently beta decays to Pa-234m at an average beta energy of 47.8 keV. Then, Pa-234m primarily (99.84%) beta decays into U-234 at an average beta energy of 810 keV, which remains relatively stable at a half-life of 2.5×10^5 years. In this estimate we will use the comparatively energetic Pa-234m decay.

Next, about 89.28% of K-40 decays into stable Ca-40 with an average beta energy of 500 keV. The rest decays to Ar-40 by electron capture, which may produce a subdominant Compton background that we will ignore. For about 3.72 g of Cirlex per detector, we get an approximate background of ~ 1600 betas per year at an average energy of ~ 810 keV from U-238, and $\lesssim 600$ betas per year at average energy of ~ 500 keV from K-40. Also present in the Cirlex is Th-232, whose daughter Ra-228 undergoes beta decay at 7.2 keV with a half-life of 5.75 years; due to its low energy and long half-life, we will neglect this decay in our total.

The Cirlex components are irregularly shaped, but are roughly flat, with a shared thickness of around 1.5 mm. The mean electron track length in Kapton, assumed to be close in composition to Cirlex, is 1.4 mm for 500 keV electrons and 2.6 mm for 810 keV electrons, rising to ~ 8 mm for 2 MeV electrons at the high end of the Pa-234m beta spectrum. Using trigonometry, the average fraction that escape Cirlex is $\sim 60\%$ for 500 keV electrons and $\sim 80\%$ for 810 keV electrons. Since most electrons will escape Cirlex, this may be a significant source of TR—the total radioactivity is higher compared to radon deposition, and TR may occur twice per decay as electrons leaving Cirlex may subsequently enter copper. Importantly, however, many electrons will likely have lost much of their energy by the time they reach the surface of the Cirlex. The overall effect of the electron stopping power in Cirlex is difficult to calculate analytically and will be deferred to the simulation.

Finally, Cirlex is fairly transparent at optical frequencies, so TR and HR emitted into Cirlex may then transmit out of Cirlex. In this case, both forward and backward HR must be taken into account, both for charges exiting Cirlex and for charges produced elsewhere entering Cirlex.

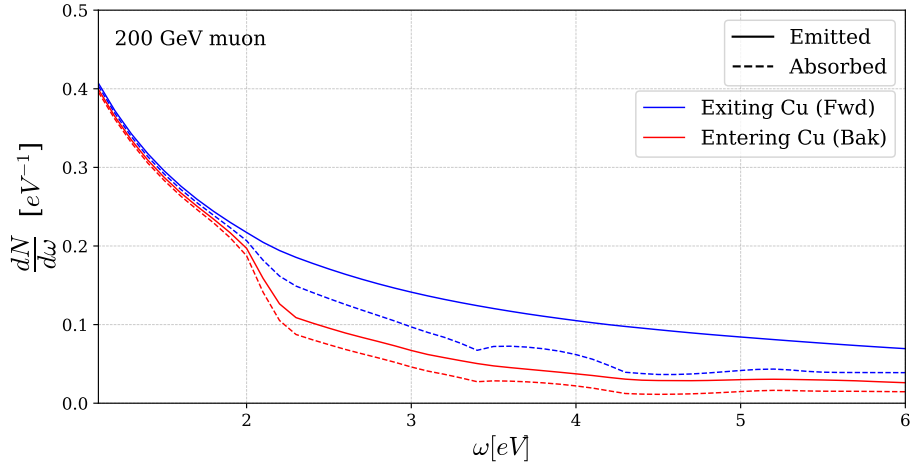


Figure 5.2: TR spectra for peak cosmic-ray muons (200 GeV) crossing a copper/vacuum interface at normal incidence. The emission spectra are shown in solid lines, and the absorption spectra are shown dashed (Eq 5.2).

5.1.3 TR from Muon Background

The rock overburden at SNOLAB is expected to remove the bulk of the cosmic-ray muon background, but a small fraction remains ($\sim 0.001/\text{cm}^2\text{-yr}$) and may generate TR on the interior of the copper housing. In particular, cosmic-ray muons are very energetic compared to betas, with a peak energy at around 200 GeV ($\gamma = 1.9 \times 10^3$) [63].

Once again, we consider the copper housing as the main source of TR events. The muon background is not isotropic; as an approximation we assume that all muons pass through the top and bottom lids at normal incidence, with no flux through the sides. Fig 5.2 plots the TR spectra for $E_\mu \approx 200$ GeV, along with the spectra after reflections; not shown are spectra after consecutive reflections from copper, which further suppress $\omega \gtrsim 2$ eV photons as in Fig 5.1.

Accounting for both forward and backward radiation, and summed between 1 and 6 eV, an average of ~ 1.2 TR photons are emitted per muon track, or ~ 1.0 absorbed. The detector lids share a radius of 5 cm, or around 78 cm^2 area, which intersects ~ 0.1 muons per year. Thus, an estimated ~ 0.1 TR photons are gener-

ated and absorbed per year from the muon background, before any cuts are applied. The TR background from muons is therefore likely subdominant compared to TR from Bi-210 decays.

5.1.4 Other TR Sources

Aside from Rn-222 decay products, the most significant beta emitter is Co-60, produced in copper by cosmogenic activation with a total decay rate of ~ 0.04 mBq per detector housing. However, Co-60 is distributed throughout the bulk of copper, in which electrons have a mean range of $\sim 10^{-3}$ cm only [14]; since the copper housing is 3mm thick, for a uniform distribution of Co-60 only $\sim 10^{-4}$ mBq can be expected to exit copper and generate transition radiation. Compared to the $\sim 10^{-2}$ mBq of Bi-210, this can be neglected from our estimate, but should be included in the full simulation. Furthermore, betas from Co-60 have a relatively low mean energy of 95.6 keV (compared to 389 keV from Bi-210), which produces fewer TR photons per boundary crossing.

Electrons can also be emitted from copper due to Compton scattering from high-energy gammas. The isotopes most responsible for high-energy gammas are U-238, Th-232, and K-40. Aside from in Cirlex, where beta decays are dominant compared to the Compton background, they are also present in the copper housing and in dust in small amounts– K-40 has the highest total decay rate of 0.00275 mBq from dust on the inner surface of the copper housing. These contaminants are also present in much greater abundance throughout the lab, though it may be assumed that gammas originating far away from the detector are shielded with high efficiency [18]. Compton scattering also shares the same problem with Co-60 decay, as electrons must be produced in a shallow layer near the surface of the housing in order to escape it. As such, the electron background from Compton scattering can be neglected at SNOLAB, although it may be important in other settings due to higher contamination and less efficient shielding.

5.2 Cherenkov Radiation in SuperCDMS SNOLAB

Cherenkov radiation is produced under more stringent circumstances compared to TR, as any photons emitted in e.g. the copper bulk will be quickly reabsorbed;

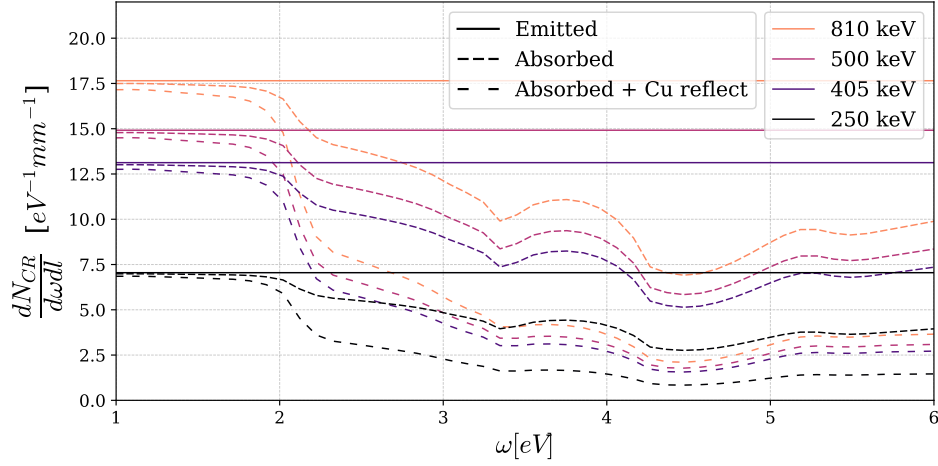


Figure 5.3: Estimated CR spectra for electrons of various energies traveling in Cirlex. Shown in solid is the flat CR emission spectrum for a constant index of refraction in Cirlex. Dashed lines show the absorption spectra after reflection. These values are likely greatly overestimated, and should only be used as upper limits compared to simulation results.

CR photons may escape if emitted within a skin depth at the surface of copper, but this is likely minimal. Certain backgrounds that we had dismissed as bulk effects in the previous section, such as the cosmogenic activation of Co-60, will not be significant sources of CR either. However, since the CR intensity is generally much higher than TR, we expect overall that the CR background should be dominant.

The dominant sources of CR are likely the Cirlex components. As previously described, these contain significant amounts of U-238 and K-40, which produce betas at average energies of 810 keV and 500 keV, respectively, above the Cherenkov threshold (~ 170 keV for $n \approx 1.5$ in Cirlex). Unlike in metals, photons produced in Cirlex have a high chance of escaping, as the absorption constant in Kapton is nearly zero at optical frequencies.

Electrons do not travel at a constant velocity over the mean track length, and many leave the thin Cirlex components before they are stopped— roughly 80% of 810 keV and 60% of 500 keV electrons are able to escape based on their angles of emission. As a rough and dirty estimate, however, we might model the energy loss as constant along the path, and calculate the Cherenkov emission using the

Mean path length	Beta energy	$N_{\text{CR}}^{\text{abs}}$	$N_{\text{CR}}^{\text{abs}}, \text{Cu-first}$
1.4 mm	250 keV	33	20
	500 keV	70	42
2.6 mm	405 keV	115	70
	810 keV	155	93

Table 5.1: Estimated number of CR photons absorbed in Si per electron in Cirlex, summed from 1 to 6 eV and over the respective mean path lengths [14]. In rows 1 & 3, the betas are assumed to begin at the full energy and slow to rest with constant energy loss, with an average energy of half the full energy; in rows 2 & 4, the betas do not lose energy at all. These values are very rough estimates and likely greatly overestimated, and should only be used as upper limits compared to simulation results.

average energy (i.e., 405 keV and 250 keV for U-238 and K-40, respectively). The precise optical properties of Cirlex are not known in detail, so we will use a constant refractive index of $n = 1.5$ over our energy range.

Fig 5.3 plots the Cherenkov spectra for electrons of various energies in Cirlex. The absorption spectra, particularly Cu-first, are greatly reduced above $\omega \gtrsim 2$ eV, but to a lesser extent than TR due to the intrinsic shape of the emission spectrum. As such, we expect that CR photons primarily produce single-electron events with significant multiple-electron production as well.

Table 5.1 shows the total CR photons absorbed from the two beta sources. Per electron, the number of CR photons emitted in Cirlex appears to exceed that of TR from Bi-210 by $\gtrsim 10^3$. This is, however, an upper limit, as our calculation deliberately ignored abridged electron tracks, nonlinear electron stopping power, photon reabsorption in Cirlex, and other particularities of the detector geometry that may significantly decrease the efficiency of CR photon absorption in Si.

Finally, since Cirlex has a low absorption constant, it also allows for the formation of hybrid transition-Cherenkov radiation (Section 4.3). The estimates made here must then be compared to the overall TR and HR emission rates in Cirlex, which were qualitatively discussed in 5.1.2 and deferred to the simulation due to the sensitivity of HR to the detector geometry.

5.3 Cherenkov and Transition Radiation in SuperCDMS HVeV Aboveground

Much like the Ge/Si HV and iZip detectors at SuperCDMS SNOLAB, the HVeV detector setup consists of a copper housing surrounding a detector crystal, with various smaller components in between. The TR background due to Bi-210 decay should be similar to that at SNOLAB after scaling for the smaller size of the HVeV detector.

More significant are the muon, cosmogenic activation, and Compton scattering backgrounds, which are expected to be considerably stronger than in SuperCDMS SNOLAB. The aboveground muon background is well-measured. The others, however, are dependent on the radioactive contamination in the lab and the detector shielding. These factors have not been extensively studied, and estimations cannot be made from known abundances of contaminants e.g. for SNOLAB.

A separate attempt has been made by Du et al.[4] to calculate the CR/TR production for an electron background dominated by Compton scattering. The paper assumes that the HVeV electron background is identical to that observed at SENSEI, but scaled up by a factor of 60 to match results from SuperCDMS CPD. In this estimate the number of CR and TR photons generated are, respectively:

$$N_{\text{CR}} \sim 10^4/\text{day}$$

$$N_{\text{TR}} \sim 10^3/\text{day}$$

for a 0.93 gram HVeV detector. This number is markedly higher than the estimate made for SuperCDMS SNOLAB, though the discrepancy may be expected as backgrounds should be far higher aboveground and with less efficient shielding.

We must also account for photons that reflect from or miss the detector, those that are produced from charges entering the detector, or any other situation where the generated TR photons are either not detected or easily rejected. In the paper by Du et al., this is represented by a normalization factor $f \approx 0.0016$, which is calculated retroactively by fitting the n -electron CR rates to the observed $n \geq 2$ electron event rates [4]. This is a rough approach which assumes that Cherenkov radiation dominates in the $n \geq 2$ electron low-energy events, and which also ignores

any energy-dependence.

Due to the lack of information about radioactive contamination in HVeV, we are unable to do a full simulation of its CR/TR backgrounds. In this thesis we will focus on simulations of SuperCDMS SNOLAB, but the estimates obtained of HVeV (particularly the relative differences between TR and CR) may be useful points of comparison.

Chapter 6

SuperCDMS Simulation Software

As discussed in previous chapters, Cherenkov and transition radiation are dominantly produced in specific components of the detector, and their contribution to the measured background is likely highly dependent on the detector geometry. Order of magnitude estimates were found analytically in Section 5, but a proper calculation was deferred to Monte Carlo simulations in Section 7.

To this end, we use the SuperCDMS simulations package known as SuperSim, built upon the Geant4 platform commonly used in detector physics. Given its modular nature, any missing physics can be easily implemented and tested alongside existing processes. In this chapter, we will give an overview of the SuperCDMS simulation software, leading up to our implementation of Cherenkov and transition radiation.

6.1 Geant4 Basics

Before discussing the specific implementation of a physics process, we should describe the basic structure and operation of Geant4. Unless otherwise noted, all information in this section will be summarized from Ref [6].

6.1.1 Runs and Events

In Geant4, an **event** (`G4Event`) is the primary unit of simulation. For input, it takes a list of primary vertices and particles, which are generated by a separate

generator object and pushed into a stack. As the event is processed, primaries are popped from the stack first-in-last-out, which may in turn generate secondary particles that are themselves pushed onto the stack. Throughout this process, the event object accumulates particle hit and trajectory data, which are output at the end of the event simulation per user specification.

Due to the stacked nature of event primaries, particles are generally independent and not related chronologically, and in fact do not interact, except for the obvious case of secondary particle production by a parent particle. After a secondary is produced, however, it no longer interacts with the parent.

A **run** is a collection of events sharing a user-defined primary generation, detector setup, and physics process list. Within a run, detector and physics settings generally cannot be changed. Primaries can be different between events, where e.g. the spatial distribution and composition is specified beforehand. For instance, a run can be configured to simulate a mix of radioisotopes distributed uniformly throughout a detector component; each event may then consist of a single decay, selected randomly according to the proportions of isotopes, at a random point in the component volume.

Events within a run are assigned unique event IDs, but are otherwise independent. Most event information is transient and not stored after event execution unless specified by the user; the `G4Event` object is itself discarded after event execution for performance reasons. Events are constructed by a singleton `G4RunManager` object, which also constructs a singleton `G4EventManager` object that handles event simulation throughout the run.

6.1.2 Particles

A “particle” in Geant4 may refer to three distinct classes that hold information about the particle: `G4ParticleDefinition`, `G4DynamicParticle`, and `G4Track`. For purposes of flexibility and performance, each class is independent and passes minimal information back and forth, only referencing each others’ data fields via pointers. A non-exhaustive list of the data stored in each object is shown in Table 6.1.

- `G4ParticleDefinition` is a base class that contains the static prop-

G4ParticleDefinition	G4DynamicParticle	G4Track
PDG ID	Energy	Track ID
Charge	Momentum	Parent ID
Rest mass	Polarization	Coordinates
Decay time	Proper time	Velocity
Physics process list		Current volume
	G4ParticleDefinition*	G4DynamicParticle*

Table 6.1: Some information contained in the respective particle classes in Geant4. Only the fields most relevant to us are listed. The * symbol indicates a pointer.

erties of a particle type and a list of relevant physics processes. Concrete particle types (e.g. `G4Electron`, `G4Gamma`) extend the base class and are each instantiated as singletons to ensure that their properties are uniform across the simulation.

- `G4DynamicParticle` is an object that stores dynamic information, unique to each *instance* of a particle. They also contain a pointer to the relevant `G4ParticleDefinition`, where all `G4DynamicParticles` of the same type point to the same `G4ParticleDefinition` object.
- `G4Track` is an object that stores geometric information and tracking metadata. Like `G4DynamicParticle`, it is unique to each individual particle, and each `G4Track` points to its respective `G4DynamicParticle` object. Despite what the name might imply, the `G4Track` object does not store past information, but is a “snapshot” responsible for information about particle tracking at any given moment.

6.1.3 Tracking and Stepping

Particle tracking proceeds via discrete steps represented by the `G4Step` object. Each step contains information about geometric quantities to be changed over the course of the step, as well as two `G4StepPoint` objects representing the spatial points before and after the step (Table 6.2).

G4Step	G4StepPoint
Step length	Coordinates
Energy deposit	Momentum
Secondary particles	Physical volume
Pre-, Post-step G4StepPoint	Material
	On Boundary?

Table 6.2: Some information contained in the `G4Step` and `G4StepPoint` classes in Geant4. Only the fields most relevant to us are listed.

Importantly, in Geant4, a track is not a collection of steps, and each track generally only contains information pertaining to the current step. Instead, a track is *updated* by successive steps, via the singleton `G4TrackingManager` and `G4SteppingManager` classes. As previously mentioned, particle tracks are pushed into a stack and retrieved as particles are independently simulated. When a particle leaves the simulation volume, slows to rest with no rest processes, or is otherwise destroyed, its corresponding `G4Track` object is deleted. As such, when more than one particle (including secondaries) is involved, a `G4Track` object does not even span the course of a single event. Persistent information between steps and tracks is instead stored in the `G4Trajectory` and `G4TrajectoryPoint` classes that can be output at the end of an event, which must be enabled by the user in the run setup.

Since different tracks cannot interact, for performance reasons each step is advanced by distance traveled rather than time elapsed. Each step's length is defined either by the distance to the next geometric boundary or the discrete physics process with the shortest mean free path, whichever is shorter; in Geant4, this is also known as the *physical interaction length* (PIL). If a physics process is activated, its PIL is recalculated at the end of the step, whereas the step length is subtracted from the PILs of all other processes [9].

6.1.4 Physics processes

Since we will be implementing our own physics processes (Section 6.3.4, their structure and essential functions are important to understand.

Physics processes are called over the course of a step, whose length is lim-

ited by the single process with the shortest remaining PIL, but more than one process may be executed. For modularity, they generally do not affect the `G4Track` directly, but accumulate their effects in `G4ParticleChange` objects that are propagated to the `G4Track` by the `G4SteppingManager`.

All physics processes extend the abstract `G4VProcess` class, which defines three categories of functions by order of execution: `AlongStep`, `PostStep`, and `AtRest`. Each category has two further functions: `GetPhysicalInteractionLength`, which calculates the step limit, and `DoIt`, which actually performs the actions of the physics process.

All functions of the same category are sorted and executed together, i.e., all `AlongStepDoIt()` functions across different processes are executed first, then all of the `PostStepDoIt()` functions, and so forth. The specific roles and ordering are as follows:

- `AlongStepDoIt()`: Actions to be taken over the course of a step, corresponding to continuous processes such as particle movement in fields. These functions only have access to the step length and track properties at the pre-step point. Each process with `AlongStep` actions returns the `G4ParticleChange` object, which `G4SteppingManager` uses to calculate the track post-step properties only when *all* active `AlongStepDoIt()` functions are complete, so ordering is unimportant.
- `PostStepDoIt()`: Actions to be taken at the end of a step, i.e. after the mean free path is traversed, corresponding to discrete occurrences such as particle scattering or decay. It has access to both pre- and post-step information, the latter of which has accumulated all changes from `AlongStepDoIt()` actions. The post-step properties are updated after *each* `PostStepDoIt()` function is executed, so ordering may matter.
- `AtRestDoIt()`: Actions to be taken while the particle is at rest. Since `Geant4` increments steps by length, particles at rest are stepped uniquely with the `AtRest` functions; when no active process has a defined `AtRest` function, the track is deleted. The post-step properties are updated after each `AtRest` function is executed.

The three categories of functions broadly correspond to continuous, discrete, and rest processes, represented by intermediary abstract classes. However, each process may implement any combination of the three functions; for instance, particle decays may occur both `PostStep` and `AtRest`.

The line between continuous and discrete blurs further as a discrete process can be forced to execute at every step, regardless of the PIL of its own. Cherenkov radiation, for instance, is intuitively a continuous process, but in Geant4 it is a discrete process invoked at every step when valid, as it must emit photons over the final step path after all other processes have been taken into account [5]. Boundary processes such as reflection and refraction do not have a PIL and are also forced to execute every step, to check if each post-step point is on a boundary.

Physics Lists

Geant4 includes a wide array of physics processes with approximations spanning different energy ranges, and the majority of them are not relevant for any single simulation. For efficiency, the list of desired particles and corresponding physics processes must be provided by the user as a **physics list**.

Physics lists are objects that inherit the abstract `G4VUserPhysicsList` class, with the `ConstructParticle()` function which constructs all desired `G4ParticleDefinition` objects, and the `ConstructProcess()` function which iterates through all particle definitions and assigns them processes. Realistically, for simulations with many processes a modular physics list should be used, which allows the user to group particle and process construction into distinct physics modules.

6.1.5 Geometry and Materials

The geometry of a simulation is described by a hierarchy of volumes. Each volume is represented by three layered classes: `G4Solid`, `G4LogicalVolume`, and `G4PhysicalVolume`. The information in each class is listed in Table 6.3.

The physical volume object contains pointers to both its own logical volume and the logical volume of an enclosing *mother volume*— all spatial coordinates used in the three volume classes are relative to the coordinate system of the mother

G4Solid	G4LogicalVolume	G4PhysicalVolume
Shape	Material	Position
Size	Sensitivity	Rotation
	Own G4Solid*	Own
		G4LogicalVolume*
	Daughters'	Mother's
	G4LogicalVolume*	G4LogicalVolume*

Table 6.3: Some information contained in the respective volume classes in Geant4. Only the fields most relevant to us are listed. The * symbol indicates a pointer.

volume. At the top of the hierarchy is the *world volume* which defines the global coordinate system, outside of which all particle tracks are destroyed.

Each logical volume can be placed multiple times, i.e. assigned to multiple physical volumes, with their daughter hierarchies intact. Physical volumes may also be placed singly or repeatedly with only one physical volume constructed. These allow for the easy duplication of geometries in e.g. QET arrays or stacks of detectors while saving memory.

The material of each volume is treated as a combination of its component elements and isotopes, and its properties are calculated by default from the material composition. The user is also able to override default calculations or specify more complicated crystal and molecular structures. Optical information can be specified using the `G4MaterialPropertiesTable` (MPT) class, which act as maps that assign arrays of quantities to user-defined strings. The MPT is able to account for energy dependence by interpolating over each array of quantities using a corresponding array of energies.

6.2 The SuperSim Package

SuperSim is the SuperCDMS-specific implementation of Geant4, which covers the simulation of a source, its interactions with a detector, and the subsequent detector response [8]. Included in SuperSim are the various detector geometries and lab environments used by the SuperCDMS collaboration, along with any relevant backgrounds.

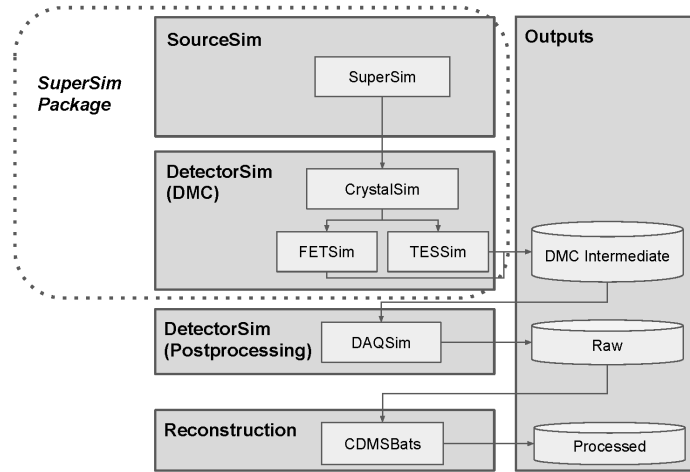


Figure 6.1: Data flow in the SuperCDMS simulation software, including the basic structure of the SuperSim package [8].

6.2.1 SuperSim Structure

The general structure of the SuperCDMS simulation is shown in Fig 6.1; misleadingly, “SuperSim” may refer to both the source simulation and the whole package which contains the source and detector simulations. Here, we will refer to the source simulation alone as “SourceSim,” though this is imprecise as SourceSim includes the input configuration and postprocessing workflow in addition to the core Geant4-based code.

The source and detector simulation parts are independent and can be run separately for intermediary testing and visualization. In this section we will discuss the basic functionality of each.

- **SourceSim** handles the simulation from the input Geant4 configuration macro to the accumulation of particle interactions in the detector. As output it provides a list of these interactions (“hits”) and their respective position, charge, energy, and other information; internally, this is known as the “Particle Hits format”, which may take different concrete forms as different needs may require.
- **DetectorSim** handles the detector response to the particle hits found with

SourceSim. The Geant4-based part of DetectorSim is also known as G4DMC (“Geant4 Detector Monte Carlo”), which uses the external G4CMP (“Geant4 Condensed Matter Physics”) library for physics not included in base Geant4.

Crucially, G4CMP includes support for crystal lattices that allows it to perform detailed phonon simulation [9]. It also includes field interpolation from meshes produced externally via finite element analysis, which allows for particles to interact with very intricate EM fields where an analytical description is untenable. In turn, G4CMP also provides detailed simulation of charge-carrier transportation and Luke phonon emission, among other important charge processes.

The Particle Hits files are first read into **CrystalSim**, which analyzes the recoil properties and performs the corresponding energy partition between phonon and charge-carrier production. These phonons and charge-carriers are then propagated through the detector using G4CMP physics processes, decaying or producing secondary particles where necessary. Finally, once they arrive at an instrumented surface (i.e. with TESs and FETs), they have a probability of being absorbed, proportional to the amount of sensor material covering each surface and calibrated to real data [9].

The CrystalSim hits may then be read into **TESSim** and **FETSim**, which simulate their respective readout signals. In total, when all functionality is enabled, G4DMC produces two files: one containing the particle hits from CrystalSim, and another containing pulse traces from the sensor simulation.

6.3 Implementation of Transition and Cherenkov Radiation in SuperSim

6.3.1 The Electromagnetic-Optical schism

EM physics in Geant4 are separated into “electromagnetic” and “optical” categories, with corresponding physics builders for each [7]. The former is by far the larger category, containing models of simulated EM processes down to ~ 1 keV scale; the additional low-energy electromagnetic package can extend the energy

scale further down to ~ 100 eV, and the medical physics G4-DNA package extends down to ~ 10 eV for processes relevant to microdosimetry [92].

The latter, “optical” category focuses directly on the optical energy range, with a smaller set of physics processes for e.g. reflection, refraction, and absorption that generally *are not related* to the higher-energy “electromagnetic” processes. Importantly, the “electromagnetic” physics builder constructs the `G4Gamma` class as its photon particle, whereas the “optical” physics builder constructs the separate `G4OpticalPhoton` class as its photon. Processes in each category interact with their own photon type, and never the twain shall meet.

The estimates of CR/TR production in Section 5 found that the final absorption rate of CR/TR photons in the detector crystal may be highly dependent on the reflection and absorption rates of photons in other detector components. Our desired CR/TR implementation must therefore produce optical photons in order to interact with the optical reflection (`G4OpBoundaryProcess`) and absorption (`G4OpAbsorption`) processes.

6.3.2 Existing implementations

Cherenkov radiation

Base Geant4 implements Cherenkov radiation (`G4Cerenkov`) as a discrete “optical” process invoked at every step when valid. The process follows the general structure of all physics processes (see Section 6.1.4). Detailed operation is as follows [5]:

- `PostStepGetPhysicalInteractionLength()`: By default, CR is turned off, and the PIL is set to the maximum `double` value so it never limits a step. First, the function checks if CR is possible in the material at all by checking if the maximum index of refraction produces a minimum threshold $\beta_{\text{CR}} < 1$. Then, it calculates the distance until the particle drops below the Cherenkov threshold using the energy loss (dE/dx) data of the material. If this range is positive, it is set as the PIL, and the process is forced to invoke at every step.
- `PostStepDoIt()`: This function is invoked after other processes have de-

terminated the particle trajectory over the course of the step. It first calculates the average number of photons expected from Eq 4.5 [7], and generates a Poisson random variable to find the number of photons emitted in this step. Then, it constructs the `G4DynamicParticle` and `G4Track` objects for each secondary `G4OpticalPhoton`, distributes them randomly over the step length, and finally pushes them to the `G4ParticleChange` output. All CR photons are assumed to be very soft and affect the particle trajectory by negligible amounts.

There are some insufficiencies in the `G4Cerenkov` process, however, that prevent us from using it without major modifications. First, it only takes into account the real index of refraction. This is a reasonable approximation for the transparent non-metals in which Cherenkov radiation is most commonly relevant, but becomes problematic in e.g. silicon, where the imaginary index can be negligible or large depending on the energy. Second, the `G4Cerenkov` process assumes that materials are normally dispersive, where the real index increases monotonically with energy; hence, the maximum index is identified with the index at the maximum photon energy, and in turn the minimum Cherenkov threshold is the Cherenkov threshold of the maximum photon energy. In materials where the real index is a more complicated function or decreases with energy, the process emits either the wrong amount of CR or no CR at all.

Finally, the existing `G4Cerenkov` process handles CR independently, whereas we need to relate it to hybrid radiation. As discussed in Section 4.3, HR occupies an intermediary position between transition and Cherenkov radiation, with both a TR-like broad angular distribution and CR-like divergent peaks. Running both the HR and CR processes in a single simulation step would be double counting, so we need to add a mechanism to turn off CR when HR is active.

Transition radiation

There does not appear to be a ready-made process for generic TR at a single boundary, nor for TR at optical frequencies. Existing TR implementations are of various X-ray transition radiation (XTR) scenarios (e.g. `G4ForwardXrayTR`) and make extensive use of approximations specific to the X-ray energy range [7]. Further-

more, the existing TR processes tend to be suited for radiation from many densely spaced boundaries such as layers of foil or foam. These are *XTR radiators* commonly used in collider experiments for beam particle discrimination, where coherence effects from consecutive boundaries increase the total X-ray radiation yield. These are also entirely irrelevant to our investigation.

6.3.3 Optical properties of materials

The following section discusses recent work by Dr. Birgit Zatschler of the SuperCDMS Collaboration.

Before any optical processes can be used, materials must be given optical properties. General properties are specified via the `G4MaterialPropertiesTable` class, which allows for the generic mapping of quantities to energy. Important properties such as the index of refraction, absorption length, and reflectivity have been added for a variety of detector materials, using data found in Ref [93].

Also important are optical surfaces, constructed as `G4OpticalSurface` objects and attached to their respective logical volume. These are especially necessary to ensure proper functionality with G4DMC. For instance, an optical photon absorbed at a metal surface is destroyed at the surface, spawning an electron-hole pair with one of the charge carriers immediately leaving the medium. Previously, germanium and silicon were treated as metals by optical processes, and using the default behavior would result in an incorrect energy deposit. Replacing the metal surface with a new `CreateSemiconductorFinish()` function adds dielectric behavior, and allows electron-hole pairs to be produced at a skin depth inside the medium.

6.3.4 Hybrid radiation physics process

Evidently, new physics process(es) must be written to address the insufficiencies of the existing Cherenkov process and to add a generic optical transition radiation process. Both processes must also be able to communicate in order to prevent double counting in the hybrid radiation regime. To this end, we can combine TR, CR, and HR in a single `CDMSOpticalTCR` process.

First, we recall that the HR formation length is angle-dependent (Eq 4.11),

and that the HR angular distribution can be characterized by two components: a divergent CR-like peak that is constrained by divergent formation lengths (Section 4.3.2), against a broad TR-like background with very short formation lengths (SFL). Since the CR-like long formation lengths (LFL) may easily exceed the simulation step length, HR may be split into multiple steps:

- Before the charge arrives at the boundary, it undergoes pure CR by default.
- First, the charge arrives at the boundary, CR is turned off, and HR is emitted for the SFL angular region dominated by TR; it is assumed that the entirety of the SFL will be traversed in the next step, so the TR-like radiation is emitted fully.
- Second, the charge enters the medium proper. In the LFL angular region, HR is emitted at the length-differential HR rate found in Eq 4.9. This continues as long as the charge has not traversed the maximum formation length, and has not changed velocity by scattering.
- After reaching the maximum formation length or scattering, HR is aborted and pure CR is reactivated. The CR-like length-differential rate should join fairly smoothly into pure CR (Fig 4.8).

The SFL and LFL angular regions are not easy to define, nor are the CR-like divergences easy to find analytically: the CR-like peaks are located at the Cherenkov angles, but this is complicated in reality as HR considers the Cherenkov radiation of image charges, and the refraction and total internal reflection thereof. Instead, we calculate the locations of divergences numerically by finding the local minima of denominator of Eq 4.7 with respect to emission angle and energy.

Then, the LFL angular region $\Delta\theta$ is defined as the region around the divergence for which the mean free path in the material is shorter than the formation length. Thus, in the LFL region the particle can be expected to scatter before the full formation length is traversed, and vice versa in the SFL region. If no divergences are found, or if the mean free path is always longer than the formation length, then pure TR occurs and only the first step listed above is performed.

Another difficulty lies in the integration of extremely narrow and tall peaks in the HR distribution (e.g. Fig 4.5). Currently, the numerical integration method

used in `CDMSOpticalTCR` is simple Riemann integration, where the accuracy in handling narrow features is entirely dependent on the size of each Riemann bin. When a bin is too wide, it tends to vastly overestimate the integral as the height of the bin may be evaluated close to the peak of the narrow feature. Simpson and more advanced integration methods can be used for slight improvements at the same bin density, but each bin takes more calculations and the average per-calculation performance is not improved (or even worsened).

Currently, this problem is mitigated by integrating with a non-uniform Riemann grid, where bins in the LFL region (i.e. near the peaks) are $\sim 1000\times$ denser than outside. This still suffers from inefficiency as the LFL region may be wide enough that most of it does not need to be integrated with the denser grid; however, the required density and width of the denser grid is hard to determine a priori, so some inefficiency is expected and preferred over larger errors in calculation.

Finally, certain values calculated at the first step (e.g. the HR distributions in Eq 4.7) are retained as `CDMSOpticalTCR` instance variables to be used in subsequent steps for the LFL radiation. Some sort of information saving is necessary, as the `G4Track` object does not retain information from previous steps. Data crucial to HR calculations such as the previous material, the incidence angle, or the particle velocity would be otherwise discarded.

Physics processes are constructed as singletons, so the `CDMSOpticalTCR` instance variables are not properly unique to each individual particle. However, since tracks are simulated individually with no mutual interactions, in practice the `CDMSOpticalTCR` instance variables are relevant to only one particle at a time. Even when multithreading, physics processes are *thread-local*, meaning that each thread retains its own copy of each physics process object [6].

The implementation of `CDMSOpticalTCR` is as follows:

- `PostStepGetPhysicalInteractionLength()`: Calculates the maximum formation length in the current material (Eq 4.8) and sets it as the PIL. Also forces the process to invoke at every step; this is necessary to check if the particle has arrived at a valid boundary.
- `PostStepDoIt()`: Once all particle and material attributes have been imported, for a particle **on a boundary** the following actions are performed for

both forward and backward radiation:

- Generate a *uniform* grid over θ , ϕ , and ω for Riemann integration.
- Using the uniform grid, calculate formation lengths, divergences, and the long-formation-length angular ranges.
- Generate a second, *non-uniform* grid with information found in the previous step.
- Recalculate formation lengths, divergences, and angular ranges using the more refined non-uniform grid, then save them as class instance variables to be used in subsequent steps.
- Calculate the HR formula (Eq 4.7) to determine the average number of photons emitted for each bin, again saving as class instance variables to be used again later.
- For Riemann bins in the short-formation-length angular region, generate Poisson variables to determine the actual number of photons emitted for each bin (usually zero, since each bin should be small).
- If necessary, construct `G4OpticalPhoton` secondaries distributed randomly over the angle and energy range of each bin. Push the secondaries to the `G4ParticleChange` object and return.

For a particle that has **left the boundary but has yet to scatter**, the following actions are performed for the CR-like radiation, again both forwards and backwards when applicable:

- Retrieve the long-formation-length angular regions and HR emission numbers calculated in the previous step.
- Calculate the length-differential HR emission rate (Eq 4.9) to find a non-divergent result and scale by the current step length.
- For Riemann bins in the long-formation-length region, generate Poisson variables to determine the actual number of photons emitted for each bin.

- If necessary, construct `G4OpticalPhoton` secondaries distributed randomly over the angle and energy range of each bin. Push the secondaries to the `G4ParticleChange` object and return.

Otherwise, for a particle that either **has not reached a boundary or has completed HR**, pure CR is performed instead:

- Calculate the photon energies that can be emitted, and their respective Cherenkov angles θ_{CR} and average emission rates.
- Generate Poisson variables to determine the actual number of photons emitted.
- If necessary, construct `G4OpticalPhoton` secondaries distributed randomly over ϕ and the allowed energies. Push the secondaries to the `G4ParticleChange` object and return.

6.3.5 Future efficiency improvements

Compared to the other optical processes in Geant4/SuperSim, the efficiency of `CDMSOpticalTCR` is quite abysmal. Primarily, computation time is tied up in the calculation of various quantities for each of the Riemann bins, whose accuracy is highly dependent on the density of bins and the overall runtime.

Incorporation of HR simulation in any real experimental simulation pipeline will have to make use of lookup tables. Geant4 also allows for the runtime generation of physics tables via the `G4PhysicsTable` class and its corresponding `BuildPhysicsTable()` function; this functionality is already utilized in `G4Cerenkov`. Since HR calculation is dependent on the refractive indices of two materials, the velocity of the charged particle, and its incidence angle, the size of its physics table may be very large and require significant reductions in resolution, which may or may not be acceptable. The tradeoff between memory usage and simulation accuracy should be investigated in the future.

The divergence and long-formation-length angular range calculation should also be replaced with smarter algorithms. Currently, they are calculated over the entire Riemann grid *twice*, first roughly over a uniform grid, then again over the

refined non-uniform grid; the divergence, which should be a minimization problem of the HR distribution denominator, is found instead by brute force.

Chapter 7

Transition and Cherenkov Radiation Simulation

Using the software described in the previous chapter, we will attempt to simulate the effects of transition and Cherenkov radiation in SuperCDMS detectors. Our simulations will be compared to the theoretical predictions made in Chapter 5, first validating its physics using a simple beam of electrons, and then calculating the optical backgrounds produced for the radioisotopes embedded in various detector components. Certain backgrounds proposed in Chapter 5, such as the TR/CR produced from isotopes in Cirlex, were deferred then due to their dependence on the detector geometry and will also be presented in this chapter. Finally, we will offer an estimate of the expected TR/CR contribution to low energy backgrounds at SuperCDMS SNOLAB, provided its detailed background model, though more work will be necessary in the future to validate and expand on the results presented here.

Throughout this section, we will talk about numbers of *hits* and *events*. The former counts optical photons that enter the detector crystal volume, whereas the latter refers to primary particles (e.g. electrons) or decays (e.g. of Pb-210), which may or may not produce optical photons. The *hit rate* (or *hits/event*) is the number of optical photons that enter the detector crystal per primary particle, and corresponds to the average *absorption rate* calculated in Section 5. For more information about events in the language of Geant4, see Section 6.1.

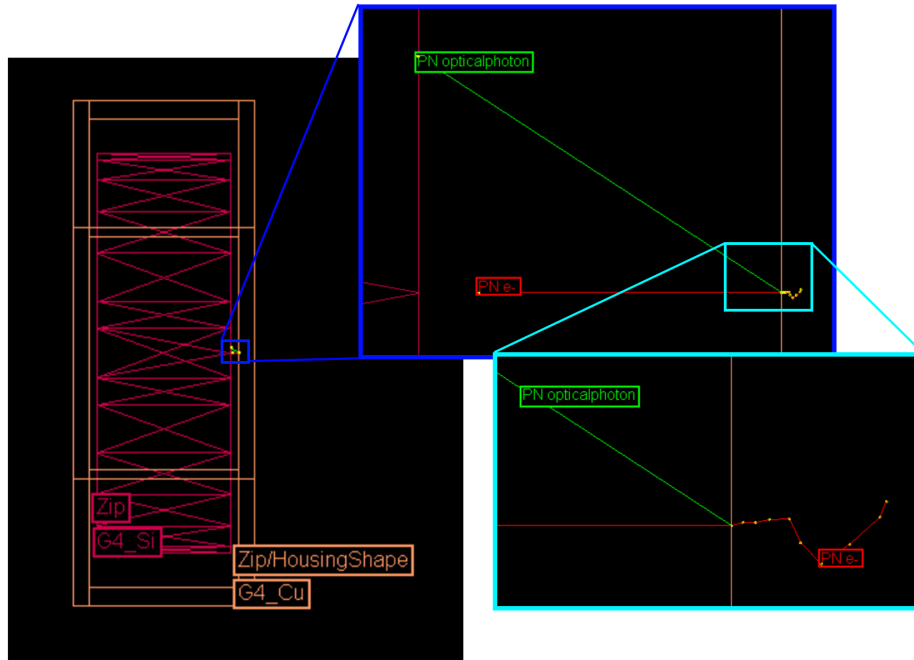


Figure 7.1: Visualization of the electron beam aimed at the center of an internal copper face, which produces the events shown in Fig 7.2a. The detector crystal (Zip) is shown in magenta, the copper housing in orange, the electron in red and the TR photon in green. The deepest level of zoom (cyan) shows the electron scattering in copper, which has a chance of escaping copper. The visualizations were produced using the HepRApp software [10].

7.1 Electron Beam on Copper

We will first consider transition radiation emitted from copper, with a high absorption constant that suppresses the Cherenkov-like component of hybrid radiation. This allows for a relatively “pure” transition radiation that can be considered separately from Cherenkov radiation.

Fig 5.1 of Section 5.1.1 showed the expected energy distribution of TR produced from average Bi-210 decay (389 keV) electrons normally incident on copper, along with the TR absorption rates after reflections. A preliminary test of our simulation was performed by firing a beam of 389 keV electrons at the center of

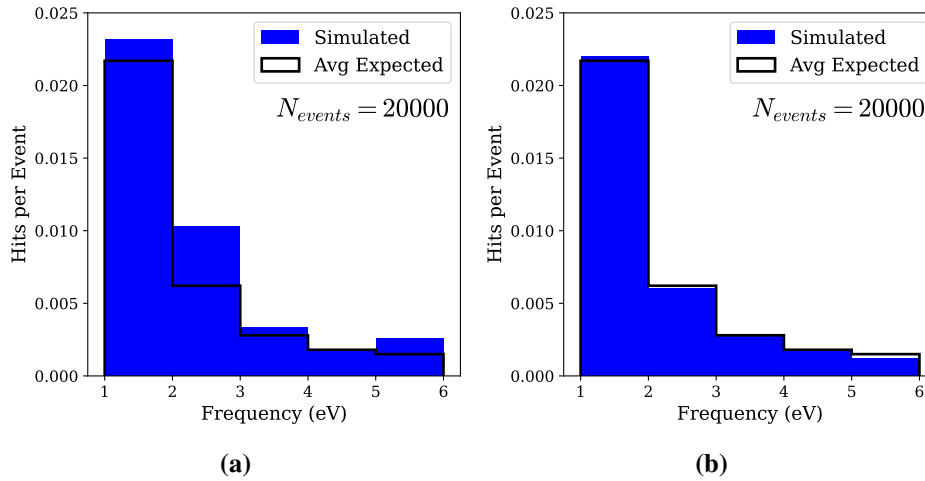


Figure 7.2: Energy spectra of backward TR produced from a beam of 389 keV electrons normally incident on a copper surface. In (a) electrons are allowed to freely exit and reenter the copper housing, whereas in (b) electrons are not allowed to exit copper. The measured spectra from our Monte Carlo simulation (Ch 6) is shown in blue; the expected spectra (integrated from the “absorption” distribution in Fig 5.1) is shown in black outline.

the copper housing (Fig 7.1). The energy spectrum for 20,000 simulated events, along with the predicted distributions integrated over energy bins, are shown on in Fig 7.2a.

The measured spectrum in Fig 7.2a shows increased hit rates compared to the expected spectrum, especially at low energies. This is due to TR produced from electrons exiting and reentering copper, which was not accounted for in the original estimate but is a non-negligible contribution to the total TR background.

To validate our simulation, a special process is added which destroys all electrons as soon as they enter the copper housing, allowing only the initial TR to be produced. Fig 7.2b shows the measured spectrum with this extra restriction, which follows the expected spectrum quite well.

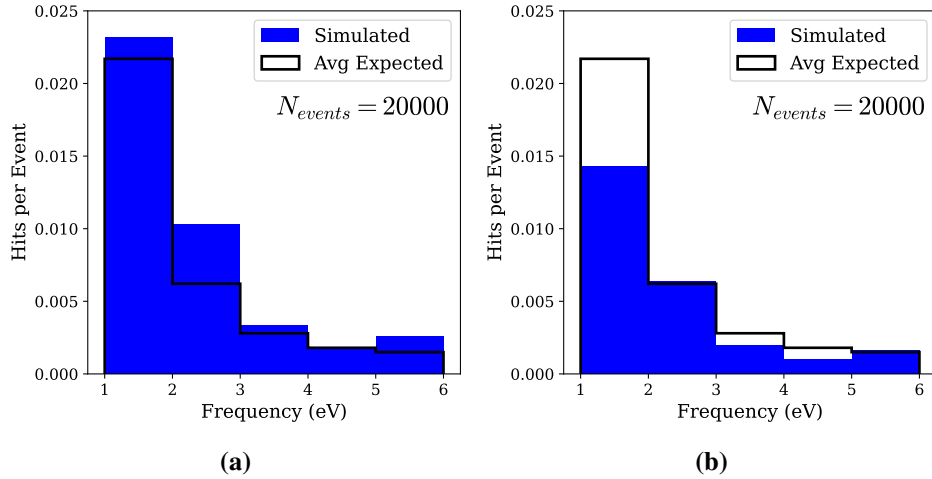


Figure 7.3: Energy spectra of backward TR produced from a beam of 389 keV electrons normally incident on a copper surface. Fig (a) is identical to Fig 7.2a, reproduced here for comparison to (b), where primary rejection has been applied that removes all TR photons coincident with a charged particle hit. The overall effect is that the hit rates are reduced to below our initial estimate (black outline).

7.1.1 Primary Rejection

Electrons escaping copper may themselves hit the detector to produce a large ionization yield. These relatively high-energy events can be easily detected and are generally already handled by existing trigger and cut conditions, and do not contribute to the unexplained low energy background. Any optical photons associated with such an event will likewise be removed, as the trigger rate is much slower than the travel time of light in the detector housing.

To account for this, we will apply “primary rejection” (PR) to simulation results, which rejects all optical photons accompanying a primary charge (e.g. an electron or a recoiling nucleus), which removes all events where a non-photon particle hits the detector. This should remove many, but not all, TR photons produced from electrons exiting copper. The result of primary rejection is shown in Fig 7.3b, which shows a significantly reduced hit rate compared to the estimate.

Primary rejection will be especially important once we allow charges to interact with non-copper materials. The transparency of the detector crystals to low

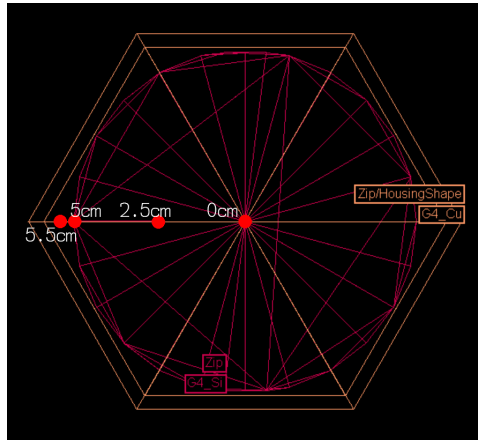


Figure 7.4: Test points for checking position dependence of electron sources to TR absorption. A 389 keV beam of electrons, as in Fig 7.1, is fired at each point normally to the inner surface of the copper housing. Results are given in Table 7.1.

energy photons allows for abundant hybrid and Cherenkov radiation within the detector crystal itself; these are likely the dominant sources of optical radiation backgrounds, but are all easily removed as they require that charges enter the detector directly.

7.1.2 Position Dependence

In Chapter 5, we predicted intuitively that the true hit rates of TR (and the efficiency of primary rejection) would be highly dependent on the specifics of the detector geometry. If TR/CR were a significant contribution to low energy backgrounds, this could also in part explain the discrepancies between observed backgrounds in various experiments (Section 3).

As a quick verification of this assumption, we can repeat the beam gun simulation at different points in the detector (Fig 7.4). The results both pre- and post-primary rejection are shown in Table 7.1. It appears that the post-PR hit rate increases slightly towards the edge of the detector, which suggests that electrons can escape through the gap between the detector and housing rather than hitting the detector. More effects of position dependence will be shown once other detector

Radius	Hits/Event	Hits/Event, post-PR
0.0 cm	0.041(1)	0.025(1)
2.5 cm	0.046(2)	0.027(2)
5.0 cm	0.040(2)	0.039(2)
5.5 cm	0.038(2)	0.029(2)

Table 7.1: TR simulation results from a 389keV electron beam fired at each of the test points in Fig 7.4. “Post-PR” refers to the hit rate after primary rejection. The standard error of the mean is given for uncertainties.

components and hybrid radiation are taken into account.

7.2 Bi-210 Decays in Copper

In Sections 2.3 and 5.1.1, we discussed the deposition of Rn-222 decay products in the surface of copper as a possible source of electron background. For us, the most relevant isotope is Bi-210, which decays at an average electron energy of 389 keV.

The TR background from Bi-210 decay was simulated with an even coating of Bi-210 on the inner surface of the copper housing, deposited with a uniform depth distribution up to 10 nm into the copper. The measured spectra pre- and post-primary rejection are shown in Fig 7.5.

Compared to the electron beam spectra from the previous section, the raw hit rates from Bi-210 decay are significantly lower. This is due to two main factors: first, Bi-210 decays are assumed to produce betas isotropically, so only \sim half of all betas cross the copper surface. Second, while the previous section simulated a monoenergetic beam of 389 keV electrons, the actual energy distribution of Bi-210 betas is skewed towards lower energies, with a median energy lower than the 389 keV mean.

Applying primary rejection lowers the Bi-210 TR background dramatically, proportionally much more than the that applied to the 389 keV beam (Fig 7.3b). There, the beam was shot into copper, and only a minority of electrons scattered back out of copper and into the detector; for Bi-210 decay, electrons are emitted out of copper, and a majority of electrons proceed to hit the detector itself. Furthermore, in Bi-210 decay the resulting Po-210 nucleus may itself recoil out of copper

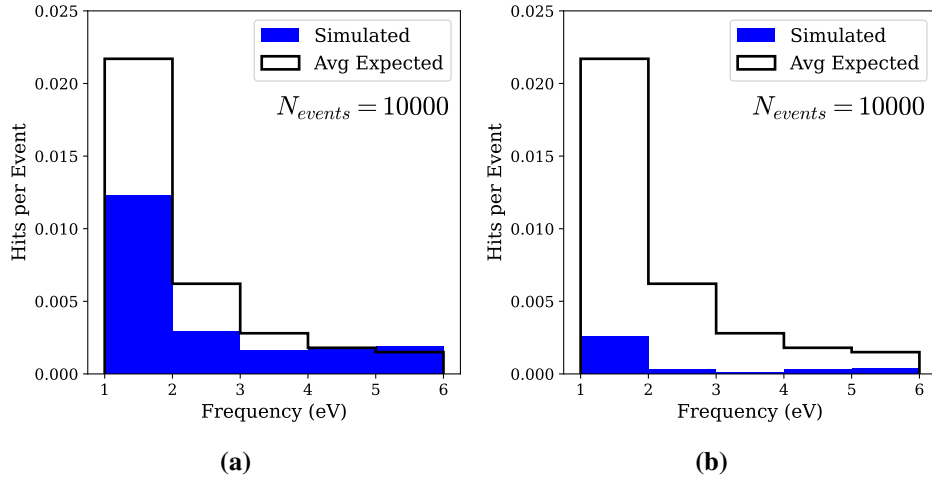


Figure 7.5: Energy spectra of TR produced from Bi-210 decays, distributed evenly over the inner surface of the detector housing at a skin depth of up to ~ 10 nm. Raw hit rates are shown in (a), whereas the hit rates after primary rejection are shown in (b). The expected spectrum from a monoenergetic 389 keV electron beam is shown in black outline, which we now see was likely an overestimate of the Bi-210 decay TR hit rate.

and into the detector, which allows us to reject a further fraction of events.

The 10 nm skin depth used for Bi-210 deposition in copper is an approximate mean value [60], and may be quite different in practice; for larger depths, smaller fractions of betas are able to escape copper with lower average velocities. Table 7.2 shows the total hit rates simulated for different depths. There does not appear to be a clear dependence on depth until $\sim 10^3$ nm, which suggests that a ~ 1 order of magnitude of difference in skin depth is unlikely to change results significantly.

7.3 Hybrid Radiation in Cirlex

7.3.1 Pa-234 and K-40

The other expected major source of CR/TR are betas produced by radioisotopes throughout the bulk of Cirlex. Since Cirlex is fairly transparent (compared to copper), optical photons produced in the bulk have a good chance of escaping, and

Skin Depth	Hits/Event	Hits/Event, post-PR
10^0 nm	0.022(1)	0.004(1)
10^1 nm	0.021(1)	0.004(1)
10^2 nm	0.023(1)	0.005(1)
10^3 nm	0.019(1)	0.0036(9)
10^4 nm	0.019(1)	0.0026(7)
10^5 nm	0.011(1)	0.0017(5)

Table 7.2: Hit rates of 1~6 eV TR photons produced from Bi-210 decays, distributed evenly over the inner surface of the detector housing to various depths. “Post-PR” refers to the hit rate after primary rejection.

Isotope	Activity (mBq)	Hits/Event	Hits/Event, post-PR	Hits/Year
Pa-234	0.052	2.67(5)	0.009(1)	15(2)
K-40	<0.020	2.36(8)	0.043(3)	<29

Table 7.3: Hit rates of 1~6 eV HR+CR photons from Cirlex in a single detector, for 10,000 events simulated per isotope. “Post-PR” refers to the hit rate after primary rejection.

hybrid radiation becomes an important consideration: with small ($\lesssim 0.001$) absorption constants, the angular distributions are divergent in the direction of Cherenkov radiation, and must be normalized by the divergent formation length (Section 4.3).

In the simulation, twelve slots are made in the hexagonal copper housing, with two on each side. Eight of these slots are filled with Cirlex DIB connectors, and four are left empty (Fig 7.6). Two main beta-emitting isotopes, Pa-234 and K-40, are present in the decay chains of Cirlex radiocontaminants with activities of 0.052 mBq and < 0.020 mBq, respectively.

Back in Section 5, we predicted that $10 \sim 100$ CR photons of 1 to 6 eV would be emitted per electron in Cirlex. Table 7.3 gives the simulated values of optical photons absorbed in the detector crystal (including the TR contribution). This is $1 \sim 2$ orders of magnitude lower than the predicted CR production, as the majority of optical photons do not escape Cirlex, and a further fraction are absorbed directly into copper.

Fig 7.7 shows the absorbed spectra after primary rejection, which reduces the

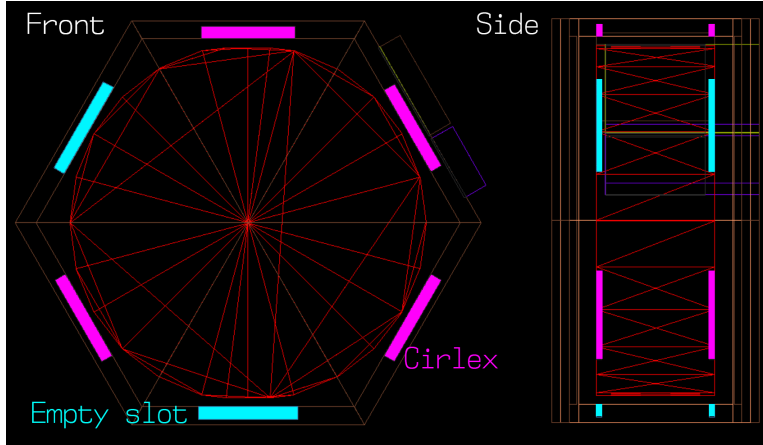


Figure 7.6: Visualization of the SuperCDMS SNOLAB detector with instrumentation. The detector crystal (Zip) is shown in red wireframe, copper housing in orange, Cirlex DIB connectors in magenta, and empty slots in teal. The visualizations were produced using the HepRApp software [10].

hit rate by a couple more orders of magnitude. The K-40 contribution, with a relatively weak 500 keV beta compared to the average 810 keV beta of Pa-234, actually becomes dominant after the primary rejection cut. This is likely due to its weaker electron, which has a smaller chance of escaping Cirlex or producing gamma radiation, and in turn impinges fewer particles on the detector.

Using the upper limit of K-40 activity, the post-rejection HR hit rate from Cirlex is ~ 44 photons/year/detector for $1 \sim 6$ eV photons (Table 7.3). In the previous section, we found that the TR hit rate from Bi-210 decay is ~ 0.004 per event, which for a contamination of ~ 0.01 mBq gives ~ 1 photons/year/detector. At SNOLAB, it appears that the pure TR contribution to the optical background is likely subdominant by about an order of magnitude compared to HR + CR.

7.4 CR and TR energy ranges

For transition radiation from a particle beam on copper (Section 7.1), our simulation calculated the TR/HR distributions (Eq 4.7) over a narrow energy range of 1 to 6 eV. This range was selected as a direct comparison to the estimates made in

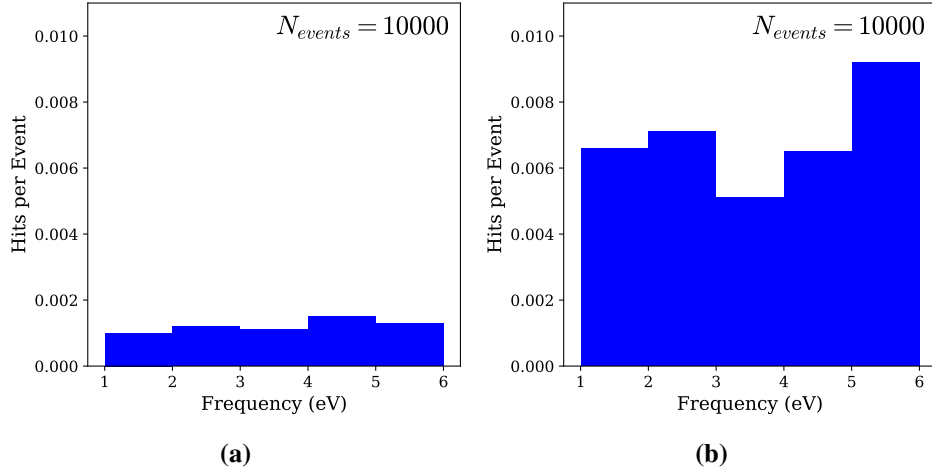


Figure 7.7: Simulated energy spectra of HR+CR between 1 and 6 eV after primary rejection, produced from (a) Pa-234 decays and (b) K-40 decays, each distributed evenly over the bulk of Cirlex components (Fig 7.6). 10,000 events were generated for each isotope.

Chapter 5, and is fairly reasonable as we’ve shown that the TR spectrum is heavily suppressed below ~ 2 eV (Fig 7.3b).

The detector crystals have band gap energies of ~ 1 eV and average electron-hole pair energies of ~ 3 eV, so the 1 to 6 eV energy range also roughly corresponds to the energy range of single-electron events. Since low energy excesses have been observed up to ~ 100 eV, it seems unlikely that TR contributes significantly to the bulk of the low energy excess, or at all for detectors with $\gtrsim 10$ eV trigger thresholds (e.g. the HV detectors at SuperCDMS SNOLAB). TR may become relevant as more detectors reach sub-eV resolutions in the future, however.

In our Cherenkov-heavy simulations, we considered the same energy range of 1 to 6 eV, again for direct comparison to our estimates. Unlike TR, however, CR is relevant at higher energies – in principle, the CR spectrum should be considered for the entire low energy backgrounds ($\lesssim 100$ eV) region. Currently, the refractive index of copper has only been implemented in SuperSim up to around 8 eV, and more studies of CR must be done once the available energy range has been expanded.

Crucially, Cherenkov radiation can produce a significant background of multiple-

electron events: as discussed in Section 2.2.2, single-electron events from charge leakage are a prominent background in high voltage detectors, which likely drowns out TR and CR in the single-electron energy range. On the other hand, the broad energy range of CR allows it to extend past the charge leakage background, where it may be the dominant background in other parts of the energy spectrum. A deeper analysis will be required in the future to compare simulation results against data from HVeV, especially once it is operated underground and with detailed background models.

Chapter 8

Conclusions

In this thesis we have presented an overview of the unexplained low energy backgrounds found in various eV-scale dark matter detectors, motivating an investigation of Cherenkov radiation (CR) and transition radiation (TR) as hypothetical origins of these backgrounds.

The intermediary phenomenon between Cherenkov and transition radiation, known as hybrid transition-Cherenkov radiation or HR, posed a significant challenge to calculations of TR in transparent media – the generalized TR/HR distributions (Eq 4.7) also contain Cherenkov radiation, which when integrated over all space display sharp divergences that vastly overestimate the radiation intensity. By treating HR alternately as delocalized TR or finite-path CR, we have shown that the divergent peaks can be normalized using the HR formation length (Section 4.3.2). The formation length can in turn be defined to allow HR to transition smoothly into CR in the appropriate parameter region, which gives us a generalized way of numerically calculating TR and CR that is appropriate for materials of any complex indices of refraction.

After making some analytical estimates of CR and TR backgrounds in SuperCDMS SNOLAB detectors, we discussed the implementation of CR and TR in the Geant4-based Monte Carlo simulation software used at SuperCDMS (Section 6.3.4). Our new `CDMSOpticalTCR` process performs numerical integrations over the HR distribution using the formation length normalization method, and separates HR into long- and short-formation length angular regions, corresponding to

its CR-like and TR-like components respectively.

Preliminary simulations using our new process show that, given the radiocontamination present at SuperCDMS SNOLAB, a TR/CR background rate of $\sim 10^1$ events can be expected per year per detector. The primary contribution to this background comes from CR produced in Cirlex, with a secondary contribution from TR produced by Pb-210 decays that is subdominant by about an order of magnitude.

Importantly, the TR spectrum is suppressed below ~ 3 eV (Fig 7.3b), such that TR produces a measurable background, if any at all, of single electron-hole pairs only. Given the presence of charge leakage as a known major source of single-electron events, the TR background is subdominant and likely indistinguishable from the charge leakage background, unless the latter is identified and efficiently removed in the future. Furthermore, since SuperCDMS detectors (with the notable exception of HVeV) do not have single-charge resolution, TR likely does not explain the observed low energy excesses up to ~ 100 eV.

On the other hand, the CR spectrum is comparatively flat above 3 eV (Fig 7.7), which allows it to generate multiple-charge events distinct from the charge leakage background and may explain some of the observed low energy backgrounds.

These are only preliminary analyses, however, using simple detector geometries, a handful of important radioisotopes, and a narrow energy range. More thorough simulations and further physics validations must be carried out in the future. In particular, since the HVeV detector has previously only been operated above-ground without a comprehensive background model, we cannot yet compare simulation results to the low energy excesses measured by HVeV. Plans are in place to operate HVeV underground at CUTE, which will hopefully allow direct comparisons and validations to be performed.

Bibliography

- [1] N. Kurinsky, D. Baxter, Y. Kahn, and G. Krnjaic, *Phys. Rev. D* **102**, 015017 (2020).
- [2] V. P. Zrelov, V. P. Lupiltsev, and J. Ruzicka, *Nucl. Instrum. Meth. A* **270**, 62 (1988).
- [3] SuperCDMS Internal, Background from Transition Radiation, <https://confluence.slac.stanford.edu/x/W7V2E>, Accessed July 28, 2021.
- [4] P. Du, D. Egana-Ugrinovic, R. Essig, and M. Sholapurkar, (2020), arXiv:2011.13939.
- [5] Geant4 Collaboration, *Geant4.10 Documentation*, <https://apc.u-paris.fr/~franco/g4doxy4.10/html/index.html>.
- [6] Geant4 Collaboration, *Geant4 User's Guide for Toolkit Developers*, Release 10.7.
- [7] Geant4 Collaboration, *Geant4 Physics Reference Manual*, Release 10.7.
- [8] SuperCDMS Internal, SuperSim Package Home Page, <https://confluence.slac.stanford.edu/x/h4bsDgE>, Accessed June 30, 2021.
- [9] R. Agnese, *Simulating the SuperCDMS Dark Matter Detector Response and Readout*, PhD thesis, University of Florida, 2017.
- [10] HepRApp - HepRep Browser, <https://www.slac.stanford.edu/~perl/HepRApp/>, Accessed July 28, 2021.
- [11] Planck Collaboration, N. Aghanim *et al.*, *Astronomy and Astrophysics* **641**, A6 (2020), arXiv:1807.06209.
- [12] Particle Data Group, P. Zyla *et al.*, *PTEP* **2020**, 083C01 (2020).

- [13] SuperCDMS Internal, SuperCDMS Background Explorer, <https://bgexplorer.pnnl.gov/supercdms/>, Accessed July 30, 2021.
- [14] M. Berger, J. Coursey, and J. Chang, Stopping-Power & Range Tables for Electrons, Protons, and Helium Ions: NIST Standard Reference Database 124., <https://physics.nist.gov/PhysRefData/Star/Text/method.html>, Accessed June 21, 2021.
- [15] V. C. Rubin, J. Ford, W. K., and N. Thonnard, *The Astrophysical Journal* **238**, 471 (1980).
- [16] D. Clowe *et al.*, *The Astrophysical Journal* **648** (2006).
- [17] J. L. Feng, <http://arxiv.org/abs/1003.0904v2>.
- [18] SuperCDMS Collaboration, R. Agnese *et al.*, *Phys. Rev. D* **95**, 082002 (2017).
- [19] N. Kurinsky, *The Low-Mass Limit, Dark Matter Detectors with eV-Scale Energy Resolution*, PhD thesis, Stanford University, 2018.
- [20] N. Mast, *Cryogenic Detector Development for SuperCDMS*, PhD thesis, University of Minnesota, 2020.
- [21] W. Rau *et al.*, *Journal of Physics: Conference Series* **1342**, 012128 (2020).
- [22] B. Ryden, *Introduction to cosmology* (Cambridge University Press, 2006).
- [23] S. Dodelson, *Modern Cosmology* (Academic Press, 2003).
- [24] C. Alcock *et al.*, *The Astrophysical Journal* **542**, 281 (2000).
- [25] K. Freese, B. D. Fields, and D. S. Graff, Death of stellar baryonic dark matter, in *MPA / ESO Workshop on the First Stars*, ESO Astrophysics Symposia European Southern Observatory, 1999, arXiv:astro-ph/0002058.
- [26] EROS-2, P. Tisserand *et al.*, *Astron. Astrophys.* **469**, 387 (2007), arXiv:astro-ph/0607207.
- [27] M. Milgrom, *The Astrophysical Journal* **270**, 371 (1983).
- [28] S. Boran, S. Desai, E. Kahya, and R. Woodard, *Phys. Rev. D* **97**, 041501 (2018), arXiv:1710.06168.
- [29] J. Moffat, *Phys. Lett. B* **763**, 427 (2016), arXiv:1603.05225.

- [30] D. Baumann, *Cosmology, Part III Mathematical Tripos* (, 2015).
- [31] D. G. Cerdeno, *Dark Matter 101, From Production to Detection* (, 2018).
- [32] ATLAS Collaboration, G. Aad *et al.*, *Physics Letters B* **716**, 1 (2012).
- [33] S. P. Martin, A supersymmetry primer, in *Advanced Series on Directions in High Energy Physics*, pp. 1–153, WORLD SCIENTIFIC, 2010.
- [34] D. E. Morrissey, Psi explorations: Beyond the standard model.
- [35] Fermi-LAT Collaboration, M. Ackermann *et al.*, *The Astrophysical Journal* **840**, 43 (2017).
- [36] S. Profumo, F. Queiroz, and C. Siqueira, *J. Phys. G* **48**, 015006 (2020), arXiv:1903.07638.
- [37] N. Trevisani, *Universe* **4** (2018).
- [38] ATLAS, E. Tolley, *PoS ICHEP2018*, 171 (2019).
- [39] F. Mayet and J. Billard, *Journal of Physics: Conference Series* **469**, 012013 (2013).
- [40] G. Bertone, D. Hooper, and J. Silk, *Physics Reports* **405**, 279 (2005).
- [41] C. A. J. O’Hare, *Phys. Rev. D* **102**, 063024 (2020).
- [42] R. Bernabei *et al.*, *Universe* **4**, 116 (2018).
- [43] J. Amaré *et al.*, *Phys. Rev. D* **103**, 102005 (2021).
- [44] M. Battaglieri *et al.*, US Cosmic Visions: New Ideas in Dark Matter 2017: Community Report, in *U.S. Cosmic Visions: New Ideas in Dark Matter*, 2017, arXiv:1707.04591.
- [45] K.-C. Yang, *JHEP* **11**, 048 (2019), arXiv:1905.09582.
- [46] K. Petraki and R. R. Volkas, *Int. J. Mod. Phys. A* **28**, 1330028 (2013), arXiv:1305.4939.
- [47] K. J. Bae, M. Park, and M. Zhang, *Phys. Rev. D* **101**, 115036 (2020).
- [48] SuperCDMS Collaboration, R. Agnese *et al.*, *Phys. Rev. D* **92**, 072003 (2015).

- [49] SuperCDMS Collaboration, R. Agnese *et al.*, Phys. Rev. Lett. **120**, 061802 (2018).
- [50] C. Jacoboni and L. Reggiani, Rev. Mod. Phys. **55**, 645 (1983).
- [51] K. Ramanathan and N. Kurinsky, Phys. Rev. D **102**, 063026 (2020).
- [52] W. Page, *Data Acquisition for SuperCDMS SNOLAB*, PhD thesis, University of British Columbia, 2015.
- [53] SuperCDMS Collaboration, R. Agnese *et al.*, Applied Physics Letters **103** (2013).
- [54] SuperCDMS Collaboration, R. Agnese *et al.*, Phys. Rev. Lett. **121**, 051301 (2018).
- [55] SuperCDMS, D. W. Amaral *et al.*, Phys. Rev. D **102**, 091101 (2020), arXiv:2005.14067.
- [56] CPD Collaboration, C. W. Fink *et al.*, Appl. Phys. Lett. **118**, 022601 (2021), arXiv:2009.14302.
- [57] SuperCDMS, I. Alkhatib *et al.*, (2020), arXiv:2007.14289.
- [58] Live Chart of Nuclides, <https://www-nds.iaea.org/relnsd/vcharthtml/VChartHTML.html>, Accessed July 28, 2021.
- [59] M. Bowles, *Minimizing Backgrounds for the SuperCDMS SNOLAB Dark-Matter Experiment*, PhD thesis, South Dakota School of Mines and Technology, 2019.
- [60] D. Barker, *SuperCDMS Background Models for Low-Mass Dark Matter Searches*, PhD thesis, University of Minnesota, 2018.
- [61] CoGeNT Collaboration, C. E. Aalseth *et al.*, Phys. Rev. Lett. **106**, 131301 (2011).
- [62] DAMIC, A. Aguilar-Arevalo *et al.*, JINST **10**, P08014 (2015), arXiv:1506.02562.
- [63] SNO, B. Aharmim *et al.*, Phys. Rev. D **80**, 012001 (2009), arXiv:0902.2776.
- [64] R. Essig, T. Volansky, and T.-T. Yu, Phys. Rev. D **96**, 043017 (2017).

- [65] D. S. Akerib *et al.*, Phys. Rev. D **102**, 092004 (2020).
- [66] DarkSide Collaboration, P. Agnes *et al.*, Phys. Rev. Lett. **121**, 111303 (2018).
- [67] CRESST Collaboration, A. H. Abdelhameed *et al.*, Phys. Rev. D **100**, 102002 (2019).
- [68] R. Strauss, J. Rothe, F. Petricca, and S. Schoenert, Journal of Physics: Conference Series **1342**, 012132 (2020).
- [69] EDELWEISS Collaboration, Q. Arnaud *et al.*, Phys. Rev. Lett. **125**, 141301 (2020).
- [70] EDELWEISS Collaboration, E. Armengaud *et al.*, Phys. Rev. D **99**, 082003 (2019).
- [71] SuperCDMS Internal, Comparison of PD2@SLAC with PD2@CUTE, <https://confluence.slac.stanford.edu/x/ngtYE>, Accessed June 14, 2021.
- [72] DAMIC Collaboration, A. Aguilar-Arevalo *et al.*, Phys. Rev. Lett. **123**, 181802 (2019).
- [73] SENSEI Collaboration, L. Barak *et al.*, Phys. Rev. Lett. **125**, 171802 (2020).
- [74] XENON Collaboration, E. Aprile *et al.*, Phys. Rev. Lett. **123**, 251801 (2019).
- [75] E. Aprile and T. Doke, Rev. Mod. Phys. **82**, 2053 (2010).
- [76] E. Aprile *et al.*, J.Phys. **G41** (2013).
- [77] P. Sorensen, (2017), arXiv:1702.04805.
- [78] CRESST Collaboration, J. Astrom *et al.*, Physics Letters A **356**, 262 (2005).
- [79] DAMIC Collaboration, A. Aguilar-Arevalo *et al.*, Phys. Rev. D **94**, 082006 (2016).
- [80] F. Chierchie *et al.*, (2020), arXiv:2012.10414.
- [81] SuperCDMS Internal, 0VeV-HVeV Preliminary Analysis V3, <https://confluence.slac.stanford.edu/x/U5HoE>, Accessed June 21, 2021.
- [82] I. Tamm, *Radiation Emitted by Uniformly Moving Electrons* (Springer Berlin Heidelberg, Berlin, Heidelberg, 1991), pp. 37–53.

- [83] P. Budini, Phys. Rev. **89**, 1147 (1953).
- [84] V. M. Grishin, Nucl. Instrum. Meth. A **482**, 629 (2002).
- [85] S. M. Neamtan, Phys. Rev. **92**, 1362 (1953).
- [86] V. P. Zrelov and J. Ruzicka, Nucl. Instrum. Meth. **151**, 395 (1978).
- [87] V. P. Zrelov and J. Ruzicka, Nucl. Instrum. Meth. **165**, 307 (1979).
- [88] V. P. Zrelov and J. Ruzicka, Nucl. Instrum. Meth. **160**, 327 (1979).
- [89] L. L. DeRaad, Jr., W.-y. Tsai, and T. Erber, Phys. Rev. D **18**, 2152 (1978).
- [90] V. L. Ginzburg and V. N. Tsytovich, Phys. Rept. **49**, 1 (1979).
- [91] V. P. Zrelov and J. Ruzicka, (1988).
- [92] S. Incerti, M. Douglass, S. Penfold, S. Guatelli, and E. Bezak, Physica Medica **32**, 1187 (2016).
- [93] E. Palik, *Handbook of Optical Constants of Solids* (Academic Press, 1991).